Master of Science Thesis

Multiscale Modelling of Discontinuities

Towards accurate computations of shock-turbulence interactions

Jan Willem Van Langenhove

July 1, 2014

Aerodynamics

Faculty of Aerospace Engineering

TU Delft

Delft University of Technology

Multiscale Modelling of Discontinuities

Towards accurate computations of shock-turbulence interactions

Master of Science Thesis

For obtaining the degree of Master of Science in Aerospace Engineering
at Delft University of Technology

Jan Willem Van Langenhove

July 1, 2014

Faculty of Aerospace Engineering · Delft University of Technology

Delft University of Technology

DELFT UNIVERSITY OF TECHNOLOGY
DEPARTMENT OF AERODYNAMICS

The undersigned hereby certify that they have read and recommend to the Faculty of Aerospace Engineering for acceptance the thesis entitled **"Multiscale Modelling of Discontinuities"** by **Jan Willem Van Langenhove** in fulfillment of the requirements for the degree of **Master of Science**.

Dated: July 1, 2014

Thesis supervisor:

Dr. S.J. Hulshoff

Committee members:

Dr. ir. M. Gerritsma

Dr. ing. M. Ruess

Dr. ir. R. Vos

Dr. ir. S. van Zuijlen

Preface

This thesis was the final leg on my journey towards an MSc. degree. It was a challenging thesis project, which makes successfully finishing it all the more satisfying. The challenges lie both in the topic, the fact that it is exploratory research, and on the practical side, working with a C++ code that is still in development. This also made it an incredibly interesting and worthwhile project.

There are many people that helped me along the way to whom I am greatly indebted.
I could have never gotten this far without the guidance of my thesis supervisor Dr. Steven Hulshoff. Under his tutelage I was given the opportunity to pursue my interests and the freedom to explore new research paths. There was an enjoyable atmosphere with room for informal talk, not just about work. I learned a great deal on this project and I have him to thank for it.

The mathematical background needed to fully understand the finite element method is not a part of the curriculum. A lot of functional analysis is required and studying that on your own is extremely difficult. But thanks to the seminars and discussions with my mathematics study group, under de guidance of Dr. Marc Gerritsma, I have been able to make a lot of progress in that area. I am very grateful for that.

All my years in Delft, I lived in *PH57 Heldenhuis*. What our house lacked in hygiene and tidiness was made up for in spirit. It was a memorable time during which I also learned some important life skills. When I came in I knew nothing, now I can cook meals and almost iron a shirt.

I also want to thank my friends for an unforgettable time. Our conversations and activities kept my mind open to a much broader range of topics then just my studies.

And last but certainly not least, I want to thank my parents for their unconditional support.

Summary

To overcome the computational challenges of shock-dominated flows, shock-capturing methods have been developed. Existing shock-capturing operators are designed to only become active in the vicinity of the shock and try to resolve the discontinuous solution on the computational grid by adding artificial dissipation. Furthermore, they are robust and generally applicable. The problem with these methods however is that their very working principle, using artificial dissipation, not only results in a smearing out the shock but also introduces an unphysical damping of turbulence. This is especially problematic for the simulation of shock-turbulence interactions.

In this thesis a different approach to shock-capturing is proposed, one that does not smear out the shock using dissipation but one that explicitly accounts for the unresolved scales which are present near a discontinuity. In this case shocks are seen as sharp discontinuities, the internal shock structure will not be investigated. It is also assumed that the element size is larger than the shock thickness such that a shock can always be captured in one element. A reasonable assumption as the shock thickness is usually of the order of the molecular mean free path.

We limit our attention to the Burgers' equation for which two cases are considered: a shock that is stationary with respect to the mesh and a shock that moves through the mesh. For the former case a multiscale analysis of the existing DCDD and $YZ\beta$ shock-capturing operators revealed the extent to which these shock-capturing methods approximate the exact integrated effect of the unresolved scales. In this thesis *Multiscale Shock-Capturing* (MSC), a shock-capturing parameter that reproduces the integrated effect of the unresolved scales was developed. For the stationary shock, MSC outperformed the existing shock-capturing methods used for reference.

For the moving shock it was found that taking into account the time dependency of the unresolved scales is essential. Here *Dynamic Multiscale Shock-Capturing* (DMSC) method is developed that achieves nodally exact solution for simple moving shocks. It is implemented in a semi-discrete formulation using an Euler implicit time march demonstrating its viability in practice. Applied to an idealized shock-turbulence interaction problem, DMSC performed very well and clearly better than the existing DCDD and $YZ\beta$ methods.

Table of Contents

Chapter 1

Introduction

Shock-turbulence interaction problems are among the most difficult type of problems in compressible flow. Turbulence by itself is a complex phenomenon that is not fully understood, shock waves interacting with turbulent compressible flow add another layer of complexity. For supersonic and hypersonic vehicles, particularly the development of air-breathing engines for those high-speed regimes, shock-turbulence interactions are very important. But also commercial airliners pushing operating speeds to a point where shock waves start to form face shock-turbulence interaction problems. Outside of aerospace, shock-turbulence interaction problems are also of interest to astrophysics for simulations of explosions of supernovae and to research on inertial confinement fusion (fusion energy).

This thesis deals only with numerical methods used for computing shock-turbulence interactions. Interest in such methods rose around World War II when compressibility effects had become increasingly important for the computation of blast waves and the design of aircraft and rockets. To be able to solve problems where shock waves played a role, shock-fitting methods were initially developed. These were largely based on the method of characteristics. With growing computer power and more sophisticated shock-fitting methods, ever more complex problems could be analysed. An account of the development of these early methods can be found in Salas (2011). A downside of shock-fitting methods, however, is the difficulty of handling complex shock structures in two or three dimensions. This is the reason why nowadays shock-capturing methods are more popular.

1.1 Shock-capturing methods

Shock-capturing methods generally use artificial viscosity as a remedy against the oscillations that tend to occur when trying to numerically obtain a solution with sharp gradients (Gibbs phenomenon). They are less cumbersome than shock-fitting methods and applicable to general problems, including problems with complex shock structures. The downside of this approach

is that this artificial viscosity tends to smear out the shock over a broad region and damps physically correct oscillations resulting in an unphysical damping of the turbulence (Larsson, 2009). This is especially problematic for shock-turbulence interaction problems.

The development of shock-capturing methods for finite difference and finite volume discretizations has received significant attention since the 1970's, with important milestones including the development of total variation diminishing (TVD) and ENO/WENO schemes ((W)ENO stands for (weighted) essentially non-oscillatory) along with less costly more recent contributions. For an overview see Yee et al. (2001).

Similar concepts were used in the development of finite element methods. One of the earliest stabilized finite element formulations was streamline upwind/Petrov-Galerkin (SUPG), it was developed as an upwinding technique for finite elements (Brooks and Hughes, 1982). It was later rewritten for entropy variables and a shock-capturing operator was added. This shock capturing operator was just an additional operator working in tandem with SUPG (Hughes and Mallet, 1986), it would only be active in the crosswind direction to iron out the oscillations that the stabilization method, only working in the streamline direction, had failed to address. That formulation was later improved by Le Beau and Tezduyar (1991) with a new shock-capturing term, which later became known as δ_{91}. Detailed analysis and proof of convergence of these shock-capturing streamline diffusion methods was done by Johnson and Szepessy (Johnson et al., 1990; Szepessy, 1989, 1991).

As a reference two recent shock-capturing methods are implemented and used throughout this thesis. The formulation of their shock-capturing parameters is both more compact and more efficient than δ_{91}. The first of those methods is called $YZ\beta$ discontinuity capturing. It was introduced by Tezduyar (2004) and very good results were reported in Tezduyar and Senga (2006, 2007); Tezduyar et al. (2006). The second method used as reference is the *Discontinuity Capturing Directional Dissipation* (DCDD) method developed by Rispoli et al. (2007).

Exploiting the possibilities of adaptivity for finite element methods, Nazarov and Hoffman came up with a combination of adaptivity and artificial viscosity for their shock-capturing method (Nazarov and Hoffman, 2010). Most other shock-capturing methods are consistent, in that their error will go to zero as the element size goes to zero. So using an adaptive method, where the element size is reduced in the regions where the shock-capturing operator is active, will improve results for all of these methods. It will not however solve the problem of the flawed unresolved scale models being used for that artificial viscosity. For compressible flow problems they report that turbulence and shocks are under-resolved (Nazarov and Hoffman, 2013).

Another possibility is to use *spectrally vanishing viscosity* (Tadmor, 1989). With this technique the dissipation term only becomes active in the part of the spectral approximation where the frequency is high. Then there is also the *entropy viscosity method* developed by Guermond, Pasquetti, Richard and coworkers (Guermond and Pasquetti, 2011; Guermond et al., 2011). Which bases the artificial viscosity on the magnitude of entropy production.

A recent approach to shock-capturing using the variational multiscale method, is to enforce a monotonic solution by constraining the basis (Evans et al., 2009). While this does give good

results in the test cases of a steady convection-diffusion equation, it also implies an unresolved scale model and it is unclear how it will influence models for unresolved turbulence. As such it will be difficult to control the outcome of shock-turbulence interactions because the subgrid scale model is in two places, one is given by the turbulence model and the other is implied by the constraining of the basis.

These are all techniques that can prevent oscillations from occurring, but without the capacity to discern physically correct fluctuations from numerical errors. It is therefore inevitable that the methods mentioned above will, to some extent, distort turbulent fluctuations.

1.2 Multiscale concept

Any phenomenon dealing with turbulence is characterised by an intricate interplay of eddies and whirls of different length scales. Things that happen at the smallest length scales influence the largest length scales and vice versa, and computing what happens at all these length scales is computationally very intensive (it is known as a Direct Numerical Simulation (DNS)). For real-world problems a DNS usually takes too much time and computational resources. As a result, only the dynamics of the larger scales are normally computed while the influence of the unresolved smaller scales is modelled. This is known as a large eddy simulation (LES).

The conceptual development of unresolved-scale models (USM) requires a precise definition of the resolved scales $\bar{u}$ and the unresolved scales u'. Classically this is done using explicit filtering, although this is not often used in practice. In this thesis the variational multiscale concept is used for scale separation, as this clarifies scale separation in realistic computations.

This work will consider two-scale variational multiscale methods for which different scales are represented by projection into subspaces: the variational statement of the problem at hand is defined in a suitable mathematical space and different scales are given by projection into a finite dimensional subspace for the large scales and into an infinite dimensional subspace for the small scales.

1.3 Scope of this thesis

To effectively treat shock-turbulence interactions it seems desirable to consider the design of USM's in a framework which allows the unresolved effects of shocks and turbulence to be considered directly. We need an approach to develop unresolved scale models where the concepts of unresolved shocks and turbulence can be united. The variational multiscale method provides a suitable framework for this, as it deals explicitly with the (approximation of) unresolved scales. As a first step towards a unified shock-turbulence unresolved scale model, we will investigate if existing shock-capturing techniques have a multiscale interpretation, and then develop exact unresolved scale models for shocks as a guide for developing future shock-turbulence variational multiscale unresolved scale models. As the development of exact

USM's can be laborious, we restrict our attention to a model equation for shock dynamics, the (viscous) Burgers' equation.

The content of this thesis is as follows: in Chapter 2 the variational multiscale method is presented. The link with stabilization methods SUPG and variable subgrid scale stabilization (V-SGS) is demonstrated for the convection-diffusion equation. The next chapter, Chapter 3, treats the *Discontinuity-Capturing Directional Dissipation* and $YZ\beta$ shock-capturing methods. These two shock-capturing methods will be used as a reference later on. Chapter 4 deals with a stationary Burgers' shock, a multiscale analysis is made of DCDD and $YZ\beta$ and a new shock-capturing method called *Multiscale Shock-Capturing* is developed. The more difficult problem of a moving Burgers' shock is tackled in Chapter 5. A new method called *Dynamic Multiscale Shock-Capturing* is developed here by taking into account the dynamic influence of the unresolved scales. Then, in Chapter 6 the *Dynamic Multiscale Shock-Capturing* method is tested on a model shock-turbulence interaction problem and the results are compared to the DCDD and $YZ\beta$ methods. Finally the conclusions and recommendations are presented in the last chapter.

Chapter 2

The variational multiscale method

This chapter will introduce the approach and notation of the variational multiscale method which is used to develop shock-capturing methods later in the report. Standard approaches to the representation of u' will also be introduced. These will be used in connection with the shock-capturing operators.

In the introduction it was explained that stabilization methods used in compressible flow computations are not enough to solve the problem of oscillations around discontinuities. In the chapters after this one both streamline upwind/Petrov-Galerkin (SUPG) (Brooks and Hughes, 1982) and variable subgrid scale (V-SGS) (Corsini et al., 2005) stabilization will be used in combination with different shock-capturing operators. So not only the stabilization will be tested but also the interaction with shock-capturing operators. SUPG was designed as a finite element implementation of a stabilization technique first developed for finite volume and finite difference methods: upwinding. It was discovered later that SUPG can be interpreted as an approximation to the small-scale terms in a variational multiscale decomposition. V-SGS was developed later, it is similar to SUPG but used the variational multiscale framework from the onset.

In this work the focus will be on two-scale variational multiscale methods, where the large-scale equation will be resolved and the small-scale equation will be modeled. This type of method is a relatively recent development. In Hughes et al. (1998), an L^2 projector was used to decompose the solution as a sum: $u = \bar{u} + u'$ (with $\bar{u}$ being the large scales and u' the small scales). Other projectors are also possible, as will be discussed in this chapter. For an explanation of the function spaces and notation used, the reader is referred to Appendix B.

2.1 The abstract problem

If $\Omega \subset \mathbb{R}^d$ is an open bounded domain with smooth boundary Γ, then a standard boundary-value problem with Dirichlet boundary conditions would read: find $u : \Omega \to \mathbb{R}$ such that

$$Lu = f \quad \text{in } \Omega \tag{2.1}$$
$$u = g \quad \text{on } \Gamma. \tag{2.2}$$

In the above equation L can be up to a second-order non-symmetric differential operator. To keep this discussion compact, only Dirichlet boundary conditions are used here but other boundary conditions can be used as well. Now let $\mathcal{V} \subset H^1(\Omega)$ be the weighting function space and $\mathcal{S} \subset H^1(\Omega)$ the trial solution space. So the following holds:

$$u = g \quad \text{on } \Gamma \ \forall u \in \mathcal{S} \tag{2.3}$$
$$w = 0 \quad \text{on } \Gamma \ \forall w \in \mathcal{V}. \tag{2.4}$$

The equivalent variational problem statement is: Find $u \in \mathcal{S}$ such that $\forall w \in \mathcal{V}$:

$$B(w, u) = F(w) \tag{2.5}$$

with $B(\ .\ ,\ .\ )$ being the bilinear form

$$B(w, u) = (w, Lu) \tag{2.6}$$

and $F(.)$ a linear form

$$F(w) = (w, f). \tag{2.7}$$

Throughout this document the inner product notation $(\ .\ ,\ .\ )$ will be used (see Appendix B and references therein for more details). As explained above the solution is split up, decomposed as a sum of the large-scale and small-scale solution:

$$u = \bar{u} + u' \tag{2.8}$$
$$w = \bar{w} + w' \tag{2.9}$$

note that now the trial function space and weighting function space are also decomposed as $\mathcal{S} = \bar{\mathcal{S}} \oplus \mathcal{S}'$ and $\mathcal{V} = \bar{\mathcal{V}} \oplus \mathcal{V}'$ respectively. The boundary conditions now become:

$$\bar{u} = g \quad \text{on } \Gamma \ \forall \bar{u} \in \bar{\mathcal{S}} \tag{2.10}$$
$$u' = 0 \quad \text{on } \Gamma \ \forall u' \in \mathcal{S}' \tag{2.11}$$
$$\bar{w} = 0 \quad \text{on } \Gamma \ \forall \bar{w} \in \bar{\mathcal{V}} \tag{2.12}$$
$$w' = 0 \quad \text{on } \Gamma \ \forall w' \in \mathcal{V}' \tag{2.13}$$

The actual splitting of $\mathcal{V}$ and $\mathcal{S}$ is done by a linear projector $\mathcal{P}$, this projector is called the variational projector. The most used ones are the L^2-projector

$$\bar{\mathcal{P}}_{L^2} : u \in \mathcal{V} \to \bar{u} \in \bar{\mathcal{V}} \ \text{ s.t. } (\bar{w}, \bar{u}) = (\bar{w}, u) \ \forall \bar{w} \in \bar{\mathcal{V}} \tag{2.14}$$

and the H^1-projector, or the H^1 semi-norm projector:

$$\bar{\mathcal{P}}_{H^1} : u \in \mathcal{V} \to \bar{u} \in \bar{\mathcal{V}} \text{ s.t. } (\nabla\bar{w}, \nabla\bar{u}) = (\nabla\bar{w}, \nabla u)\ \forall\bar{w} \in \bar{\mathcal{V}}. \tag{2.15}$$

The projector onto $\mathcal{V}'$ is called $\mathcal{P}'$, it is defined as $\mathcal{P}' = Ker(\bar{\mathcal{P}})$.

$$u' = u - \bar{u} = (\mathcal{I} - \bar{\mathcal{P}})u = \mathcal{P}'u \tag{2.16}$$

The initial variational problem can now be rewritten as

$$B(\bar{w} + w', \bar{u} + u') = (\bar{w} + w', f)\ \forall\bar{w} \in \bar{\mathcal{V}},\ \forall w' \in \mathcal{V}' \tag{2.17}$$

From (2.17) the following identities can be established:

$$B(\bar{w}, u') = (L^*\bar{w}, u')\ \forall\bar{w} \in \bar{\mathcal{V}}, u' \in \mathcal{S}', \tag{2.18}$$
$$B(w', \bar{u}) = (w', L\bar{u})\ \forall w' \in \mathcal{V}', \bar{u} \in \bar{\mathcal{S}}, \tag{2.19}$$
$$B(w', u') = (w', Lu')\ \forall w' \in \mathcal{V}', u' \in \mathcal{S}', \tag{2.20}$$

where L^* is the adjoint operator of L, i.e. $(w, Lu) = (L^*w, u)$. (2.17) can now be split up into two problems (this is allowed because $\bar{w}$ and w' are linearly independent), the first problem is:

$$B(w', \bar{u}) + B(w', u') = (w', f)\ \forall w' \in \mathcal{V}' \tag{2.21}$$

or equivalently

$$(w', L\bar{u}) + (w', Lu') = (w', f) \tag{2.22}$$

and the second one:

$$B(\bar{w}, \bar{u}) + B(\bar{w}, u') = (\bar{w}, f)\ \forall\bar{w} \in \bar{\mathcal{V}}, \tag{2.23}$$

or equivalently

$$(\bar{w}, L\bar{u}) + (L^*\bar{w}, u') = (\bar{w}, f). \tag{2.24}$$

The large-scale equation (2.24) contains a small-scale term that represents the influence of the unresolved scales on the resolved scales. Stabilization methods following a multiscale philosophy try to approximate this small-scale term. The small-scale solution can be expressed in terms of its Green's function:

$$u'(y) = \int_\Omega g'(x, y)(f - L\bar{u})(x)dx \tag{2.25}$$

and because this small-scale Green's function is generally not known it is usually approximated by a parameter τ such that:

$$u' \approx \tau(f - L\bar{u}). \tag{2.26}$$

Note that this is a function of the large-scale residual $\bar{R}$:

$$\bar{R} = L\bar{u} - f. \tag{2.27}$$

For further details about this Green's function, the reader is referred to Appendix A.1.

2.2 The link between stabilized methods and the variational multiscale method

Stabilized Galerkin methods can generally be written in the form

$$B(w,u) + B_{stab}(w,u) = F(w) + F_{stab}(w) \quad \forall w \in V \tag{2.28}$$

Using the variational multiscale method explained in the previous section, (2.28) can be split up into a large-scale and a small-scale equation. For non-linear problems, this assumption is often made: $B_2(w', u', u') \approx 0$. Using (2.26), the large-scale equation of (2.28) can be written as

$$(\bar{w}, L\bar{u}) + (L^*\bar{w}, \tau(L\bar{u} - f))_{\cup\Omega_e} = (w, f) \quad \forall \bar{w} \in \mathcal{V} \tag{2.29}$$

So now the small-scale term in that large-scale equation is expressed as a function of the adjoint operator L^*, the small scale Green's function (in this case approximated by τ) and the large scale residual $\bar{R} = L\bar{u} - f$. In the subsequent sections the relation of this small-scale Green's function with τ will be analysed for the convection-diffusion equation. There are different ways to approximate g' which will result in a different τ, and different stabilization methods. Here SUPG and V-SGS stabilization will be considered but note that other stabilization methods may differ in the u' terms that are included (e.g. GLS).

2.2.1 Convection-diffusion equation

The 1D scalar convection-diffusion equation is of the form:

$$a\frac{du}{dx} - k\frac{d^2u}{dx^2} = f(x) \tag{2.30}$$

where a is a constant that determines the convection speed and k is diffusivity constant. Let u_x be the derivative of u with respect to x, u_{xx} the second derivative, then (2.30) can be formulated as

$$au_x - ku_{xx} = f(x). \tag{2.31}$$

The solution of this equation on the domain $\Omega = [0,1] \in \mathbb{R}$ with boundary Γ and $f = 0$, $u(0) = u(1) = 0$, $a = 1$, $k = 0.01$ will be the model problem considered for the next sections. Note that the convection-diffusion differential operator can be written as

$$L = a\frac{d}{dx} - k\frac{d^2}{dx^2}, \tag{2.32}$$

and its adjoint (for the case of zero Dirichlet boundary conditions) as:

$$L^* = -a\frac{d}{dx} - k\frac{d^2}{dx^2}. \tag{2.33}$$

So the model problem can also be written as

$$Lu = 0 \tag{2.34}$$
$$u(0) = 0 \tag{2.35}$$
$$u(1) = 0. \tag{2.36}$$

For the convection-diffusion equation, the Green's function of interest can be computed

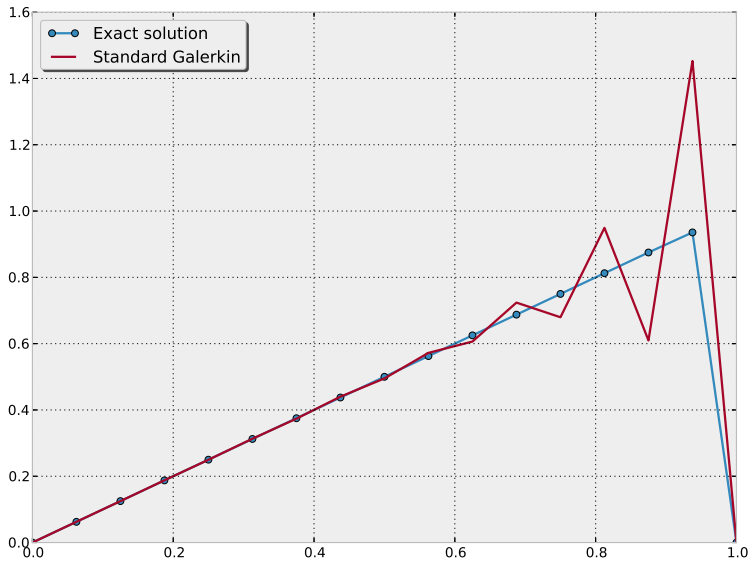

Figure 2.1: Solution of the 1D advection-diffusion problem with $a = 1$ and $k = 0.01$ using the standard Galerkin method and 16 elements.

(see Appendix A.2) and the stabilization parameter τ_{SUPG} and τ_{V-SGS} are approximations thereof. The exact solution of the model problem along with a finite element approximation is given in Fig. 2.1.

2.2.2 SUPG stabilization

The SUPG stabilization parameter τ_{SUPG} is found by taking the average τ_{exact} (see A.44) over the element domain:

$$\tau_{SUPG} = \frac{1}{h}\int_{\Omega_e} \tau_{exact}(\zeta) d\Omega_e, \tag{2.37}$$
$$= \frac{-2k + ah\coth\left(\frac{ah}{2k}\right)}{2a^2}, \tag{2.38}$$
$$= \frac{h}{2|a|}\left(\coth\left(Pe\right) - \frac{1}{Pe}\right) \tag{2.39}$$

where h is the element size, Pe is the element Peclet number $Pe = \frac{|a|h}{2k}$. This τ_{exact} is exactly the Green's function g_e as derived in Appendix A.2.1. For this case with linear test functions, SUPG is a special case of the variational multiscale method, where instead of the adjoint L^*, only the advective part of the original differential operator is used (because $\partial^2 w/\partial x^2 = 0$) and τ is used in the approximation of g'.

$$B_{SUPG}(w, u) = (L_{adv} w, \tau L u) \tag{2.40}$$

The SUPG formulation worked out for this example is

$$(w, au_x) + (w_x, ku_x) + (aw_x, \tau_{SUPG}(au_x - ku_{xx} - f)) = (w, f) \tag{2.41}$$

In this example the solution using this stabilization with linear elements is nodally exact, as can be seen in Fig. 2.2. Which is clearly a lot better than the solution without stabilization shown in Fig. 2.1.

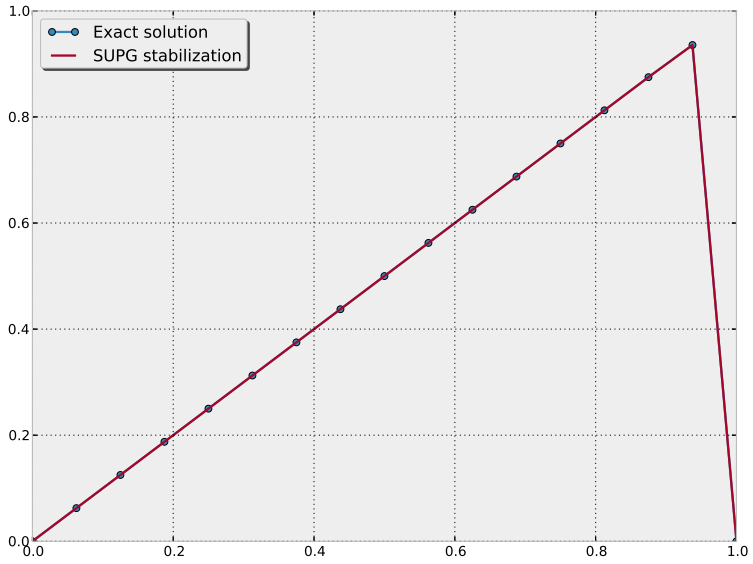

Figure 2.2: Solution of the 1D advection-diffusion problem with $a = 1$ and $k = 0.01$ using SUPG stabilization and 16 elements.

2.2.3 Variable subgrid scale stabilization (V-SGS)

The V-SGS method for compressible flows by Rispoli and Rafael Saavedra (2006) was developed with the variational multiscale framework of Hughes, using the insight that stabilization can in some cases be seen as a manifestation of the subgrid scales.

In the original work of Rispoli and Rafael Saavedra (2006) the stabilization parameter is derived for a parent element with domain $[-1, 1]$, here however the parent element is taken as $[0, 1]$ so the τ_{V-SGS} computed here will be slightly different from their paper.

In this method, the stabilization parameter τ_{V-SGS} is not the mean value over the element, as with SUPG, instead it is exactly (A.44). So τ_{V-SGS} will vary over the domain, it can be decomposed in a mean and a fluctuating term:

$$\tau_{V-SGS} = \tau_{SUPG}(1 + f_{fluct}(\zeta, Pe)), \tag{2.42}$$

where the fluctuating part is

$$f_{fluct}(\zeta, Pe) = -1 - 2ah^2 \frac{\zeta - 1 + e^{2\frac{a}{|a|}Pe\zeta} - e^{2\frac{a}{|a|}Pe}\zeta}{e^{2\frac{a}{|a|}Pe} - 1} \left(\coth(Pe) - \frac{1}{Pe}\right)^{-1} \tag{2.43}$$

Fig. 2.3 shows the result of V-SGS stabilization on the example problem. The result is good, but not quite as good as SUPG which uses a simpler approximation for τ_{exact}. The reason for this is explained below.

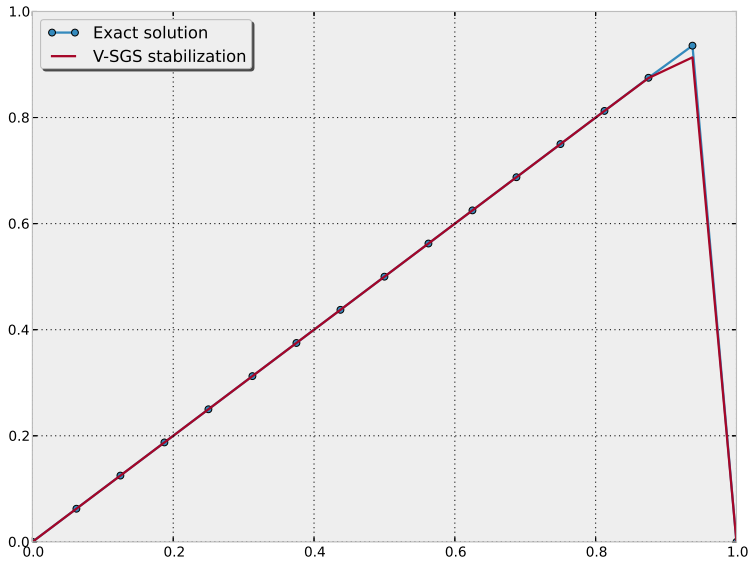

Figure 2.3: Solution of the 1D advection-diffusion problem with $a = 1$ and $k = 0.01$ using V-SGS stabilization and 16 elements.

2.2.4 Comparison of SUPG and V-SGS

The approximation of the small-scale element Green's functions g'_e of SUPG (τ_{SUPG}) and that of V-SGS τ_{V-SGS} are plotted (on a single 1D element) in Fig. 2.4 and 2.5. From those figures it is clear that τ_{SUPG} is just a constant, while τ_{V-SGS} varies over the element domain. V-SGS was developed for quadratic elements, but in the computations here only linear elements were used. We will stick to linear elements throughout this thesis to avoid making things needlessly complicated later on. If V-SGS performs worse here than reported in literature the restriction to linear elements is the cause.

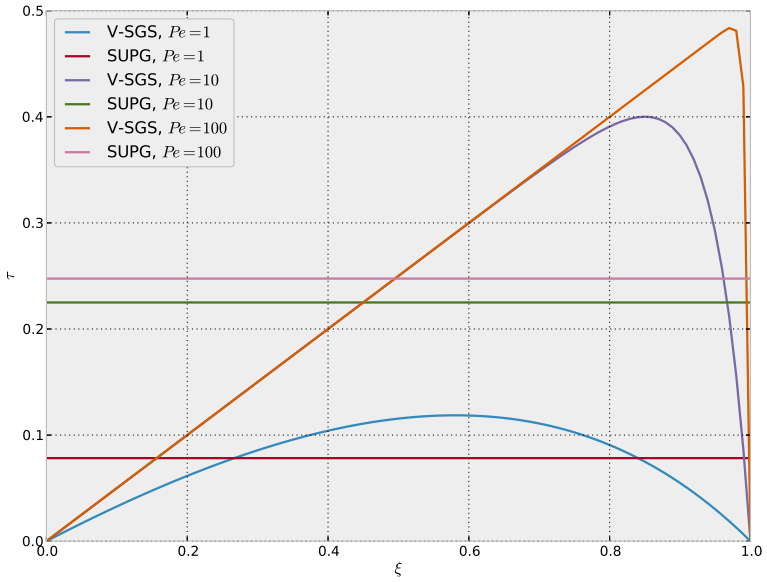

Figure 2.4: Comparison of τ_{SUPG} and τ_{V-SGS} when $a > 0$.

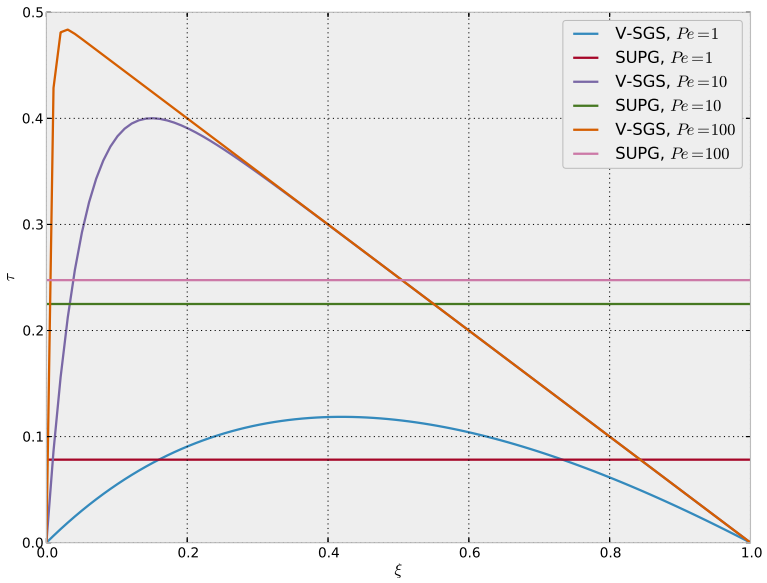

Figure 2.5: Comparison of τ_{SUPG} and τ_{V-SGS} when $a < 0$.

2.3 Summary of results

In this chapter the variational multiscale method was explained for a general abstract problem. Then the SUPG and V-SGS stabilization were derived for an example problem where the convection-diffusion equation was considered.

The reader should remember from this chapter how stabilization methods in the variational multiscale framework try to approximate the influence of the unresolved scales on the large-scale equation. The variational multiscale method is not just a way to split up a partial differential equation (PDE) into multiple equations each describing the solution at different scales, it also provides a framework to analyze and develop stabilization and shock-capturing methods. In the next chapters, this idea will be used to try and find a multiscale interpretation of existing shock-capturing operators as well to develop new shock-capturing methods.

Chapter 3

Shock-capturing

In this chapter two existing shock-capturing methods are presented. They will be demonstrated on two model problems to give the reader some insight into their performance. In subsequent chapters, the shock-capturing methods presented here will be used to generate reference solutions. The chapter will focus on their application to the Burgers' equation, which is used for later comparisons.

3.1 Burgers' equation

Continuing with the same notation as in chapter 2, the variational form of Burgers' equation will now be presented. One important fact here is that it is a nonlinear equation, so when looking at the VMS formulation of this equation one must make sure to correctly take into account all the terms resulting from this nonlinearity.

For nonlinear problems, the problem $B(w,u) = F(w)$ (see Eq. 2.5) is split up into $B_1(w,u) + B_2(w,u,u) = F(w)$ where B_1 contains all the linear terms and B_2 all the nonlinear terms. B_1 is a regular bilinear form, while B_2 is a trilinear form.

The 1D Burgers' equation is:

$$\frac{\partial u}{\partial t} + u\frac{\partial u}{\partial x} - \nu\frac{\partial^2 u}{\partial x^2} = f \tag{3.1}$$

$$\tag{3.2}$$

or in short notation:

$$u_t + uu_x - \nu u_{xx} = f. \tag{3.3}$$

The corresponding Burgers' operator L, linearized around u (see the nonlinear term uu_x as

$a(u)u_x)$ is

$$L = \frac{\partial \cdot}{\partial t} + a(u)\frac{\partial \cdot}{\partial x} - \frac{\partial}{\partial x}\left(\nu \frac{\partial \cdot}{\partial x}\right) \tag{3.4}$$

$$L^* = -\frac{\partial \cdot}{\partial t} - a(u)\frac{\partial \cdot}{\partial x} - \frac{\partial}{\partial x}\left(\nu \frac{\partial \cdot}{\partial x}\right) \tag{3.5}$$

$$\tag{3.6}$$

such that:

$$Lu = \frac{\partial u}{\partial t} + u\frac{\partial u}{\partial x} - \nu \frac{\partial^2 u}{\partial x^2} \tag{3.7}$$

and then the variational form of the problem is:

$$(w, Lu) = (w, f). \tag{3.8}$$

When Eq. 3.8 is expanded, the terms can be grouped into linear terms and nonlinear terms (the linear terms will be collected into B_1 and the nonlinear term into B_2):

$$\underbrace{\underbrace{(w, u_{,t}) + (w_{,x}, \nu u_{,x})}_{B_1(w,u)} + \underbrace{(w, uu_{,x})}_{B_2(w,u,u)}}_{B(w,u)} = \underbrace{(w, f)}_{F(w)} \tag{3.9}$$

Variational Multiscale Formulation

The variational formulation Eq. 3.8 can be decoupled into two equations:

$$B(\bar{w}, \bar{u} + u') = L(\bar{w}) \tag{3.10}$$

$$B(w', \bar{u} + u') = L(w') \tag{3.11}$$

Worked out a bit further:

$$B_1(\bar{w}, \bar{u}) + B_1(\bar{w}, u') + B_2(\bar{w}, \bar{u}, \bar{u}) + B_2(\bar{w}, \bar{u}, u') + B_2(\bar{w}, u', \bar{u}) + B_2(\bar{w}, u', u') = L(\bar{w}) \tag{3.12}$$

$$B_1(w', \bar{u}) + B_1(w', u') + B_2(w', \bar{u}, \bar{u}) + B_2(w', \bar{u}, u') + B_2(w', u', \bar{u}) + B_2(w', u', u') = L(w') \tag{3.13}$$

And if the large-scale equation is worked out further the result is:

$$(\bar{w}, \bar{u}_t) + (\bar{w}_x, \nu \bar{u}_x) + (\bar{w}, u'_t) + (\bar{w}_x, \nu u'_x) + (\bar{w}, \bar{u}\bar{u}_x) + (\bar{w}, \bar{u}u'_x) + (\bar{w}, u'\bar{u}_x) + (\bar{w}, u'u'_x) = (\bar{w}, f) \tag{3.14}$$

More detail on the discretization of Burgers' equation, including time-march, is provided in Appendix C.

3.1.1 Case 1: Initial discontinuity

In this test case the initial solution takes the form

$$u(x, t = 0) \begin{cases} u_L & \forall x \leq x_s \\ u_R & \forall x > x_s \end{cases}$$

here $x_s = 0.5$, it is the initial shock position. And the viscosity is $\nu = 0.001$.

3.1.2 Case 2: Steepening wave

In this test case the initial solution is a sine wave:

$$u(x, t = 0) = \sin(2\pi x),$$

and as time goes by, this wave will steepen into a sawtooth-like shape, limited by the value of ν, which was chosen as 0.001.

3.2 Existing Shock-capturing methods

Summarizing the works of Wilkins (1980), Noh (1987), Christensen (1990) and Caramana et al. (1998), Scovazzi gives a good overview of the design requirements for classical shock-capturing operators in his PhD thesis (Scovazzi, 2004): *"... design requirements can be summarized as follows:*

1. *Dissipativity: the DC operator must be a dissipative operator (i.e., it must dissipate energy), possibly - but not necessarily - defined through a viscosity operator.*
2. *Galilean Invariance: the DC operator must be invariant under Galilean transformations of coordinates.*
3. *Rotation invariance: it is advisable, especially in problems involving convergent flows, for the DC operator to be invariant under rotations.*
4. *The model should not introduce artificial dissipation along a surface of constant phase (a surface along which the magnitude of the velocity is constant, with a possible change in direction). An example of a surface of constant phase is a shock front, either planar or curved, as in the case of cylindrical or spherical symmetry.*
5. *The DC operator must vanish for expansions, since the solution is smooth enough to be accurately computed by the underlying numerical discretization. It is also advisable for the DC operator to vanish in a zone of uniform compression, for which a second-order code can represent the exact solution. Finally, it is of interest that the transition from zones in which the DC operator is inactive, to zones in which it is different from zero, be continuous."*

Much in the same way as with stabilization, for shock-capturing a new term is added. So using both stabilization and shock-capturing terms, the formulation for a general problem would look like this:

$$B(w,u) + \underbrace{(L_{stab}w, \tau(Lu-f))}_{\text{stabilization}} + \underbrace{(\nabla w, k_{shock}\nabla u)}_{\text{shock-capturing}} = (w,f). \tag{3.15}$$

3.2.1 Discontinuity-Capturing Directional Dissipation

A recent shock-capturing operator or discontinuity-capturing operator is the *Discontinuity-Capturing Directional Dissipation* (DCDD) method proposed by Rispoli et al. (2007). The DCDD artificial viscosity is defined as:

$$k_{shock} = \nu_{shock} rr - \nu_{shock}(r \cdot s)^2 ss \tag{3.16}$$

with ν_{shock}:

$$\nu_{shock} = \frac{1}{2}\left(\frac{||u||}{u_{ref}}\right)^2 (h_{DCDD})^2 ||u_x|| \tag{3.17}$$

and $h_{DCDD} = 2\left(\sum_{a=1}^{n_{funs}} |r\nabla N_a|\right)^{-1}$, $s = \frac{u}{||u||}$ and $r = \frac{\nabla||u||}{||\nabla||u||\ ||}$. The full term becomes:

$$\sum_{e=1}^{n_{el}} \int_{\Omega^e} w_x k_{shock} u_x d\Omega$$

or when expanded fully:

$$\sum_{e=1}^{n_{el}} \int_{\Omega^e} w_x (k_{shock} rr - k_{shock}(r \cdot s)^2 ss) u_x d\Omega$$

The performance of DCDD for the two test problems both with and without stabilization is demonstrated in Fig. 3.1 and 3.2.

3.2.2 $YZ\beta$ shock capturing

$YZ\beta$ shock capturing, uses a parameter k_{shock} computed as follows:

$$k_{shock} = \nu_{shock}\mathbf{D} \tag{3.18}$$

where ν_{shock} is the magnitude and $\mathbf{D}$ is a matrix that determines the direction in which this operator works. An isotropic operator is produced when $\mathbf{D} = \mathbf{I}$ and ν_{shock} computed by:

$$\nu_{shock} = \left|\left|Y^{-1}Z\right|\right| \left(\sum_{i=0}^{n_{dim}} \left|\left|Y^{-1}\frac{\partial \mathbf{u}}{\partial x_i}\right|\right|^2\right)^{\beta/2-1} \left(\frac{h_{shock}}{2}\right)^{\beta} \tag{3.19}$$

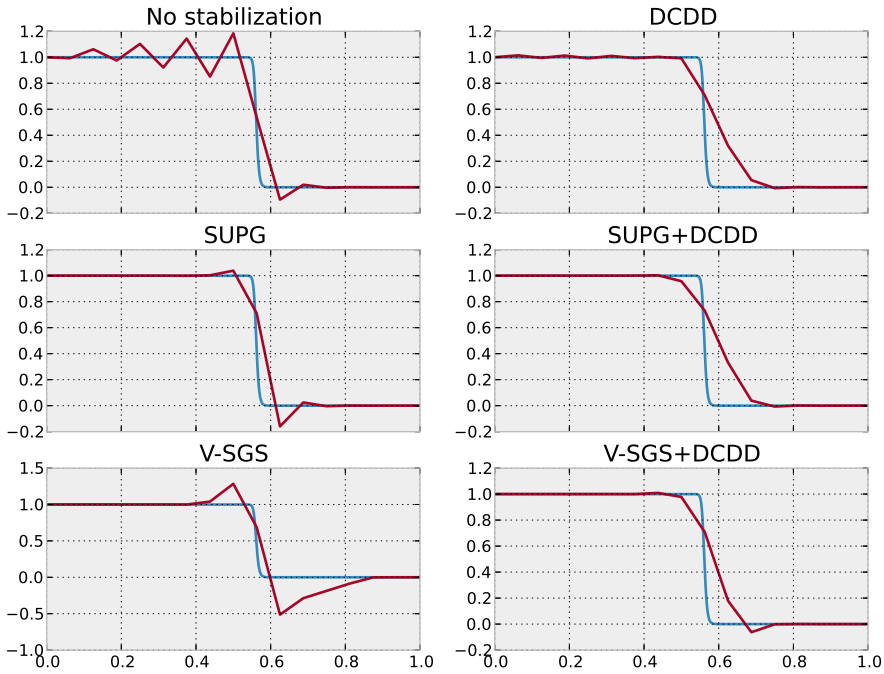

Figure 3.1: DCDD with and without stabilization on initial discontinuity test case at $t = 0.2$, using 16 elements plotted in red; the DNS is plotted in blue.

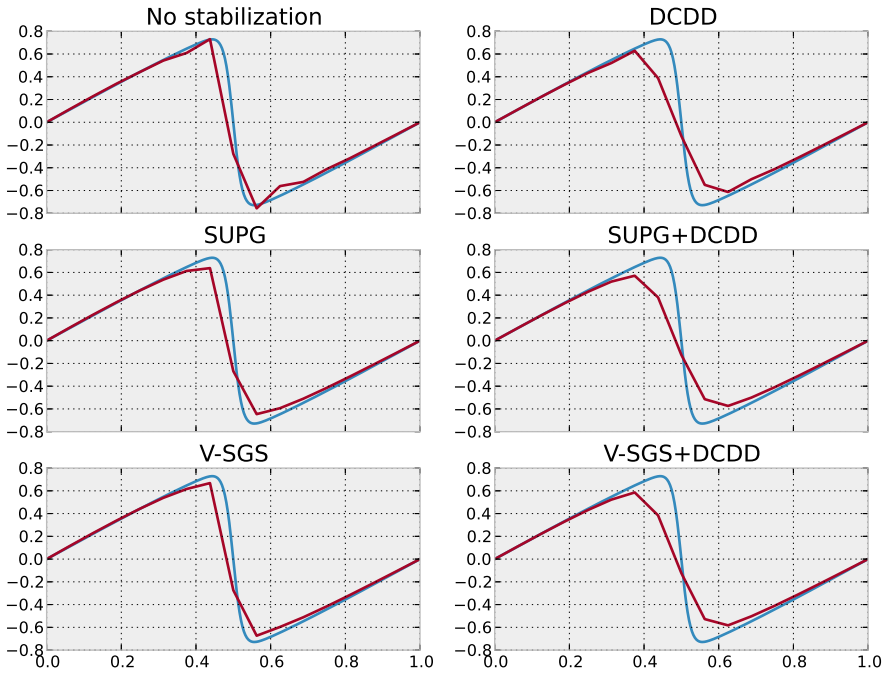

Figure 3.2: DCDD with and without stabilization on the steepening wave test case at $t = 0.4$, using 16 elements plotted in red; the DNS is plotted in blue.

with

$$Y = \mathbf{u}_{ref}$$
$$Z = \mathbf{u}\nabla\mathbf{u}$$
$$h_{shock} = 2\left(\sum_{a=1}^{n_{fun}} |\mathbf{j}\cdot\nabla N_a|\right)^{-1} \quad \text{and unit vector } \mathbf{j} = \frac{\nabla\mathbf{u}}{||\nabla\mathbf{u}||}.$$

The parameter β is set to 1 for shocks that are somewhat smooth and to 2 for sharp discontinuities (Tezduyar and Senga, 2006), and n_{funs} is the number of basis functions. The operator Z can also be taken as $L\mathbf{u} - f$, in that case Z is not an advective operator but rather a residual-based one. In the latter case, the accuracy of the result depends less on the chosen value for β and a sharper shock representation is possible (Bazilevs et al., 2007). For the 1D Burgers' equation this can be reduced to:

$$\nu_{shock} = \left|\frac{1}{u_{ref}} u \frac{\partial u}{\partial x}\right| \left(\frac{1}{u_{ref}}\frac{\partial u}{\partial x}\right)^{2(\beta/2-1)} (h_{shock})^{\beta} \tag{3.20}$$

$$\text{with} \quad h_{shock} = \left(\sum_{a=0}^{n_{fun}} \left|\frac{\partial u/\partial x}{||\partial u/\partial x||}\frac{\partial N_a}{\partial x}\right|\right)^{-1}. \tag{3.21}$$

In the expressions above, u_{ref} is some chosen reference solution. In this case u_{ref} will be taken as $u^{n+1,i}$, the local solution at the previous iteration. When inserted into the variational form, 1D Burgers' equation with YZβ discontinuity capturing becomes:

$$(w, u_t + uu_x - \nu u_{xx}) + \left(w_x, \left|\frac{uu_x}{u_{ref}}\right| \left|\frac{u_x}{u_{ref}}\right|^{\beta-2} \left(\sum_{a=1}^{n_{fun}} \left|j\frac{\partial N_a}{\partial x}\right|\right)^{-\beta} \cdot uu_x\right) = (w, f) \tag{3.22}$$

and when Z is a residual-based operator it becomes:

$$(w, u_t + uu_x - \nu u_{xx}) + \left(w_x, \left|\frac{u_t + uu_x - \nu u_{xx} - f}{u_{ref}}\right| \left|\frac{u_x}{u_{ref}}\right|^{\beta-2} \left(\sum_{a=1}^{n_{fun}} \left|j\frac{\partial N_a}{\partial x}\right|\right)^{-\beta} \cdot uu_x\right) = (w, f) \tag{3.23}$$

The results for $YZ\beta$ are shown in Fig. 3.3 and Fig. 3.4.

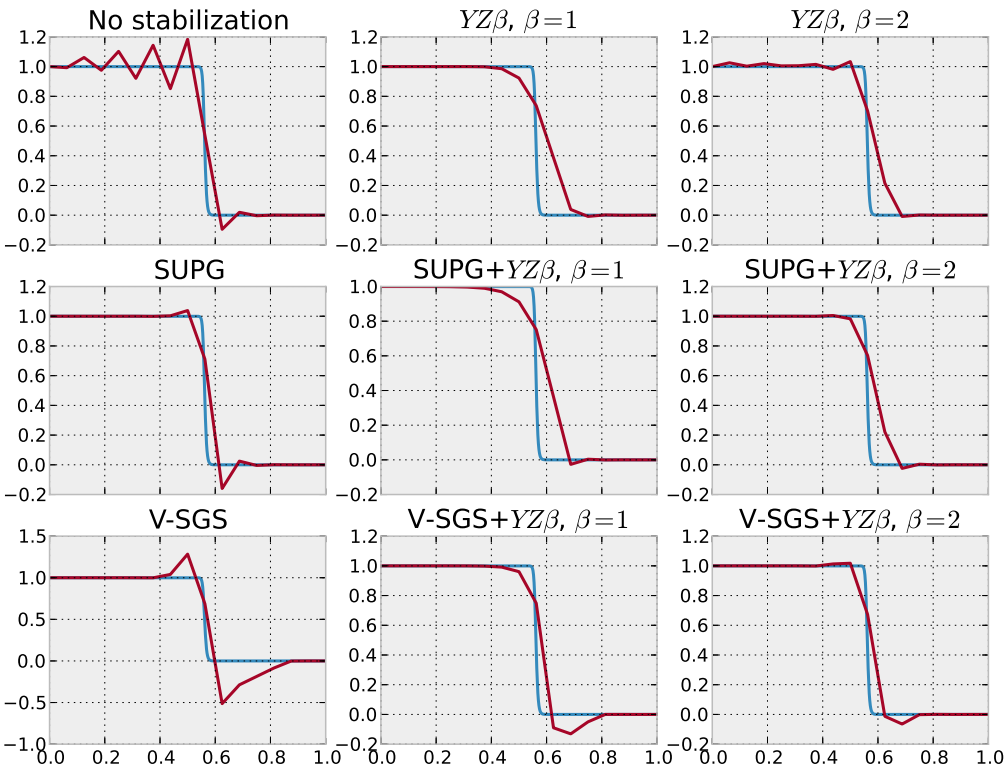

Figure 3.3: $YZ\beta$ with and without stabilization on initial discontinuity test case at $t = 0.2$, using 16 elements plotted in red; the DNS is plotted in blue.

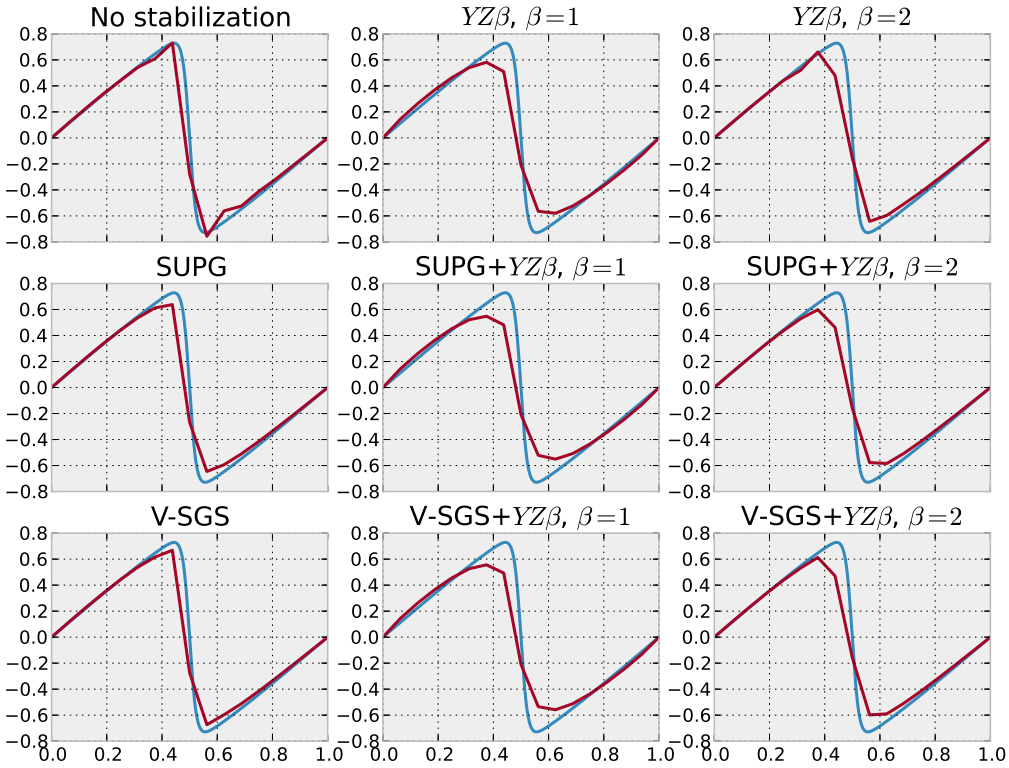

Figure 3.4: $YZ\beta$ with and without stabilization on the steepening wave test case at $t = 0.4$, using 16 elements plotted in red; the DNS is plotted in blue.

3.3 Summary of results

As can be seen from the results in this chapter, both shock-capturing methods try to such that it does not affect smooth parts of the solution but does stabilize the solution near discontinuities.

For the steepening wave test case, adding shock capturing is not useful. It can be seen in Fig. 3.2 and 3.4 that stabilization is enough, extra shock-capturing only adds diffusion making the solution less accurate (note that the result still depends on the mesh resolution, for a refined mesh the situation might be different). In the other test case, with the initial discontinuity, one can see the benefit of shock capturing. Fig 3.1 and Fig. 3.3 show shock-capturing in action, over- and undershoots are eliminated, oscillations disappear and a smooth solution is obtained. The main downside of the shock-capturing methods is also immediately clear: the shock is smeared out over multiple elements. It can also be seen that DCDD is more diffusive than $YZ\beta$.

Why these shock-capturing methods are designed the way they are and the reason they work is not always clear. Determining the shock-capturing parameters seems to be more art than science. That is why the next chapters treat the development of shock-capturing parameters that are consistent with multiscale theory.

Chapter 4

Multiscale shock-capturing for stationary shocks

In this chapter an attempt will be made to explain the working of DCDD and $YZ\beta$ shock-capturing from a multiscale perspective. To what extent do they approximate the small-scale terms needed to be consistent with multiscale theory?

Furthermore a new shock-capturing method is proposed which reproduces the integrated effect of those small-scale terms for a shock that is stationary with respect to the mesh.

4.1 Stationary shock problem

Focus here will be on pure shock dynamics, for that the one-dimensional inviscid Burgers' equation is used:

$$\frac{\partial u}{\partial t} + \frac{1}{2}\frac{\partial u^2}{\partial x} = 0. \tag{4.1}$$

Now take the case depicted in Fig. 4.1, with the inviscid Burgers' equation as the governing equation, that discontinuity will travel to the right as time progresses. Define a control domain around the shock and let this control domain move with the shock, it will move with velocity $\dot{x}$ (which will be the same velocity as the shock speed). Because the control domain will be moving with the shock, the equation inside that moving control domain will look a little different. Integrating (4.1) and rewriting it for the moving control domain yields

$$\int_D \frac{\partial u}{\partial t} dD + \int_D \frac{\partial \left(\frac{u^2}{2} - \dot{x}u\right)}{\partial x} dD = 0 \tag{4.2}$$

$$\iff \int_D \frac{\partial u}{\partial t} dD + \int_C \left(\frac{u^2}{2} - \dot{x}u\right) \cdot n \; dC = 0. \tag{4.3}$$

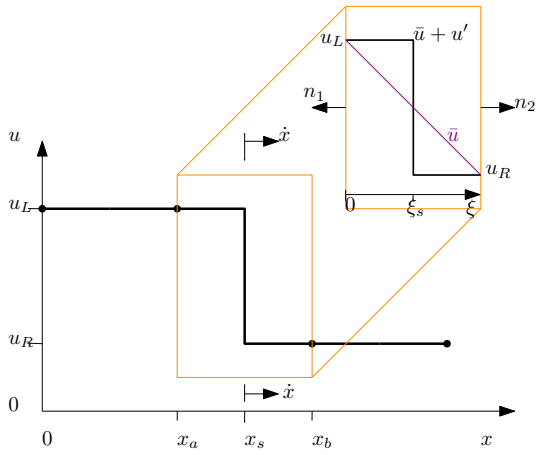

Figure 4.1: Sketch of the inviscid Burgers test case.

This control domain is basically the domain from x_a to x_b in Fig. 4.1, and the contours C are the points x_a and x_b. Note that the figure is a snapshot and that the entire control domain will be moving as the solution is time dependent. It is not defined in the beginning where exactly within the control domain the shock should be, but the control domain should move with the shock. This can be enforced by setting

$$\int_D \frac{\partial u}{\partial t} dD = 0. \tag{4.4}$$

Under that condition, only the second term in (4.3) is left and, using the conventions from Fig. 4.1, that becomes

$$\left(\frac{u_L^2}{2} - \dot{x}u_L\right) \cdot n_1 + \left(\frac{u_R^2}{2} - \dot{x}u_R\right) \cdot n_2 = 0. \tag{4.5}$$

With $n_1 = -1$ and $n_2 = 1$ the result is

$$-\left(\frac{u_L^2}{2} - \dot{x}u_L\right) + \left(\frac{u_R^2}{2} - \dot{x}u_R\right) = 0, \tag{4.6}$$

$$\Rightarrow \dot{x} = \frac{\frac{u_R^2}{2} - \frac{u_L^2}{2}}{u_R - u_L} = \frac{u_L + u_R}{2}. \tag{4.7}$$

The solution can now be split up into a large- and small-scale solution: $u = \bar{u} + u'$, in the variational form (4.1) now becomes

$$(\bar{w}, \bar{u}_t + u'_t) + \left(\bar{w}, \frac{\partial}{\partial x}\left(\frac{(\bar{u}+u')^2}{2} - \dot{x}(\bar{u}+u')\right)\right) = 0, \tag{4.8}$$

setting $\bar{u}_t$ to zero and also assuming for now that u'_t is negligible results in

$$\left(\bar{w}, \frac{\partial}{\partial x}\left(\frac{\bar{u}^2}{2} - \dot{x}\bar{u}\right)\right) + \left(\bar{w}, \frac{\partial}{\partial x}\left(\bar{u}u' + \frac{u'^2}{2} - \dot{x}u'\right)\right) = 0, \tag{4.9}$$

and the large-scale residual is now defined as

$$R = \frac{\partial}{\partial x}\left(\frac{\bar{u}^2}{2} - \dot{x}\bar{u}\right). \tag{4.10}$$

By using integration by parts, (4.9) can be written as

$$\left(\bar{w}_x, \dot{x}\bar{u} - \frac{\bar{u}^2}{2}\right) + \left(\bar{w}_x, \dot{x}u' - \bar{u}u' - \frac{u'^2}{2}\right) = 0. \tag{4.11}$$

In the ideal case where $\bar{u}$ is nodally exact, the large-scale solution will just be a linear interpolation between u_L and u_R:

$$\bar{u} = u_L + \frac{u_R - u_L}{h}\xi, \tag{4.12}$$

and its derivative with respect to the local spatial coordinate ξ will be

$$\bar{u}_\xi = \frac{u_R - u_L}{h}. \tag{4.13}$$

Note that here ξ is defined as $\xi = x - x_a$ and $0 \leq \xi \leq h$, ξ here is not the same as the reference element coordinate, furthermore h is defined as $h = x_b - x_a$ (the length of the element containing the shock).

The small-scale solution u' is discontinuous, and depends on the location of the discontinuity ξ_s. For $\xi \leq \xi_s$:

$$u'_{\xi\leq\xi_s} = u_L - \bar{u} \tag{4.14}$$

$$\Rightarrow u'_{\xi\leq\xi_s} = -\frac{u_R - u_L}{h}\xi, \tag{4.15}$$

and for $\xi > \xi_s$:

$$u'_{\xi>\xi_s} = u_2 - \bar{u} \tag{4.16}$$

$$\Rightarrow u'_{\xi>\xi_s} = (u_R - u_L)\left(1 - \frac{\xi}{h}\right). \tag{4.17}$$

Knowing $\dot{x}$ and $\bar{u}$, the large-scale residual (4.10) can now be written out as

$$\bar{R} = \frac{\partial}{\partial\xi}\left(\frac{1}{2}\left(u_L + \frac{u_R - u_L}{h}\xi\right)^2 - \frac{\frac{u_R^2}{2} - \frac{u_L^2}{2}}{u_R - u_L}\left(u_L + \frac{u_R - u_L}{h}\xi\right)\right) \tag{4.18}$$

$$= u_L\frac{u_R - u_L}{h} - \frac{u_R^2 - u_L^2}{2h} + \frac{(u_R - u_L)^2}{h^2}\xi \tag{4.19}$$

$$= -\frac{(u_L - u_R)^2(h - 2\xi)}{2h^2}. \tag{4.20}$$

From (4.9) it is easy to see that the small-scale terms contributing to the large scale solution are represented by

$$\left(\bar{w}_x, \dot{x}u' - \bar{u}u' - \frac{u'^2}{2}\right) \tag{4.21}$$

the analytical expressions of these terms are known for this test case, they are plotted in Fig. 4.2. The next step is comparing the exact small-scale terms to the shock-capturing terms.

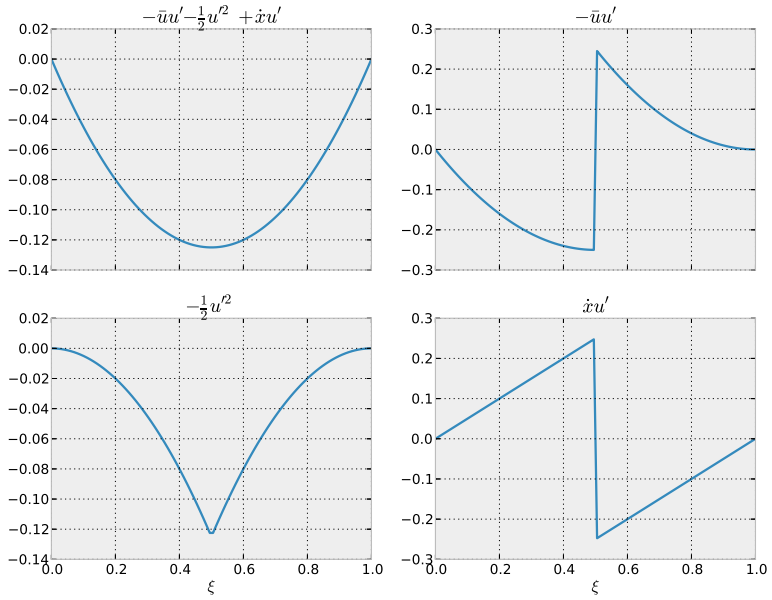

Figure 4.2: Exact small scale terms that contribute to the large-scale solution, when $u_L = 1$, $u_R = 0$ and $\xi_s = 0.5$.

4.2 Existing shock-capturing terms for the stationary shock problem

Discontinuity-Capturing Directional Dissipation

The DCDD-term for the present test problem, as defined in section 3.2.1, reduces to

$$(w_x, \nu_{shock} u_x) \tag{4.22}$$

$$= \left(w_x, \frac{1}{2u_{ref}^2} \left(\frac{2}{\sum_{a=1}^{n_{funs}} |j \cdot \nabla N_a|} \right)^2 (||\nabla ||u||\,||)\, ||u||^2 u_x \right). \tag{4.23}$$

And when using linear shape functions in 1D, this can be even further reduced to

$$(w_x, \nu_{shock} u_x) \tag{4.24}$$

$$= \left(w_x, \frac{1}{2u_{ref}^2} h^2 \left|\left| \frac{\partial ||u||}{\partial x} \right|\right| ||u||^2 u_x \right). \tag{4.25}$$

$YZ\beta$ shock-capturing

The $YZ\beta$ term, given in section 3.2.2, for this problem reduces to

$$(w_x, \nu_{shock} u_x) \tag{4.26}$$

$$= \left(w_x, \frac{\left|\left|\frac{Z}{u_{ref}}\right|\right| \left|\left|\frac{\bar{u}_x}{u_{ref}}\right|\right|^{\beta-2}}{\left(\sum_{a=1}^{n_{funs}} |j \cdot \nabla N_a|\right)^{\beta}} u_x \right), \tag{4.27}$$

where Z is either the advective part of the original problem L_{adv} or the residual R. In this test case Z will be taken to be the large-scale residual and taking linear shape functions, (4.27) can be further reduced to

$$\left(\bar{w}_x, \left(\frac{h}{2}\right)^{\beta} \left|\left|\frac{\bar{R}}{u_{ref}}\right|\right| \left|\left|\frac{\bar{u}_x}{u_{ref}}\right|\right|^{\beta-2} \bar{u}_x \right). \tag{4.28}$$

4.3 Comparing shock-capturing terms to exact analytic terms

In the case of linear shape functions, the term (4.21) will in fact be the integral of $-\bar{u}u' - 1/2u'^2 + \dot{x}u'$ multiplied by some constant as in this case the derivative of the test functions will be just constants. For a shock-capturing term to have the correct effect, the integral value, that is the term integrated over the element, needs to approximate that of the exact small-scale effect given by (4.21). First define this integral of the exact small-scale effect as:

$$S = \int_0^{\xi_s} (-\bar{u}u' - 1/2u'^2 + \dot{x}u')d\xi + \int_{\xi_s}^{h} (-\bar{u}u' - 1/2u'^2 + \dot{x}u')d\xi, \tag{4.29}$$

filling in the exact expressions for $\bar{u}$, u' and $\dot{x}$ and integrating results in

$$S = -\frac{1}{12} h (u_L - u_R)^2. \tag{4.30}$$

Note that this expression is independent of the exact position of the discontinuity ξ_s. Taking $\bar{u}_x$ as the derivative of the large-scale solution over the element with the shock, one can write out the following relation

$$\bar{u}_x = \frac{u_R - u_L}{h}, \tag{4.31}$$

$$\Rightarrow u_L - u_R = -\bar{u}_x h. \tag{4.32}$$

Using expression (4.32), equation (4.30) can be rewritten as

$$S = -\frac{1}{12} \bar{u}_x^2 h^3. \tag{4.33}$$

The surface S as a function of $\bar{u}_x$ and h is shown in Fig. 4.3. In Fig. 4.4 the surface representing the value of the $YZ\beta$ shock-capturing term, with $\beta = 1$ integrated over the

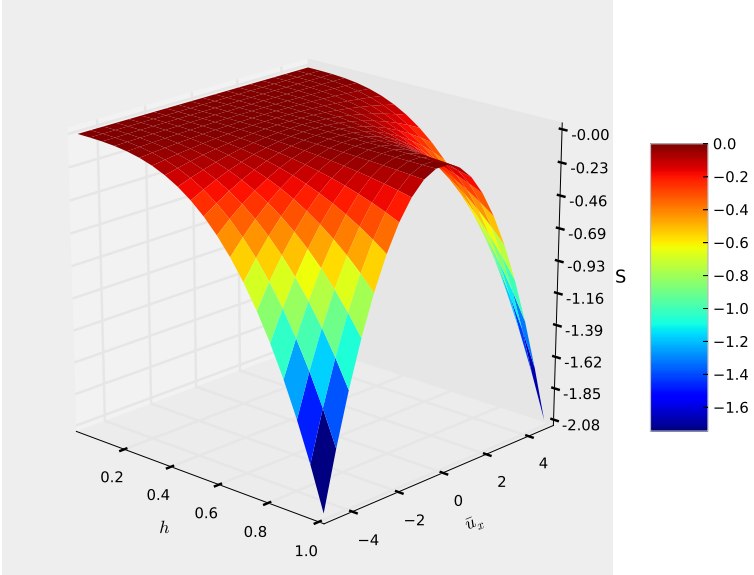

Figure 4.3: Integral value of the exact small scale terms as a function of the element size h and the gradient over the element given by $\bar{u}_x = \frac{u_R - u_L}{h}$.

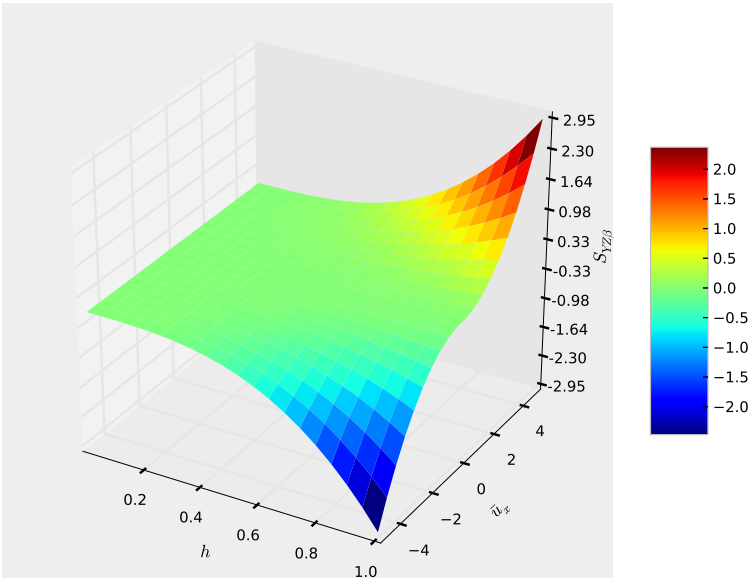

Figure 4.4: Integral value of the $YZ\beta$ term, with $\beta = 1$ as a function of the element size h and the gradient over the element given by $\bar{u}_x = \frac{u_R - u_L}{h}$.

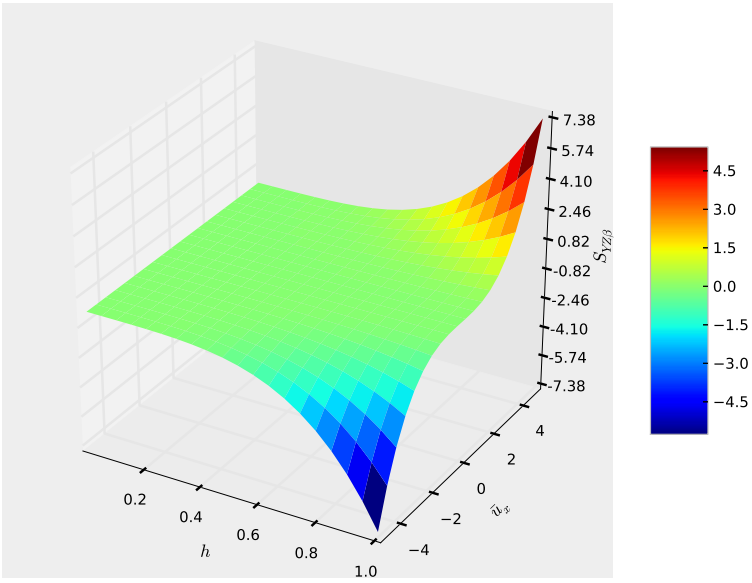

Figure 4.5: Integral value of the $YZ\beta$ term, with $\beta = 2$, as a function of the element size h and the gradient over the element given by $\bar{u}_x = \frac{u_R - u_L}{h}$.

element as a function of $\bar{u}_x$ and h is plotted. The same with $\beta = 2$ is shown in Fig. 4.5. The perfect shock-capturing operator for this test case would produce exactly the surface given in Fig. 4.3. Obviously the YZB-term is not the perfect shock-capturing parameter here. The difference between the two surfaces computed as $S_{exact} - S_{YZ\beta}$ is plotted in Fig. 4.6 for $\beta = 1$ and in Fig. 4.7 for $\beta = 2$. The most obvious difference between the exact small-scale term and the $YZ\beta$ term is that the integrated value of the former is always negative, irrespective of the sign of $\bar{u}_x$ while the $YZ\beta$ term switches sign. Note that $\bar{u}_x > 0$ means a step up and $\bar{u}_x < 0$ means a step down as depicted in Fig. 4.1. In this thesis we will focus on $\bar{u}_x < 0$, as a step up (expansion) would be unphysical in the context of fluid dynamics shocks. Even in the part of the domain where $\bar{u}_x < 0$, however the $YZ\beta$ term does not fully display the ideal behaviour. In Fig. 4.8 some cross-sections of the surface plots are shown where for each plot h is fixed. In Fig. 4.9 cross-sections from the surface plots are depicted where in each plot $\bar{u}_x$ is fixed. Clearly the dependency of S on $\bar{u}_x$, u_L and h is not fully captured by the $YZ\beta$ term. Furthermore for different values of $\bar{u}_x$, u_L and h, different values of β need to be found to get the best results. All of the aforementioned plots were also generated for DCDD but they are not printed here because they were very far off.

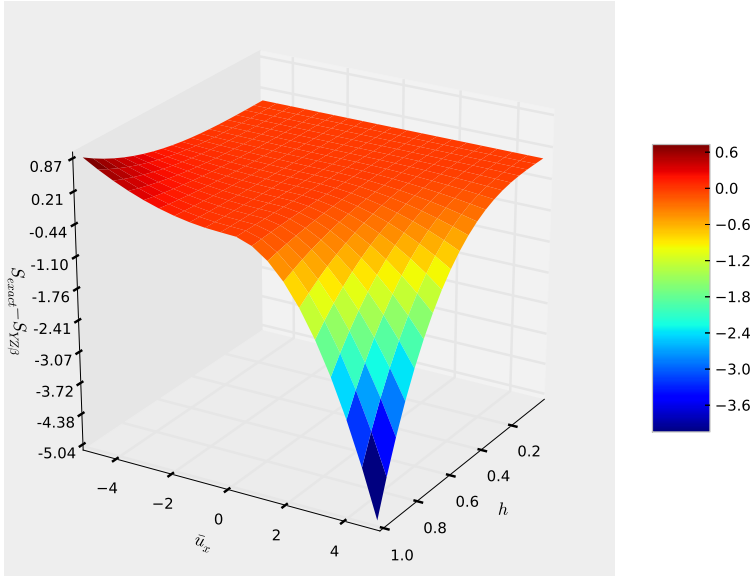

Figure 4.6: Difference in integral value between the exact terms and the $YZ\beta$-term with $\beta = 1$. The difference is given as $S_{exact} - S_{YZ\beta}$.

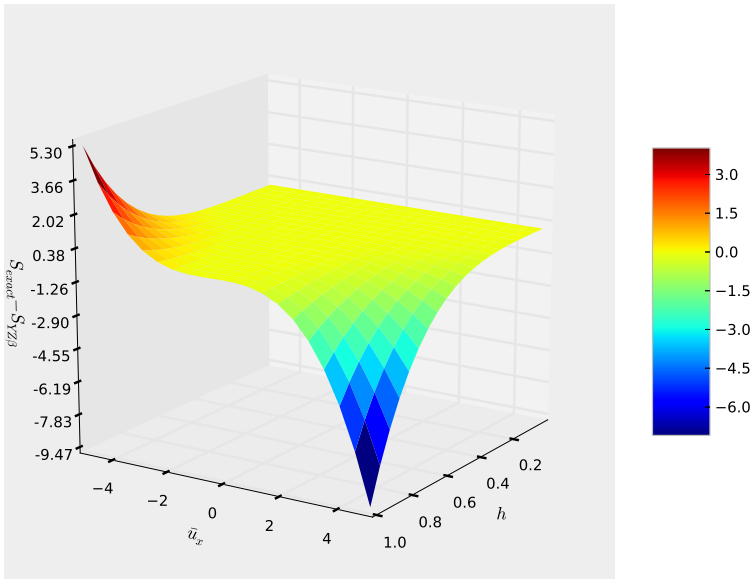

Figure 4.7: Difference in integral value between the exact terms and the $YZ\beta$-term with $\beta = 2$. The difference is given as $S_{exact} - S_{YZ\beta}$.

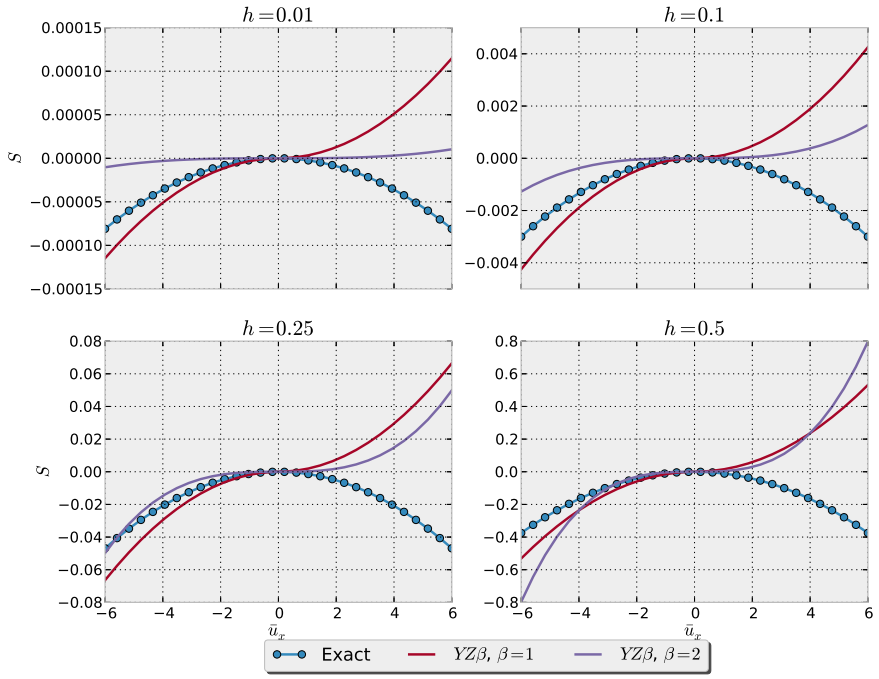

Figure 4.8: Comparison of the integrated exact and $YZ\beta$ terms for different values of h with $u_L = 1$ and u_R a function of $\bar{u}_x$.

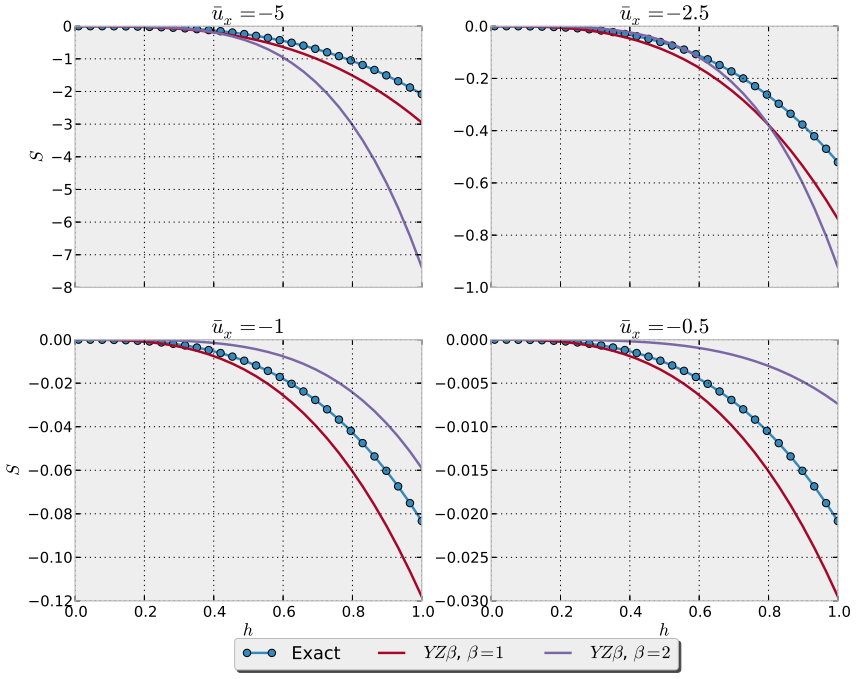

Figure 4.9: Comparison of the integrated exact and $YZ\beta$ terms for different values of $\bar{u}_x$ with $u_L = 1$ and u_R a function of h.

4.4 Multiscale shock-capturing (MSC)

From Fig. 4.8 and Fig. 4.9 it is clear that the $YZ\beta$ shock-capturing parameter with β either equal to 1 or 2 only approximates the exact value of the small-scale contribution, for particular combinations of the element size and the height of the discontinuous step. Based on the findings of the previous sections, one can now construct a shock-capturing operator that mimics the behaviour of the small-scale term $(w_x, -\bar{u}u' - {}^1\!/_2 u'^2)$. It is not required that this shock-capturing operator produces exactly the same result as in Fig. 4.2, as long as the value integrated over the element approximates that of the exact term integrated over the element domain. In other words the behaviour shown in Fig. 4.3 should be approximated by this new shock-capturing operator.

From the previous section it is also clear that the value of the exact small-scales integrated over the element is a function of u_L, u_R, h. Or, by rewriting u_R as $u_R = (\bar{u}_x h + u_L)$, and denoting u_L, the inflow velocity, as u_{ref}, the value of the small-scale terms integrated over the element can be seen as a function of $\bar{u}_x$, h and u_{ref}. And so it seems natural to take the following form as a starting point for the new shock-capturing term

$$\text{MSC term} = \left(\bar{w}_x, \underbrace{u_{ref}^{\alpha} \bar{u}_x^{\beta} h^{\gamma} R^{\delta}}_{S_{MSC}} \right) \tag{4.34}$$

$$= \left(\bar{w}_x, \underbrace{\left(u_{ref}^{\alpha} \bar{u}_x^{\beta-1} h^{\gamma} R^{\delta} \right)}_{\nu_{MSC}} \bar{u}_x \right) . \tag{4.35}$$

The relation between the exponents α, β, γ and δ is found by enforcing dimensional consistency. Interpreting the solution of the Burgers' equation as a velocity, with units length per time $[{}^L\!/_T]$ means that the derivatives with respect to time will have units $[{}^L\!/_{T^2}]$ and the derivatives with respect to x will have dimension $[{}^1\!/_{T^2}]$. Where L and T signify length- and timescales respectively. The original strong formulation of the problem

$$\frac{\partial u}{\partial t} + u \frac{\partial u}{\partial x} = 0 \tag{4.36}$$

will therefore be in units $[{}^L\!/_{T^2}]$. If a term is added to the formulation, it should be dimensionally consistent. Term (4.35) is a result of an integration-by-parts operation that brings the derivative to the test functions, originally the variational formulation for this specific term would have been

$$\left(w, \frac{\partial}{\partial x} \left(u_{ref}^{\alpha} \bar{u}_x^{\beta} h^{\gamma} R^{\delta} \right) \right) . \tag{4.37}$$

By applying integration by parts (assuming the term introduced here does not produce jump terms at the boundaries) one then gets

$$- \left(\bar{w}_x, u_{ref}^{\alpha} (\bar{u}_x)^{\beta} h^{\gamma} R^{\delta} \right) . \tag{4.38}$$

This means that the units of the term $\frac{\partial}{\partial x}\left(u_{ref}^{\alpha}\bar{u}_x^{\beta}h^{\gamma}R^{\delta}\right)$ have to be $[L/T^2]$ and after integration, consequently the term $u_{ref}^{\alpha}(\bar{u}_x)^{\beta}h^{\gamma}R^{\delta}$ will have units $[L^2/T^2]$. So now a relation between the three exponents can be set up:

$$\underbrace{\left[\frac{L}{T}\right]^{\alpha}}_{u_{ref}^{\alpha}}\underbrace{\left[\frac{1}{T}\right]^{\beta}}_{\bar{u}_x^{\beta}}\underbrace{[L]^{\gamma}}_{h^{\gamma}}\underbrace{\left[\frac{L}{T^2}\right]}_{R^{\delta}} = \left[\frac{L^2}{T^2}\right]. \tag{4.39}$$

Collecting the exponents for $[L]$ and $[T]$ yields a system of two equations,

$$\begin{cases}\alpha+\gamma+\delta=2\\ \alpha+\beta+2\delta=2,\end{cases} \tag{4.40}$$

now γ and δ can be expressed in function of α and β:

$$\begin{cases}\gamma=1-\frac{1}{2}\alpha+\frac{1}{2}\beta\\ \delta=1-\frac{1}{2}\alpha-\frac{1}{2}\beta\end{cases} \tag{4.41}$$

Using these expressions for γ and δ, the MSC term can be rewritten with only α and β as unknown exponents:

$$u_{ref}^{\alpha}\bar{u}_x^{\beta}h^{1-1/2\alpha+1/2\beta}R^{1-1/2\alpha-1/2\beta}. \tag{4.42}$$

The only thing left is to optimise α and β such that the value of this term, when integrated over the element domain, S_{MSC} approximates S (see Fig. 4.3), ideally the result would be:

$$\int_0^h u_{ref}^{\alpha}\bar{u}_x^{\beta}h^{1-1/2\alpha+1/2\beta}R^{1-1/2\alpha-1/2\beta}d\xi = S = -\frac{1}{12}\bar{u}_x h^3. \tag{4.43}$$

And it turns out that $\alpha=0$, $\beta=-2$, $\gamma=0$ and $\delta=2$ yields a perfect fit. With those exponents the integral of S_{MSC} over the element is an exact reformulation of S (see Eq. 4.33). The MSC term has now been determined to be:

$$\text{MSC term } = \left(\bar{w}_x, -R^2\bar{u}_x^{-2}\right) \tag{4.44}$$

As (4.44) is a residual-based term, the formulation of the problem is consistent. The term is dimensionally consistent, and there is no need for the tweaking the exponents or coefficients.

4.5 Results

The new MSC shock-capturing term will now be evaluated by trying it out on the model problem sketched out in Fig. 4.1 with $u_L=2$ and $u_R=1$ (similar to the model problem defined in section 3.1.1 except now the mesh is moving with the shock). To quantify the results, the error must be measured. This will be done in two ways, in the L^2 norm and in

the H^1 norm. Let u be the exact solution and u^h be the approximate solution (the outcome of the computations) on the domain Ω, then the L^2 error is defined as:

$$e_{L^2(\Omega)} = ||u - u^h||_{L^2(\Omega)} = \left(\int_\Omega (u - u^h)^2 d\Omega \right)^{\frac{1}{2}}, \tag{4.45}$$

and the H^1 error is defined as:

$$e_{H^1(\Omega)} = ||u - u^h||_{H^1(\Omega)} = \left(||u - u^h||^2_{L^2(\Omega)} + \sum_{i=1}^{d} \left|\left| \frac{\partial u}{\partial x_i} - \frac{\partial u^h}{\partial x_i} \right|\right|^2_{L^2(\Omega)} \right)^{\frac{1}{2}}, \tag{4.46}$$

where d is the number of dimensions of the domain. In all the computations discussed below, the time discretization used is a 3^{rd} order Runge-Kutta scheme where the mass matrix is lumped and is updated at every time step. To prevent the results and conclusions from being influenced by errors coming from the time discretization, the Courant number in the computations is always kept fixed at 0.25. The Courant number is computed as

$$Cr = \frac{u_{av} \Delta t}{h}, \tag{4.47}$$

where u_{av} is the average velocity in the domain. For the model problem with $u_L = 2$ and $u_R = 1$ this becomes $u_{av} = 3/2$.

4.5.1 Results of stabilization and shock-capturing methods

An overview of the results is given in Fig 4.10, in each computation only one stabilization or shock-capturing method was used (no combinations of both). It is clear from this figure that the MSC term works well for this case, the other shock-capturing methods smear the shock out over multiple elements and also attenuate the shock strength as time progresses (the shock strength should remain the same here). In Fig. 4.11 the L^2 and H^1 error is plotted for different stabilization and shock-capturing methods. The element size was varied from $1/5$ until $1/65$ and the time step was varied as well to ensure the Courant number is equal to 0.25 in every computation. The data used to in Fig. 4.11 is also given in Table D.1 for the results at $t = 0.1$ and Table D.2 for the results at $t = 0.5$.

4.5.2 SUPG stabilization with shock-capturing

The different shock-capturing methods can be used in combination with stabilization, in Fig. 4.12 the errors from computations where SUPG stabilization was combined with different shock-capturing methods are plotted. The data used in Fig. 4.12 is shown in Table D.3 ($t = 0.1$) and Table D.4 ($t = 0.5$).

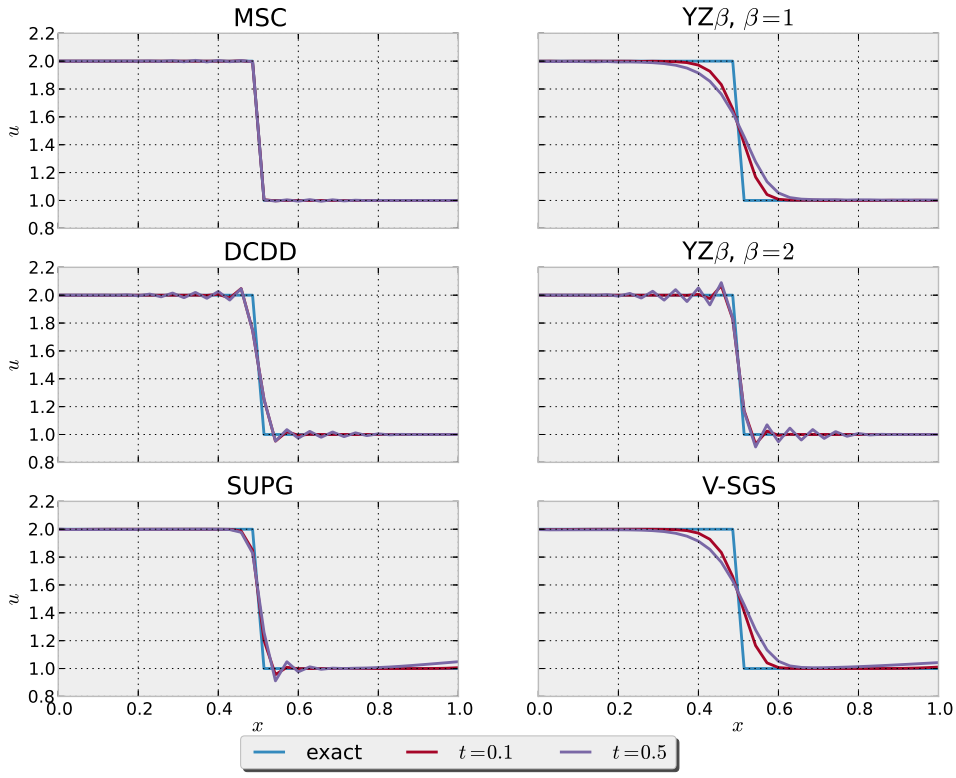

Figure 4.10: Overview of the results at time $t = 0.1$ and $t = 0.5$. In all the runs, the Courant number was kept at $Cr = 0.25$ ($\Delta t = {}^{h}/_{6}$ and the average velocity $u_{av} = {}^{3}/_{2}$).

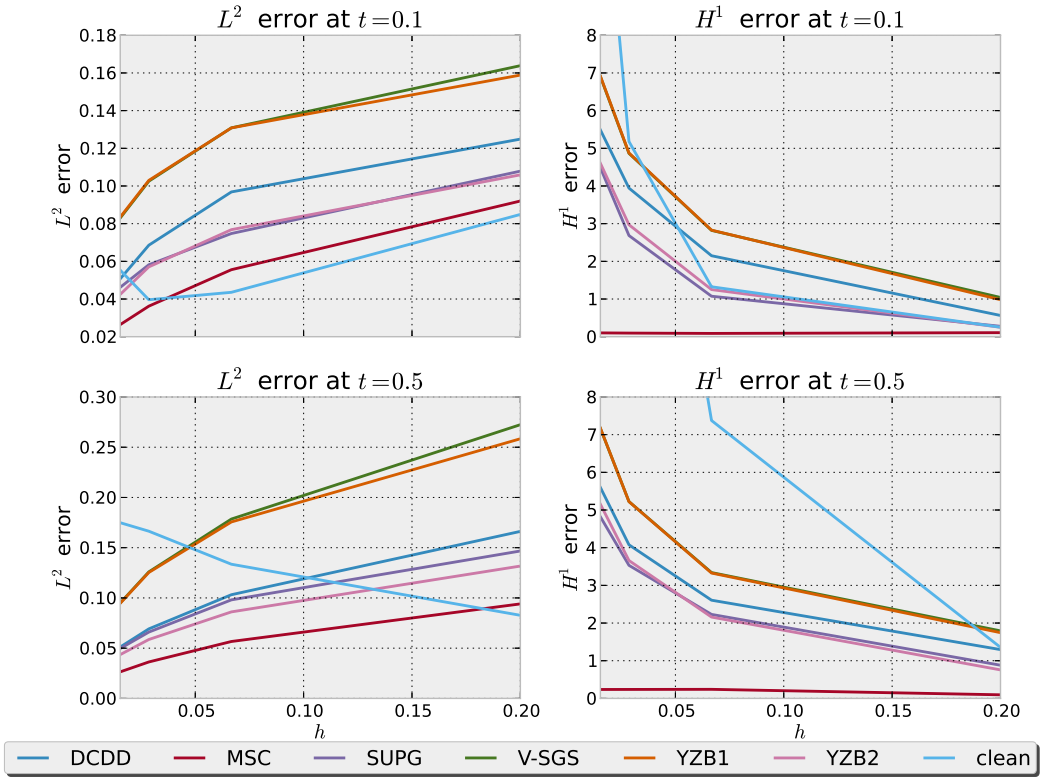

Figure 4.11: Overview of the L^2 and H^1 errors at time $t = 0.1$ and $t = 0.5$. In all the runs, the Courant number was kept at $Cr = 0.25$ ($\Delta t = h/6$ and the average velocity $u_{av} = 3/2$).

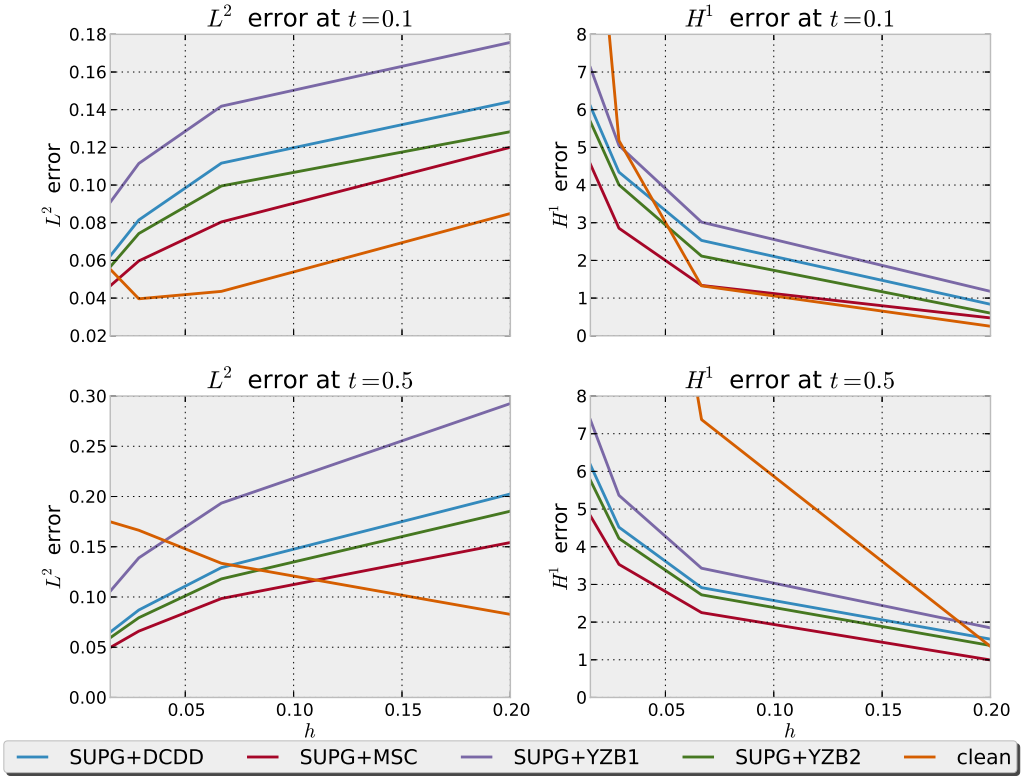

Figure 4.12: Overview of the L^2 and H^1 errors at time $t = 0.1$ and $t = 0.5$ with SUPG stabilization and different shock-capturing methods. In all the runs, the Courant number was kept at $Cr = 0.25$ ($\Delta t = h/6$ and the average velocity $u_{av} = 3/2$).

4.5.3 SUPG stabilization with shock-capturing and shock-detection

The results shown in Fig. 4.12 are obtained by simply activating both SUPG stabilization and the shock capturing method of choice over the entire domain. In the region around the shock, both the stabilization and the shock-capturing will be active. To be consistent with multiscale theory, it is better to choose to activate either the stabilization or the shock-capturing operator to represent the unresolved scales. In Fig. 4.13 the errors are shown for computations where a shock detector was used. When the shock detector detects a shock, it turns off the stabilization on the element in which the shock was detected and it turns on the shock-capturing method of choice. The shock detector in this case is a simple gradient threshold.

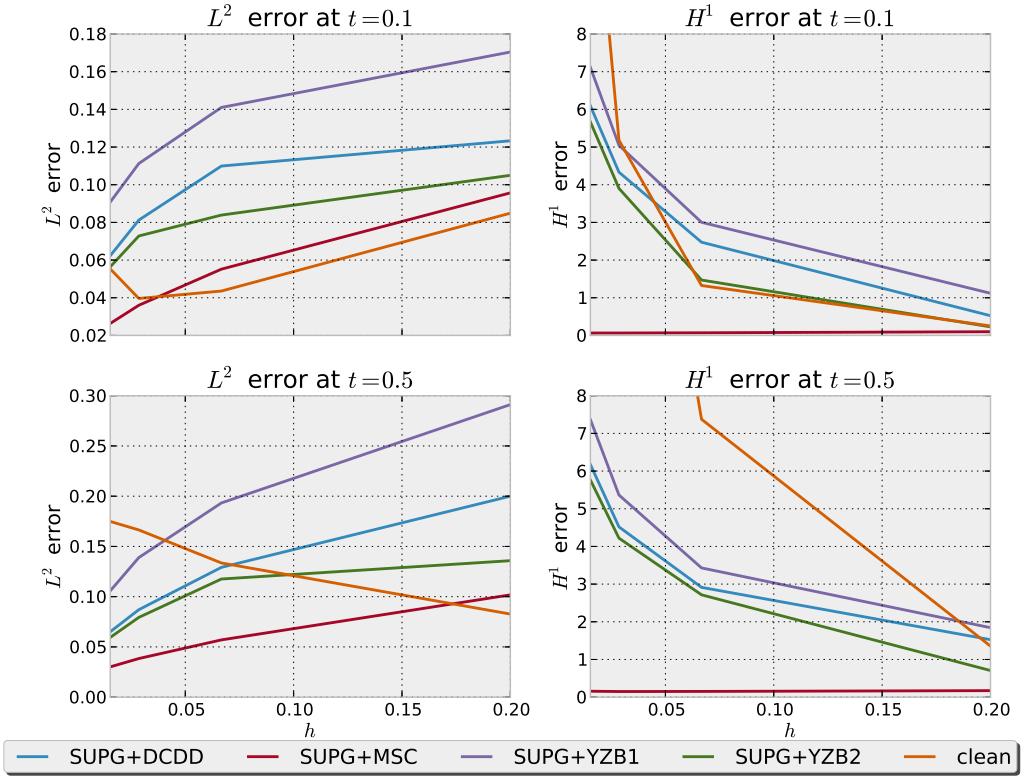

Figure 4.13: Overview of the L^2 and H^1 errors at time $t = 0.1$ and $t = 0.5$ for SUPG stabilized computations with shock detection. In all the runs, the Courant number was kept at $Cr = 0.25$ ($\Delta t = {}^{h}/_{6}$ and the average velocity $u_{av} = {}^{3}/_{2}$).

4.5.4 V-SGS stabilization with shock-capturing

In Fig 4.14, the errors from computations where V-SGS stabilization was combined with different shock-capturing methods are plotted. The data that makes up Fig. 4.14 is printed

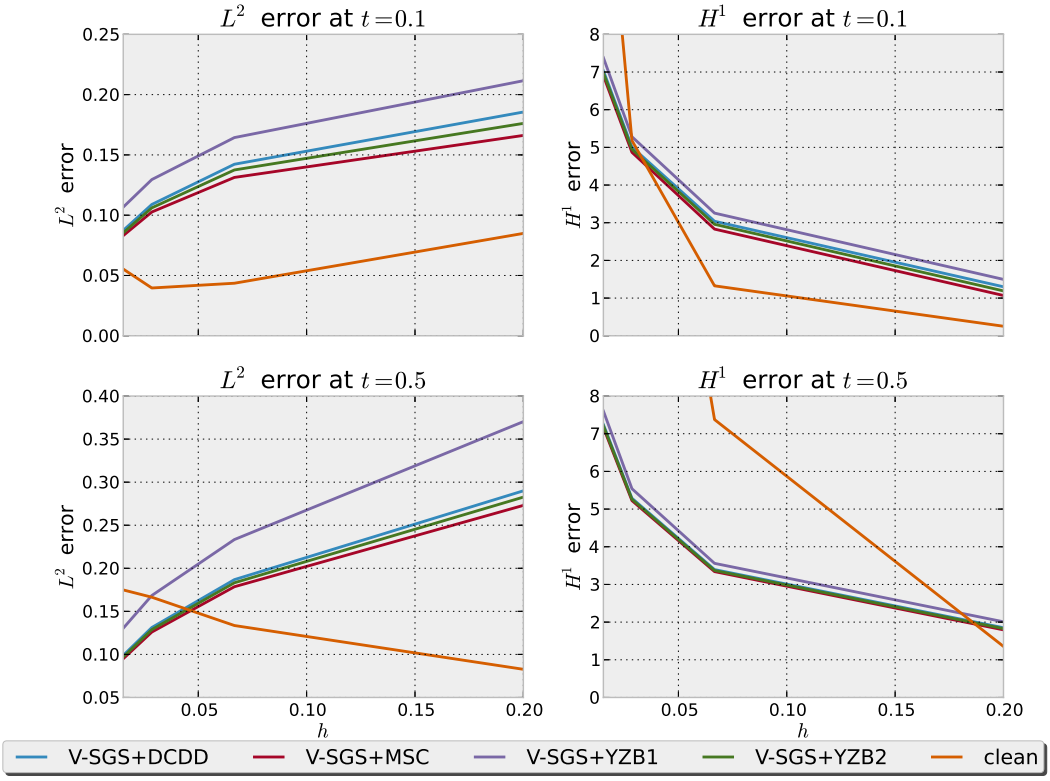

Figure 4.14: Overview of the L^2 and H^1 errors at time $t = 0.1$ and $t = 0.5$ for V-SGS stabilized computations. In all the runs, the Courant number was kept at $Cr = 0.25$ ($\Delta t = {}^{h}/_{6}$ and the average velocity $u_{av} = {}^{3}/_{2}$).

in Table D.7 ($t = 0.1$) and D.8 ($t = 0.5$).

4.5.5 V-SGS stabilization with shock-capturing and shock-detection

The computations done in this section are almost the same as those in section 4.5.4, except here shock-detection is used. The L^2 and H^1 errors are shown in Fig. 4.15 and the data is printed in Table D.9 and Table D.10.

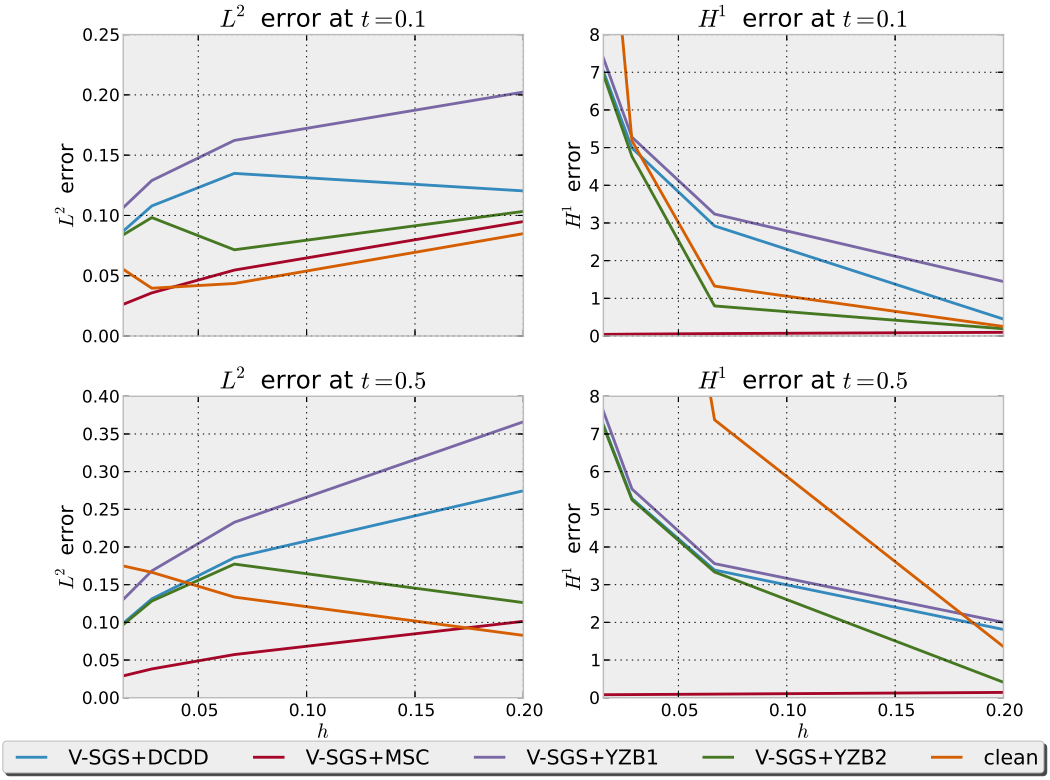

Figure 4.15: Overview of the L^2 and H^1 errors at time $t = 0.1$ and $t = 0.5$ for V-SGS stabilized computations with shock-detection. In all the runs, the Courant number was kept at $Cr = 0.25$ ($\Delta t = h/6$ and the average velocity $u_{av} = 3/2$).

4.6 Summary of results

Overall one can see from the results in the previous chapter that the MSC-term does what it was designed to do. It captures the shock accurately and better than any of the other shock-capturing methods in the comparison. It must be noted though that this is a restricted case and that it is also the test case for which MSC was specifically designed. The results above are not sufficient to conclude that MSC holds preference over the other shock-capturing methods

for general cases, they do however confirm that the design methodology works and that MSC works for a stationary normal shock. For MSC, it is illogical to have both it and stabilization turned on in the same element, this is confirmed by the results. For the other methods as well it is not beneficial to have both the shock-capturing and stabilization activated simultaneously for this test case. This not a new observation and usually shock-capturing methods contain a mechanism to prevent a doubling of stabilization and shock-capturing (see for example Hughes and Mallet (1986) or the research of Tezduyar and Rispoli on the use of $YZ\beta$ shock-capturing). Using both stabilization and shock-capturing is beneficial as long as they are not *active* in the same direction at the same time. This can clearly be seen by comparing the results in section 4.5.2 to those in section 4.5.3 (SUPG stabilization plus shock-capturing, without and with shock-detection respectively) and 4.5.4 to the results in section 4.5.5 (V-SGS stabilization plus shock-capturing with and without shock-detection respectively). Also the MSC benefits from stabilization as very small oscillations before and after the shock are cured by the stabilization.

Finally it is interesting to note that for the steady case, the details of u' (the exact shock location within the element) do not matter. Enough information exists to match the integrated effect of u' exactly.

In the next chapter, a more challenging case with a moving shock will be considered.

Chapter 5

Multiscale shock capturing for moving shocks

A sketch of the problem under consideration in this chapter is shown in Fig. 5.1, a discontinuity moving from one element (element 1) to the next element (element 2). This in contrast to Ch. 4, where the shock position was fixed relative to the mesh. At time level n the shock is in element 1 and at the next time level, $n+1$, it is in element 2. The shock-capturing parameter

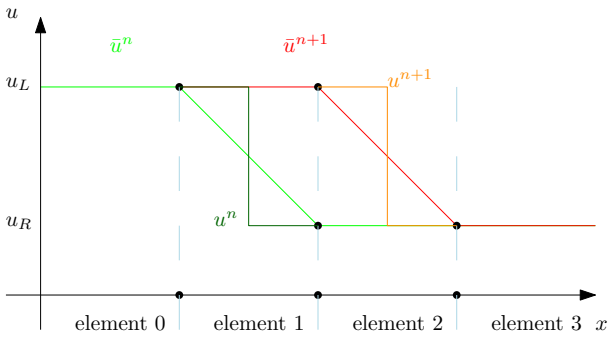

Figure 5.1: 1D diagram of the shock moving from one element to the next. The initial solution is in green (the exact solution in dark green, the large-scale solution in bright green), the solution at the next time step is drawn in red (the exact solution in orange and the large-scale solution in bright red). Below the x-axis, the shape functions active on elements 1 and 2 are drawn.

developed in the previous chapter cannot be expected to work well for moving shocks as it does not take into account any time dependent behaviour of the small scales. The result of applying this steady shock-capturing operator to a moving shock is shown in Fig. 5.2. That is clearly not a good result.

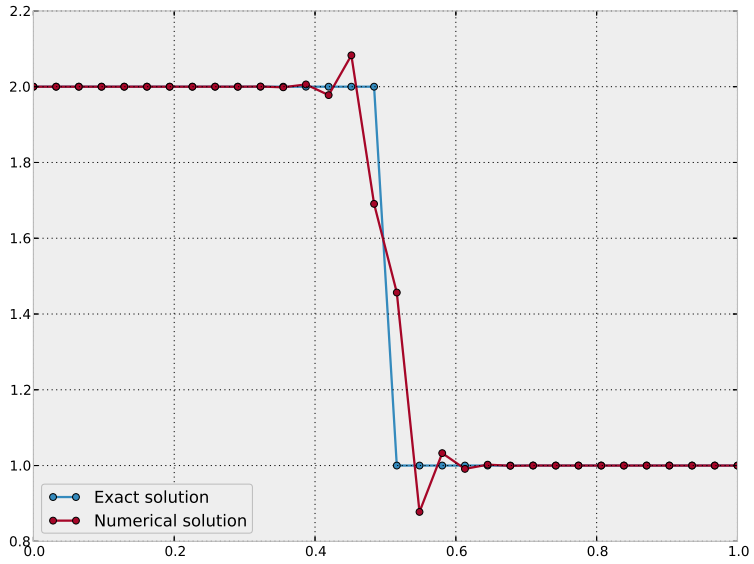

Figure 5.2: Steady shock-capturing operator applied to a moving shock after one time step (explicit Euler time step with $\Delta t = 0.0025$ and $h = 1/31$).

5.1 Space-time formulation

In order to extend the MSC term developed in Chapter 4 to the case of moving shocks, a space-time formulation is natural. In this setting, every space-time element has a domain Q_e^n as depicted in Fig. 5.3, the numbering with index e is analogous to the numbering of elements in Fig. 5.1 and the superscript n denotes that $t \in [t^n, t^{n+1})$ in the element. The space-time representation of the problem at hand is sketched in Fig. 5.4.Furthermore the boundaries in time of the space-time elements are denoted by Ω^n and Ω^{n+1} where n indicates the time level t^n.

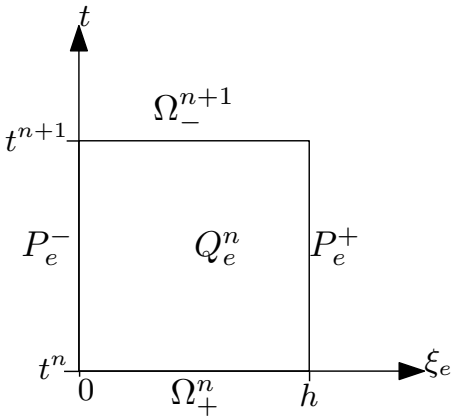

Figure 5.3: Space-time element Q_e^n.

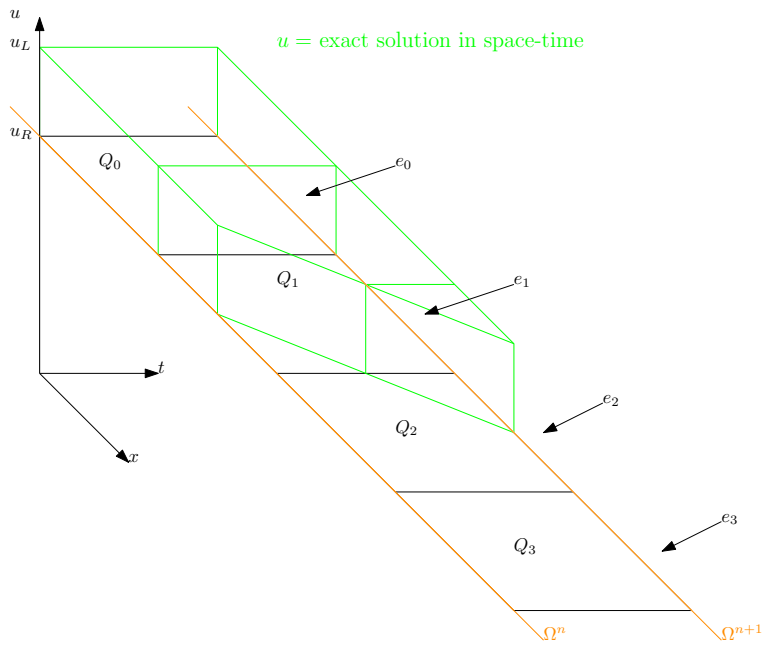

Figure 5.4: Space-time diagram of the moving shock as it moves from one element to the next.

The idea used in Chapter 4 was to get a nodally exact large-scale solution $\bar{u}$ by modelling the small-scales u' such that the integrated effect of the u' terms produced the exact solution u. As a guide to achieving this we first consider expressions for the exact u'. With a moving shock in a space-time setting, this would mean that u' also has a time dependency, the nodally exact large-scale solution in space-time would then be as depicted in Fig. 5.5. The governing equation here is the inviscid Burgers' equation and the problem on a space-time domain $Q = [0, T] \times [0, 1]$ (one dimension in time and one in space), in variational form reads: find $u(t, x) \in \mathcal{S}$ ($\mathcal{S} \subset H^1(Q)$) such that $\forall w(t, x) \in \mathcal{V}$ ($\mathcal{V} \subset H^1(Q)$) the following holds:

$$\left(w, \frac{\partial u}{\partial t}\right)_Q + \left(w, \frac{1}{2}\frac{\partial u^2}{\partial x}\right)_Q = (w, f)_Q, \tag{5.1}$$

with initial condition

$$u(t = 0, x) = \begin{cases} u_L \ \forall x \leq x_s^0 \\ u_R \ \forall x > x_s^0, \end{cases} \tag{5.2}$$

where x_s^0 is the position of the shock at $t = 0$. The boundary conditions are

$$\begin{aligned} u(t, 0) &= u_L, \\ u(t, 1) &= u_R. \end{aligned} \tag{5.3}$$

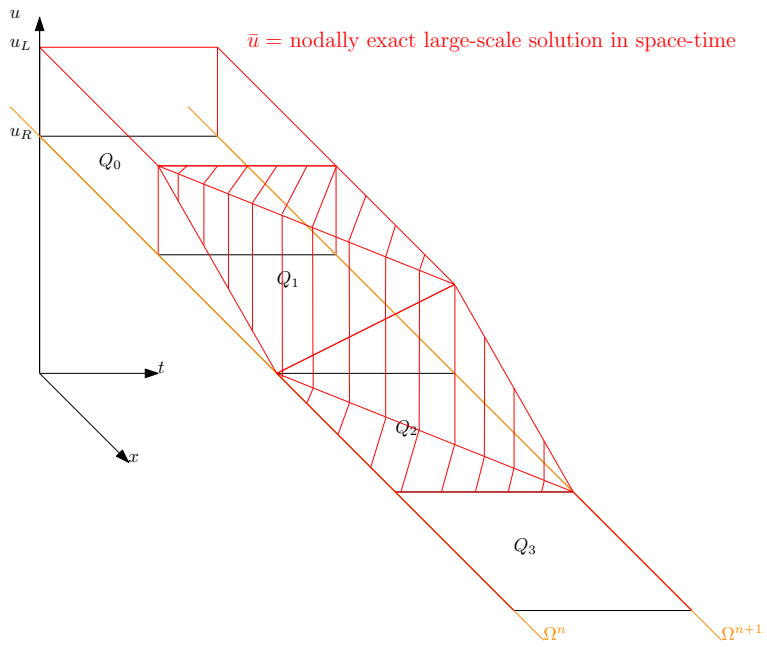

Figure 5.5: The nodally exact large-scale solution in space-time.

5.2 Semi-discrete formulation

Although space-time methods are very elegant, in practice they often require more computational effort to reach the same accuracy as modern semi-discrete methods. To be able to use existing time-discretization schemes, a representation needs to be found that is discrete in time. The first thing that is done to get a semi-discrete formulation is limit the choice of test functions to functions that are independent of time (such that $\frac{\partial w}{\partial t} = 0$). By applying integration by parts, (5.1) can be written as

$$[(w,u)_{\Omega^{n+1}} - (w,u)_{\Omega^n}] - \left(\frac{\partial w}{\partial t}, u\right)_Q + \left[\left(w, \frac{u^2}{2}\right)_{P^+} - \left(w, \frac{u^2}{2}\right)_{P^-}\right] - \left(\frac{\partial w}{\partial x}, \frac{u^2}{2}\right)_Q = (w,f)_Q \tag{5.4}$$

and using the fact that $\frac{\partial w}{\partial t} = 0$ this can be simplified to

$$[(w,u)_{\Omega^{n+1}} - (w,u)_{\Omega^n}] + \left[\left(w, \frac{u^2}{2}\right)_{P^+} - \left(w, \frac{u^2}{2}\right)_{P^-}\right] - \left(\frac{\partial w}{\partial x}, \frac{u^2}{2}\right)_Q = (w,f)_Q. \tag{5.5}$$

To keep things simple we will restrict ourselves to the implicit Euler discretization. Although this is not a very efficient time march method, its simple form allows us to examine the interpretation of semi-discrete methods with relative clarity. So the goal is to rewrite (5.1) in the form of (5.6) plus possible extra terms such that it is still equivalent to the original equation formulated in space-time. For (5.1) this results in

$$\left(w, \frac{u^{n+1} - u^n}{\Delta t}\right)_\Omega + \left(w, \frac{1}{2}\frac{\partial \left(u^{n+1}\right)^2}{\partial x}\right)_{\Omega^{n+1}} = (w,f)_{\Omega^{n+1}} \tag{5.6}$$

note here that for the first term the assumption was made that integration over Ω^n is the same as integration over Ω^{n+1} ($\Omega^n = \Omega^{n+1} = \Omega$) in other words, it is assumed that the time boundaries of the domain do not change. Thus the first term of (5.6) is written as an integration over Ω, and similarly the first term of (5.5): $[(w,u)_{\Omega^{n+1}} - (w,u)_{\Omega^n}]$ can be written as $\left(w, u^{n+1} - u^n\right)_\Omega$. So (5.5) now looks like this:

$$\left(w, u^{n+1} - u^n\right)_\Omega + \left[\left(w, \frac{u^2}{2}\right)_{P+} - \left(w, \frac{u^2}{2}\right)_{P-}\right] - \left(\frac{\partial w}{\partial x}, \frac{u^2}{2}\right)_Q = (w, f)_Q. \tag{5.7}$$

Now divide both sides by Δt:

$$\left(w, \frac{u^{n+1} - u^n}{\Delta t}\right)_\Omega + \frac{1}{\Delta t}\left[\left(w, \frac{u^2}{2}\right)_{P+} - \left(w, \frac{u^2}{2}\right)_{P-}\right] - \frac{1}{\Delta t}\left(\frac{\partial w}{\partial x}, \frac{u^2}{2}\right)_Q = \frac{1}{\Delta t}(w, f)_Q, \tag{5.8}$$

then add and subtract $\left(w, 1/2\frac{\partial (u^{n+1})^2}{\partial x}\right)_{\Omega^{n+1}}$:

$$\begin{aligned}\left(w, \frac{u^{n+1} - u^n}{\Delta t}\right)_\Omega + \frac{1}{\Delta t}\left[\left(w, \frac{u^2}{2}\right)_{P+} - \left(w, \frac{u^2}{2}\right)_{P-}\right] - \frac{1}{\Delta t}\left(\frac{\partial w}{\partial x}, \frac{u^2}{2}\right)_Q \\ + \left(w, \frac{1}{2}\frac{\partial (u^{n+1})^2}{\partial x}\right)_{\Omega^{n+1}} - \left(w, \frac{1}{2}\frac{\partial (u^{n+1})^2}{\partial x}\right)_{\Omega^{n+1}} = \frac{1}{\Delta t}(w, f)_Q.\end{aligned} \tag{5.9}$$

Now do the same trick with $(w, f)_{\Omega^{n+1}}$ on the right-hand side

$$\begin{aligned}\left(w, \frac{u^{n+1} - u^n}{\Delta t}\right)_\Omega + \frac{1}{\Delta t}\left[\left(w, \frac{u^2}{2}\right)_{P+} - \left(w, \frac{u^2}{2}\right)_{P-}\right] - \frac{1}{\Delta t}\left(\frac{\partial w}{\partial x}, \frac{u^2}{2}\right)_Q \\ + \left(w, \frac{1}{2}\frac{\partial (u^{n+1})^2}{\partial x}\right)_{\Omega^{n+1}} - \left(w, \frac{1}{2}\frac{\partial (u^{n+1})^2}{\partial x}\right)_{\Omega^{n+1}} \\ = \frac{1}{\Delta t}(w, f)_Q + (w, f)_{\Omega^{n+1}} - (w, f)_{\Omega^{n+1}}.\end{aligned} \tag{5.10}$$

After rearranging the terms, the result is an equation that is still equivalent to (5.7) but in the form of the implicit Euler discretization (5.6). This differs from a standard Galerkin discretization by the terms in the square brackets:

$$\begin{aligned}&\left(w, \frac{u^{n+1} - u^n}{\Delta t}\right)_\Omega + \left(w, \frac{1}{2}\frac{\partial (u^{n+1})^2}{\partial x}\right)_{\Omega^{n+1}} \\ &+ \left[\frac{1}{\Delta t}\left(\left(w, \frac{u^2}{2}\right)_{P+} - \left(w, \frac{u^2}{2}\right)_{P-}\right) - \frac{1}{\Delta t}\left(\frac{\partial w}{\partial x}, \frac{u^2}{2}\right)_Q - \left(w, \frac{1}{2}\frac{\partial (u^{n+1})^2}{\partial x}\right)_{\Omega^{n+1}}\right. \\ &\left. - \frac{1}{\Delta t}(w, f)_Q + (w, f)_{\Omega^{n+1}}\right] \\ &= (w, f)_{\Omega^{n+1}}.\end{aligned} \tag{5.11}$$

As described in Chapter 2, the variational multiscale method can be used write (5.11) out as a large-scale and a small-scale equation. The large-scale equation of (5.11) is then

$$\begin{aligned}
&\left(\bar{w}, \frac{\bar{u}^{n+1}-\bar{u}^{n}}{\Delta t}\right)_{\Omega} + \left(\bar{w}, \frac{1}{2}\frac{\partial(\bar{u}^{n+1})^2}{\partial x}\right)_{\Omega} \\
&+\Bigg[\left(\bar{w}, \frac{u'^{n+1}-u'^{n}}{\Delta t}\right)_{\Omega} - \left(\bar{w}, \frac{1}{2}\frac{\partial(\bar{u}^{n+1})^2 + 2\bar{u}^{n+1}u'^{n+1} + (u'^{n}+1)^2}{\partial x}\right)_{\Omega} \\
&\quad + \left(w, \frac{1}{2}\frac{\partial\left(2\bar{u}^{n+1}u'^{n+1} + (u'^{n+1})^2\right)}{\partial x}\right)_{\Omega^{n+1}} + \frac{1}{\Delta t}\left(\left(\bar{w}, \frac{u^2}{2}\right)_{P^+} - \left(\bar{w}, \frac{u^2}{2}\right)_{P^-}\right) \\
&\quad - \frac{1}{\Delta t}\left(\bar{w}_x, \frac{u^2}{2}\right)_{Q} - \frac{1}{\Delta t}(\bar{w}, f)_{Q} + (\bar{w}, f)_{\Omega^{n+1}}\Bigg] = (\bar{w}, f)_{\Omega^{n+1}}
\end{aligned} \tag{5.12}$$

which can be rewritten as

$$\begin{aligned}
&\left(\bar{w}, \frac{\bar{u}^{n+1}-\bar{u}^{n}}{\Delta t}\right)_{\Omega} + \left(\bar{w}, \frac{1}{2}\frac{\partial(\bar{u}^{n+1})^2}{\partial x}\right)_{\Omega} \\
&+\Bigg[\left(\bar{w}, \frac{u'^{n+1}-u'^{n}}{\Delta t}\right)_{\Omega} - \left(\bar{w}, \frac{1}{2}\frac{\partial(\bar{u}^{n+1})^2}{\partial x}\right)_{\Omega} + \frac{1}{\Delta t}\left(\left(\bar{w}, \frac{u^2}{2}\right)_{P^+} - \left(\bar{w}, \frac{u^2}{2}\right)_{P^-}\right) \\
&\quad - \frac{1}{\Delta t}\left(\bar{w}_x, \frac{u^2}{2}\right)_{Q} - \frac{1}{\Delta t}(\bar{w}, f)_{Q} + (\bar{w}, f)_{\Omega^{n+1}}\Bigg] = (\bar{w}, f)_{\Omega^{n+1}}.
\end{aligned} \tag{5.13}$$

For the remainder of this chapter the forcing f will be assumed to be zero, in that case (5.13) becomes:

$$\begin{aligned}
&\left(\bar{w}, \frac{\bar{u}^{n+1}-\bar{n}^{n}}{\Delta t}\right)_{\Omega} + \left(\bar{w}, \frac{1}{2}\frac{\partial(\bar{u}^{n+1})^2}{\partial x}\right)_{\Omega} \\
&+\Bigg[\left(\bar{w}, \frac{u'^{n+1}-u'^{n}}{\Delta t}\right)_{\Omega} - \left(\bar{w}, \frac{1}{2}\frac{\partial(\bar{u}^{n+1})^2}{\partial x}\right)_{\Omega} + \frac{1}{\Delta t}\left(\left(\bar{w}, \frac{u^2}{2}\right)_{P^+} - \left(\bar{w}, \frac{u^2}{2}\right)_{P^-}\right) \\
&\quad - \frac{1}{\Delta t}\left(\bar{w}_x, \frac{u^2}{2}\right)_{Q}\Bigg] = 0.
\end{aligned} \tag{5.14}$$

The term within the square brackets in (5.13) is what one needs to add to the implicit Euler discretization to have a nodally exact large-scale solution $\bar{u}$. A good shock-capturing operator will approximate the behaviour of this term. For $f = 0$, a term S_{sc} is defined as follows:

$$\begin{aligned}
S_{sc} = &\Bigg[\left(\bar{w}, \frac{u'^{n+1}-u'^{n}}{\Delta t}\right)_{\Omega} - \left(\bar{w}, \frac{1}{2}\frac{\partial(\bar{u}^{n+1})^2}{\partial x}\right)_{\Omega} + \frac{1}{\Delta t}\left(\left(\bar{w}, \frac{u^2}{2}\right)_{P^+} - \left(\bar{w}, \frac{u^2}{2}\right)_{P^-}\right) \\
&- \frac{1}{\Delta t}\left(\bar{w}_x, \frac{u^2}{2}\right)_{Q}\Bigg]
\end{aligned} \tag{5.15}$$

With the exact solution (in green in Fig. 5.6 and Fig. 5.7) and the required large-scale solution (defined in red in Fig. 5.6 and Fig. 5.7) known, the small-scale solution is then

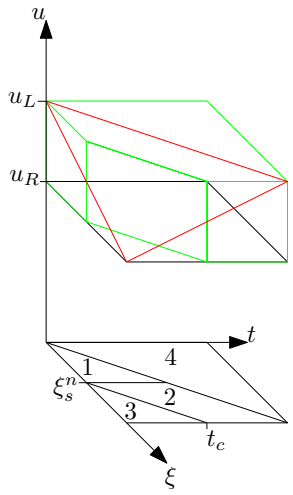

1:	$0 \leq \xi \leq \xi_s^n$	$u = u_L$
	$0 \leq t \leq \frac{\Delta t}{h}\xi$	$\bar{u}(\xi,t) = \frac{u_R-u_L}{h}\xi - \frac{u_R-u_L}{\Delta t}t + u_L$
		$u'(\xi,t) = -\frac{u_R-u_L}{h}\xi + \frac{u_R-u_L}{\Delta t}t$
2:	$\xi_s^n < \xi \leq h$	$u = u_L$
	$\frac{2}{u_L+u_R}(\xi-\xi_s^n) \leq t \leq \frac{\Delta t}{h}\xi$	$\bar{u}(\xi,t) = \frac{u_R-u_L}{h}\xi - \frac{u_R-u_L}{\Delta t}t + u_L$
		$u'(\xi,t) = -\frac{u_R-u_L}{h}\xi + \frac{u_R-u_L}{\Delta t}t$
3:	$\xi_s^n < \xi \leq h$	$u = u_R$
	$0 \leq t \leq \frac{2}{u_L+u_R}(\xi-\xi_s^n)$	$\bar{u}(\xi,t) = \frac{u_R-u_L}{h}\xi - \frac{u_R-u_L}{\Delta t}t + u_L$
		$u'(\xi,t) = (u_R-u_L)\left(1 - \frac{\xi}{h} + \frac{t}{\Delta t}\right)$
4:	$0 \leq \xi \leq h$	$u = u_L$
	$\frac{\Delta t}{h}\xi < t \leq \Delta t$	$\bar{u} = u_L$
		$u' = 0$

Figure 5.6: The exact (green) and large-scale solution (red) on element 1 and the subdivision of Q_1 with the exact from of u, $\bar{u}$ and u' on each subdomain.

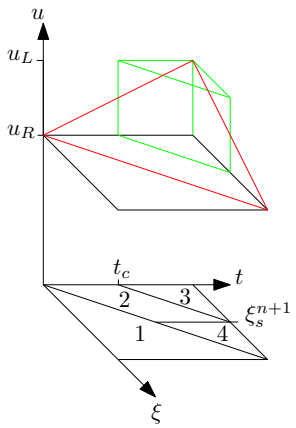

1:	$0 \leq \xi \leq h$	$u = u_R$
	$0 \leq t \leq \frac{\Delta t}{h}\xi$	$\bar{u} = u_R$
		$u' = 0$
2:	$0 \leq \xi \leq \xi_s^{n+1}$	$u = u_R$
	$\frac{\Delta t}{h}\xi < t \leq \frac{2}{u_L+u_R}(\xi-\xi_s^{n+1}) + \Delta t$	$\bar{u}(\xi,t) = \frac{u_R-u_L}{h}\xi - \frac{u_R-u_L}{\Delta t}t + u_R$
		$u'(\xi,t) = -\frac{u_R-u_L}{h}\xi + \frac{u_R-u_L}{\Delta t}t$
3:	$0 \leq \xi \leq \xi_s^{n+1}$	$u = u_L$
	$\frac{2}{u_L+u_R}(\xi-\xi_s^{n+1}) + \Delta t < t \leq \Delta t$	$\bar{u}(\xi,t) = \frac{u_R-u_L}{h}\xi - \frac{u_R-u_L}{\Delta t}t + u_R$
		$u'(\xi,t) = (u_R-u_L)\left(\frac{t}{\Delta t} - \frac{\xi}{h} - 1\right)$
4:	$\xi_s^{n+1} < \xi \leq h$	$u = u_R$
	$\frac{\Delta t}{h}\xi < t \leq \Delta t$	$\bar{u}(\xi,t) = \frac{u_R-u_L}{h}\xi - \frac{u_R-u_L}{\Delta t}t + u_R$
		$u'(\xi,t) = -\frac{u_R-u_L}{h}\xi + \frac{u_R-u_L}{\Delta t}t$

Figure 5.7: The exact (green) and large-scale solution (red) on element 2 and the subdivision of Q_2 with the exact from of u, $\bar{u}$ and u' on each subdomain.

obtained by subtracting the large-scale solution from the exact solution ($u' = u - \bar{u}$). Now that u, $\bar{u}$, and u' are known, the terms from (5.15) can be computed exactly. The path of the shock in space-time, going from element 1 to element 2, can be parametrised in terms of t and ξ_1 or ξ_2. For simplicity we consider ξ_1 and ξ_2 being equivalent to the physical x-coordinates on elements 1 and 2 respectively, each equal to zero at the start of the element. So $\xi_1 = x - x_{e_1}$ where x_{e_1} is the x coordinate of the left-hand boundary of element 1 as depicted in Fig. 5.8. Note that although the first two terms in (5.14) require integration over

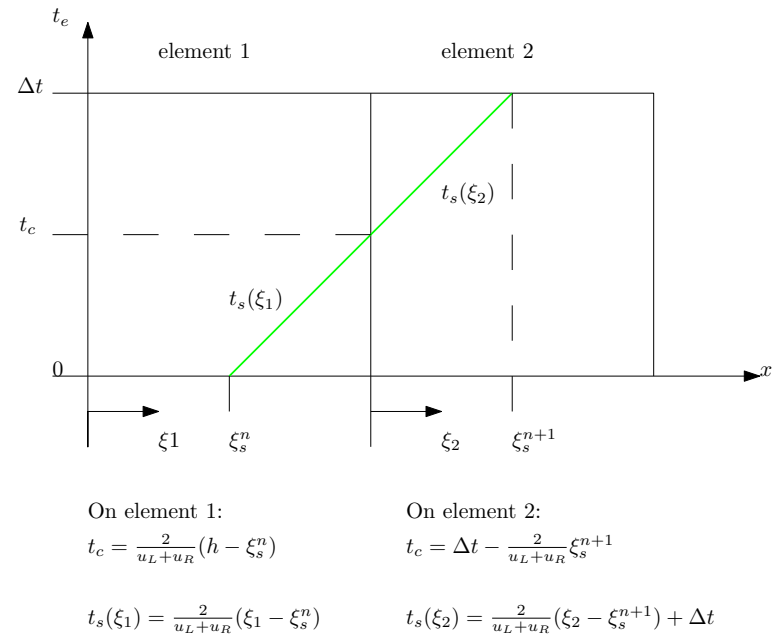

Figure 5.8: Parametrisation of the shock line $t_s(\xi)$ in elements e_1 and e_2.

Ω (so in the x direction) as is usual for a discrete-in-time implicit Euler formulation, within the square brackets there are still some time integrations to be done for the terms on Q and P. The parametrization shown in Fig. 5.8 will be used to compute these integrals in the next section.

5.2.1 Semi-discrete formulation on element 1

With the inner products from 5.15 written out in integrals, the term S_{sc} can be written as

$$\begin{aligned} S_{sc} = &\int_0^h \bar{w}\frac{u'^{n+1} - u'^n}{\Delta t}d\xi - \int_0^h \bar{w}\frac{1}{2}\frac{\partial(\bar{u}^{n+1})^2}{\partial x}d\xi + \frac{1}{\Delta t}\int_0^{\Delta t}\bar{w}(h)\frac{u(h)^2}{2}dt \\ &- \frac{1}{\Delta t}\int_0^{\Delta t}\bar{w}(0)\frac{u(0)^2}{2}dt - \frac{1}{\Delta t}\int_0^{\Delta t}\int_0^h \frac{\partial \bar{w}}{\partial x}\frac{u^2}{2}d\xi dt \end{aligned} \tag{5.16}$$

To compute this term, the integrals over the domain will be split up as indicated in Fig. 5.6: element 1 is divided into four sub-domains where u, $\bar{u}$ or u' are defined differently. Applying

u, $\bar{u}$ and u' as given in Fig. 5.6, S_{sc} for this element becomes:

$$\begin{aligned}
S_{sc} &= \frac{u_R - u_L}{\Delta t}\left(\int_0^h \bar{w}\frac{\xi}{h}d\xi - \int_{\xi_s^n}^h \bar{w}d\xi\right) + \int_0^{t_c} \bar{w}\frac{1}{\Delta t}\frac{u_R^2}{2}dt + \int_{t_c}^{\Delta t} \bar{w}\frac{1}{\Delta t}\frac{u_L^2}{2}dt - \bar{w}(0)\frac{u_L^2}{2} \\
&- \frac{1}{\Delta t}\left(\int_0^{\xi_s^n}\int_0^{\Delta t}\frac{\partial \bar{w}}{\partial x}\frac{u_L^2}{2}dtd\xi + \int_{\xi_n^2}^h\left[\int_0^{t_s}\frac{\partial \bar{w}}{\partial x}\frac{u_R^2}{2}dt + \int_{t_s}^{\Delta t}\frac{\partial \bar{w}}{\partial x}\frac{u_L^2}{2}dt\right]d\xi\right) \\
&= \frac{u_R - u_L}{\Delta t}\left(\int_0^h \bar{w}\frac{\xi}{h}d\xi - \int_{\xi_s^n}^h \bar{w}d\xi\right) + \frac{\bar{w}(h)}{\Delta t}\frac{u_R^2}{2}\frac{w}{u_L + u_R}(h - \xi_s^n) \\
&+ \frac{\bar{w}(h)}{\Delta t}\frac{u_L^2}{2}\left(\Delta t - \frac{2}{u_L + u_R}(h - \xi_s^n)\right) - \bar{w}(0)\frac{u_L^2}{2} \\
&- \frac{1}{\Delta t}\left[\int_0^{\xi_s^n}\frac{\partial \bar{w}}{\partial x}\frac{u_L^2}{2}\Delta t d\xi + \int_{\xi_s^n}^h \frac{\partial \bar{w}}{\partial x}\left(\frac{u_R^2}{2}\frac{2}{u_L + u_R}(\xi - \xi_s^n) + \frac{u_L^2}{2}\left(\Delta t - \frac{2}{u_L + u_R}(\xi - \xi_s^n)\right)\right)d\xi\right]
\end{aligned} \tag{5.17}$$

Which, when worked out, results in

$$S_{sc}^{e_1} = \int_0^h \bar{w}\frac{u_R - u_L}{\Delta t}\frac{\xi}{h}d\xi = \left(\bar{w}, \frac{u_R - u_L}{\Delta t}\frac{\xi}{h}\right)_{\Omega_1} \tag{5.18}$$

So for element 1 the entire term in the square brackets in (5.15) reduces to just (5.18). And the semi-discrete formulation for this element becomes

$$\left(\bar{w}, \frac{\bar{u}^{n+1} - \bar{u}^n}{\Delta t}\right)_\Omega + \left(\bar{w}, \frac{1}{2}\frac{\partial (u^{n+1})^2}{\partial x}\right)_\Omega + S_{sc}^{e_1} = 0. \tag{5.19}$$

The large-scale residual is defined as

$$\bar{R} = \frac{\bar{u}^{n+1} - \bar{u}^n}{\Delta t} + \frac{1}{2}\frac{\partial (\bar{u}^{n+1})^2}{\partial x} \tag{5.20}$$

and on element 1, substituting $\bar{u}^{n+1}$ and $\bar{u}^n$ this becomes

$$\bar{R}_{e_1} = -\frac{u_R - u_L}{\Delta t}\frac{\xi}{h}. \tag{5.21}$$

Note the similarity between 5.18 and 5.21, 5.18 can also be written as

$$S_{sc}^{e_1} = \int_0^h \bar{w}(-\bar{R}_{e_1})d\xi = \left(\bar{w}, -\bar{R}_{e_1}\right). \tag{5.22}$$

5.2.2 Semi-discrete formulation on element 2

The same can be done for element 2, using the division of Q_2 as given in Fig. 5.7 and applying the u, $\bar{u}$ and u' as indicated, the term S_{sc} then becomes

$$\begin{aligned}
S_{sc}^{e_2} &= \int_0^h \bar{w}\frac{u'^{n+1}-u'^{n}}{\Delta t}d\xi - \int_0^h \bar{w}\frac{1}{2}\frac{\partial(\bar{u}^{n+1})^2}{\partial x}d\xi + \frac{1}{\Delta t}\int_0^{\Delta t}\bar{w}(h)\frac{u(h)^2}{2}dt \\
&- \frac{1}{\Delta t}\int_0^{\Delta t}\bar{w}(0)\frac{u(0)^2}{2}dt - \frac{1}{\Delta t}\int_0^{\Delta t}\int_0^h \frac{\partial \bar{w}}{\partial x}\frac{u^2}{2}d\xi dt \\
&= \int_0^{\xi_s^{n+1}} \bar{w}\frac{1}{\Delta t}\left(\frac{-(u_R-u_L)}{h}\xi - 0\right)d\xi + \int_{\xi_s^{n+1}}^h \bar{w}\frac{(u_R-u_L)\left(1-\frac{\xi}{h}\right)-0}{\Delta t}d\xi \\
&- \int_0^h \bar{w}\frac{1}{2}\frac{\partial}{\partial x}\left(u_L + \frac{u_R-u_L}{h}\xi\right)^2 d\xi + \frac{1}{\Delta t}\int_0^{\Delta t}\bar{w}(h)\frac{u_R^2}{2}dt \\
&- \frac{1}{\Delta t}\int_0^{t_c}\bar{w}(0)\frac{u_R^2}{2}dt - \frac{1}{\Delta t}\int_{t_c}^{\Delta t}\bar{w}(0)\frac{u_L^2}{2}dt \\
&- \frac{1}{\Delta t}\int_0^{\xi_s^{n+1}}\frac{\partial \bar{w}}{\partial x}\left(\int_0^{t_s}\frac{u_R^2}{2}dt + \int_{t_s}^{\Delta t}\frac{u_L^2}{2}dt\right)d\xi - \frac{1}{\Delta t}\int_{\xi_s^{n+1}}^h\int_0^{\Delta t}\frac{\partial \bar{w}}{\partial x}\frac{u_R^2}{2}dtd\xi
\end{aligned} \tag{5.23}$$

When worked out further, this reduces to:

$$\begin{aligned}
S_{sc}^{e_2} &= \int_0^h \bar{w}\left[\frac{u_R-u_L}{\Delta t}\left(1-\frac{\xi_2}{h}\right) - \frac{u_R-u_L}{h}\left(u_L + \frac{u_R-u_L}{h}\xi_2\right)\right]d\xi_2 \\
&= \left(\bar{w}, \frac{u_R-u_L}{\Delta t}\left(1-\frac{\xi_2}{h}\right) - \frac{u_R-u_L}{h}\left(u_L + \frac{u_R-u_L}{h}\xi_2\right)\right)_{\Omega_2}
\end{aligned} \tag{5.24}$$

This means that for element 2 the semi-discrete formulation is

$$\left(\bar{w}, \frac{\bar{u}^{n+1}-\bar{u}^n}{\Delta t}\right)_\Omega + \left(\bar{w}, \frac{1}{2}\frac{\partial(u^{n+1})^2}{\partial x}\right)_\Omega + S_{sc}^{e_2} = 0. \tag{5.25}$$

The large-scale residual as given in (5.20) for this element is

$$\bar{R}_{e_2} = -\frac{u_R-u_L}{\Delta t}\left(1-\frac{\xi_2}{h}\right) + \frac{u_R-u_L}{h}\left(u_L + \frac{u_R-u_L}{h}\xi_2\right), \tag{5.26}$$

and so $S_{sc}^{e_2}$ can also be written as

$$S_{sc}^{e_2} = \int_0^h \bar{w}(-\bar{R}_{e_2})d\xi = \left(\bar{w}, -\bar{R}_{e_2}\right). \tag{5.27}$$

5.2.3 Result: shock moving from one element to its neighbour

In Fig. 5.9 the effect of the shock-capturing terms derived above is demonstrated. The domain $[0,1]$ is divided into four elements and the initial solution is $u_L = 2$, $u_R = 1$ and the shock-position at $t = 0$ is $x_s = 0.4$. With a time-step size $\Delta t = 2/15$ and the shock moving with

$u_s = (u_L+u_R)/2 = 1.5$, the shock position after one time step will be $x_s(t = \Delta t) = 0.6$, which is in the next element. The nodally exact large-scale solution is plotted together with the computed solution. It is clear from Fig 5.9 that adding the S_{sc} terms, as derived in sections

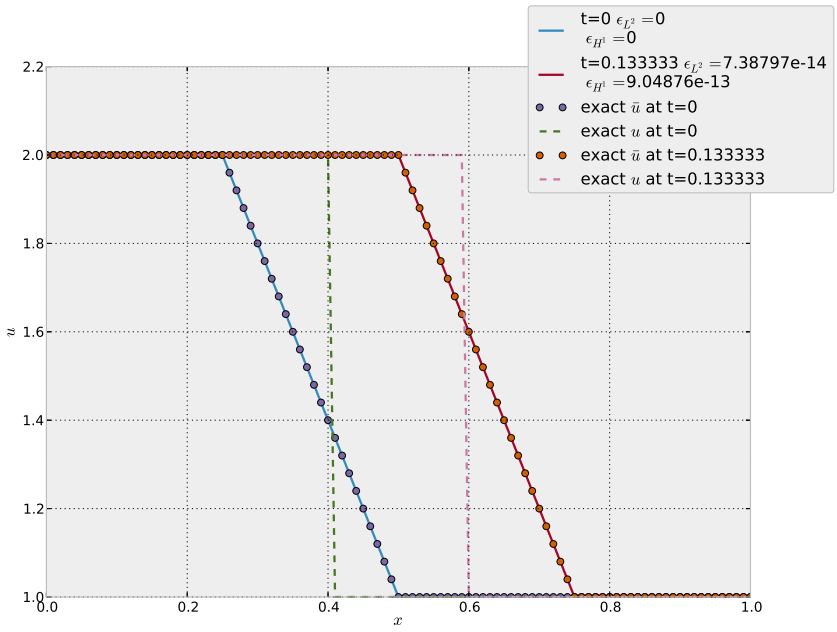

Figure 5.9: $x_s = 0.4$ 4 elements, $\Delta t = 2/15$, one time-step Implicit Euler time march.

5.2.1 and 5.2.2, to the problem formulation produces the nodally exact large-scale solution. This is also clear from the L^2 and the H^1 error of the computed solution (the convergence tolerance for the corrector passes in the Newton iteration in this computation was 10^{-6}).

5.3 Shock moving across multiple elements

In the previous section the focus was on the case where the shock moves from one element to its neighbour. Now the case where the shock moves faster, and crosses multiple elements in one time-step will be considered. The situation of a shock moving at a constant speed across k elements is shown in Fig. 5.10. The situation for the first and last elements is exactly the same as for element 1 and 2 from the previous section, only the value of t_c, the time at which the shock crosses the element boundary, will be different. However the analytic expression is still the same. Thus the S_{sc} term for the first and last element will be the same the ones derived in the previous section. All elements between the first and k^{th} element can all be characterised in the same way; this is shown in Fig 5.11. The S_{sc} term for the i^{th} element

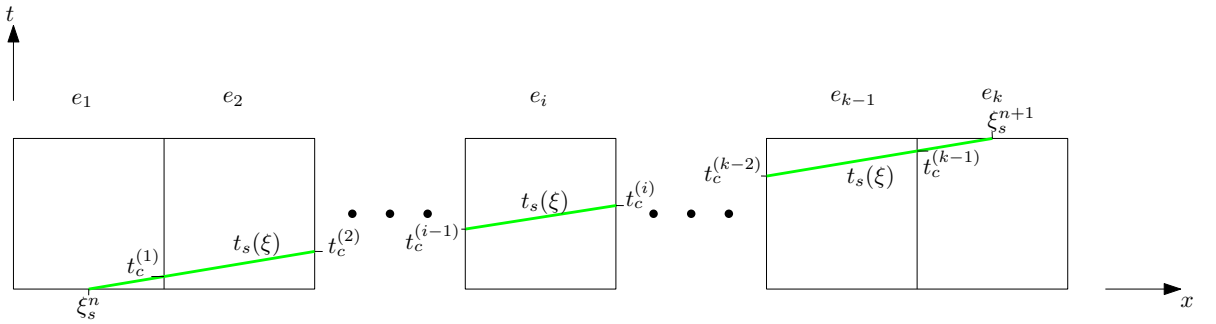

Figure 5.10: Shock moving through multiple elements in space-time.

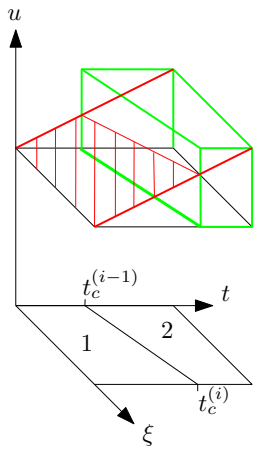

1: $0 \le \xi \le h$, $0 \le t \le \frac{2}{u_L+u_R}(\xi - \xi_s^n + (i-1)h)$: $u = u_R$, $\bar{u} = u_R - \frac{u_R-u_L}{\Delta t}t$, $u' = \frac{u_R-u_L}{\Delta t}t$

2: $0 \le \xi \le h$, $\frac{2}{u_L+u_R}(\xi - \xi_s^n + (i-1)h) < t \le \Delta t$: $u = u_L$, $\bar{u} = u_R - \frac{u_R-u_L}{\Delta t}t$, $u' = (u_R - u_L)\left(\frac{t}{\Delta t} - 1\right)$

Figure 5.11: The exact (green) and the large-scale (red) solution on element e_i.

can be derived by substituting u, $\bar{u}$ and u' as given by Fig. 5.11 into the expression for S_{sc}:

$$\begin{aligned}S_{sc} = &\int_0^h \bar{w}\frac{u'^{n+1} - u'^n}{\Delta t}d\xi - \int_0^h \bar{w}\frac{1}{2}\frac{\partial(\bar{u}^{n+1})^2}{\partial x}d\xi + \frac{1}{\Delta t}\int_0^{\Delta t}\bar{w}(h)\frac{u(h)^2}{2}dt \\ &- \frac{1}{\Delta t}\int_0^{\Delta t}\bar{w}(0)\frac{u(0)^2}{2}dt - \frac{1}{\Delta t}\int_0^{\Delta t}\int_0^h \frac{\partial \bar{w}}{\partial x}\frac{u^2}{2}d\xi dt,\end{aligned}$$

resulting in

$$\begin{aligned}S_{sc}^{e_i} = &\frac{1}{\Delta t}\int_0^{t_c^{(i)}}\bar{w}(h)\frac{u(h)^2}{2}dt + \frac{1}{\Delta t}\int_{t_c^{(i)}}\bar{w}(h)\frac{u(h)^2}{2}dt - \frac{1}{\Delta t}\int_0^{t_c^{(i-1)}}\bar{w}(0)\frac{u(0)^2}{2}dt \\ &- \frac{1}{\Delta t}\int_{t_c^{(i-1)}}^{\Delta t}\bar{w}(0)\frac{u(0)^2}{2}dt - \frac{1}{\Delta t}\int_0^h \frac{\partial \bar{w}}{\partial x}\left[\int_0^{t_s}\frac{u^2}{2}dt + \int_{t_s}^{\Delta t}\frac{u^2}{2}dt\right]d\xi \\ = &\frac{\bar{w}(h)}{\Delta t}\frac{u_R^2}{2}\frac{2}{u_L+u_R}(ih - \xi_s^n) + \frac{\bar{w}(h)}{\Delta t}\frac{u_L^2}{2}\left(\Delta t - \frac{2}{u_L+u_R}(ih-\xi_s^n)\right) \\ &- \frac{\bar{w}(0)}{\Delta t}\frac{u_R^2}{2}\frac{2}{u_L+u_R}((i-1)h - \xi_s^n) - \frac{\bar{w}(0)}{\Delta t}\frac{u_L^2}{2}\left(\Delta t - \frac{2}{u_L+u_R}(i-1)h - \xi_s^n\right) \\ &- \frac{1}{\Delta t}\int_0^h \frac{\partial \bar{w}}{\partial x}\left[\frac{u_R^2}{2}\frac{2}{u_L+u_R}(\xi - \xi_s^n + (i-1)h) + \frac{u_L^2}{2}(\Delta t - \frac{2}{u_L+u_R}(\xi - \xi_s^n + (i-1)h))\right]d\xi \\ = &\frac{\bar{w}(h)}{\Delta t}(u_R - u_L)(ih - \xi_s^n) + \bar{w}(h)\frac{u_L^2}{2} - \bar{w}(0)\frac{u_R - u_L}{\Delta t}((i-1)h - \xi_s^n) \\ &- \bar{w}(0)\frac{u_L^2}{2} - \frac{1}{\Delta t}\int_0^h \frac{\partial \bar{w}}{\partial x}\left[(u_R - u_L)(\xi - \xi_s^n + (i-1)h) + \frac{u_L^2\Delta t}{2}\right]d\xi,\end{aligned} \tag{5.28}$$

and when this is worked out, it yields

$$S_{sc}^{e_i} = \int_0^h \bar{w}\frac{u_R - u_L}{\Delta t}d\xi = \left(\bar{w}, \frac{u_R - u_L}{\Delta t}\right). \tag{5.29}$$

For this element, the large-scale residual is

$$\begin{aligned}\bar{R}_{e_i} &= \frac{\bar{u}^{n+1} - \bar{u}^n}{\Delta t} + \frac{1}{2}\frac{\partial(\bar{u}^{n+1})^2}{\partial x} \\ &= -\frac{u_R - u_L}{\Delta t},\end{aligned} \tag{5.30}$$

one can quickly see that, as in the previous case, the S_{sc} term can be written in terms of the residual:

$$S_{sc}^{e_i} = \int_0^h \bar{w}(-\bar{R}_{e_i})d\xi = \left(\bar{w}, -\bar{R}_{e_i}\right). \tag{5.31}$$

5.3.1 Result: shock moving across multiple elements

In Fig. 5.12 the result is shown for the case where, on a 6 element mesh, the shock moves from the second element to the fourth element. On element 2, the term (5.18) was used, on

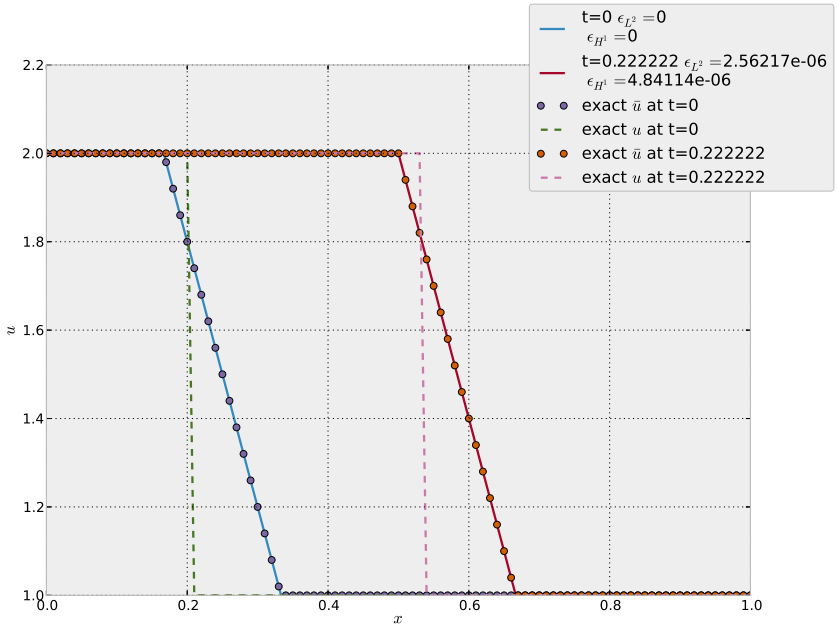

Figure 5.12: The shock moves from $x_s = 0.25$ to $x_s = 0.58$ on a 6 element grid. $\Delta t = 2/9$ and one Implicit Euler time step was taken.

element 3, the term (5.29) was used and on element 4 the term (5.24) was used. As can be observed from Fig. 5.12, the result is the exact large-scale solution. One can also make the shock move further in a single time-step, in that case the term (5.29) should be applied to all but the first and last shock elements.

5.4 Shock moving within one element

There is one situation that has not yet been mentioned: the shock that moves but does not leave the element. This situation is sketched in Fig. 5.13.

In this case the large-scale solution is constant in time and there are no discontinuities along the time borders of the element, so here it is easier to derive the S_{sc} term without the integration by parts applied before. Starting with the original large-scale equation in variational form:

$$\left(\bar{w}, \frac{\partial(\bar{u}+u')}{\partial t}\right)_Q + \left(\bar{w}, \frac{1}{2}\frac{\partial u^2}{\partial x}\right)_Q = 0, \tag{5.32}$$

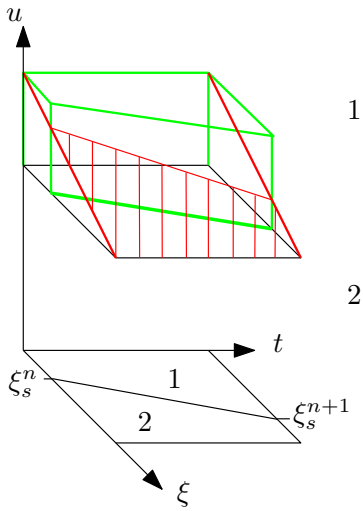

$$
\begin{aligned}
1:\quad & 0 \le t \le \Delta t && u = u_L \\
& 0 \le \xi \le \tfrac{\xi_s^{n+1}-\xi_s^n}{\Delta t} t + \xi_s^n && \bar{u} = u_L + \tfrac{u_R-u_L}{h}\xi \\
& && u' = -\tfrac{u_R-u_L}{h}\xi \\
2:\quad & 0 \le t \le \Delta t && u = u_R \\
& \tfrac{\xi_s^{n+1}-\xi_s^n}{\Delta t} t + \xi_s^n < \xi \le h && \bar{u} = u_L + \tfrac{u_R-u_L}{h}\xi \\
& && u' = (u_R - u_L)\left(1 - \tfrac{\xi}{h}\right)
\end{aligned}
$$

Figure 5.13: The exact (green) and the large-scale (red) solution when the shock moves but stays in one element.

now add and subtract $\left(\bar{w}, \frac{1}{2}\frac{\partial(\bar{u}^{n+1})^2}{\partial x}\right)_\Omega$ and rearrange terms:

$$
\begin{aligned}
&\underbrace{\left(\bar{w}, \frac{\partial(\bar{u})}{\partial t}\right)_Q}_{=0\ (\ \bar{u}\text{ is constant in time})} + \left(\bar{w}, \frac{1}{2}\frac{\partial(\bar{u}^{n+1})^2}{\partial x}\right)_\Omega \\
&\qquad + \underbrace{\left(\bar{w}, \frac{\partial u'}{\partial t}\right)_Q - \left(\bar{w}, \frac{1}{2}\frac{\partial(\bar{u}^{n+1})^2}{\partial x}\right)_\Omega + \left(\bar{w}, \frac{1}{2}\frac{\partial u^2}{\partial x}\right)_Q}_{S_{sc}} = 0.
\end{aligned}
\tag{5.33}
$$

By substituting the u, $\bar{u}$ and u' as given in Fig. 5.13, S_{sc} is computed:

$$
\begin{aligned}
S_{sc} &= \int_0^h \int_0^{\Delta t} \bar{w}\frac{\partial u'}{\partial t} dt d\xi - \int_0^h \bar{w}\frac{1}{2}\frac{\partial(\bar{u}^{n+1})^2}{\partial x} d\xi + \frac{1}{\Delta t}\int_0^{\Delta t}\int_0^h \bar{w}\frac{1}{2}\frac{\partial u^2}{\partial x} d\xi dt \\
&= -\int_0^h \bar{w}\left[u_L\frac{u_R-u_L}{h} + \frac{(u_R-u_L)^2}{h^2}\xi\right] d\xi.
\end{aligned}
\tag{5.34}
$$

And as before, a relation can be found between the S_{sc} term and the large-scale residual. The large-scale residual for the element under consideration is

$$
\begin{aligned}
\bar{R} &= \frac{\bar{u}^{n+1}-\bar{u}^n}{\Delta t} + \frac{1}{2}\frac{\partial(\bar{u}^{n+1})^2}{\partial x} \\
&= u_L\frac{u_R-u_L}{h} + \frac{(u_R-u_L)^2}{h^2}\xi.
\end{aligned}
\tag{5.35}
$$

This means that S_{sc}, expressed in terms of the large-scale residual, is:

$$
S_{sc} = \int_0^h \bar{w}(-\bar{R}) d\xi = \left(\bar{w}, -\bar{R}\right). \tag{5.36}
$$

5.4.1 Result: shock moving within one element

When the term (5.34) is used for the specific case of the shock moving but staying within the same element, then he result is the nodally exact large-scale solution. This is demonstrated in Fig 5.14.

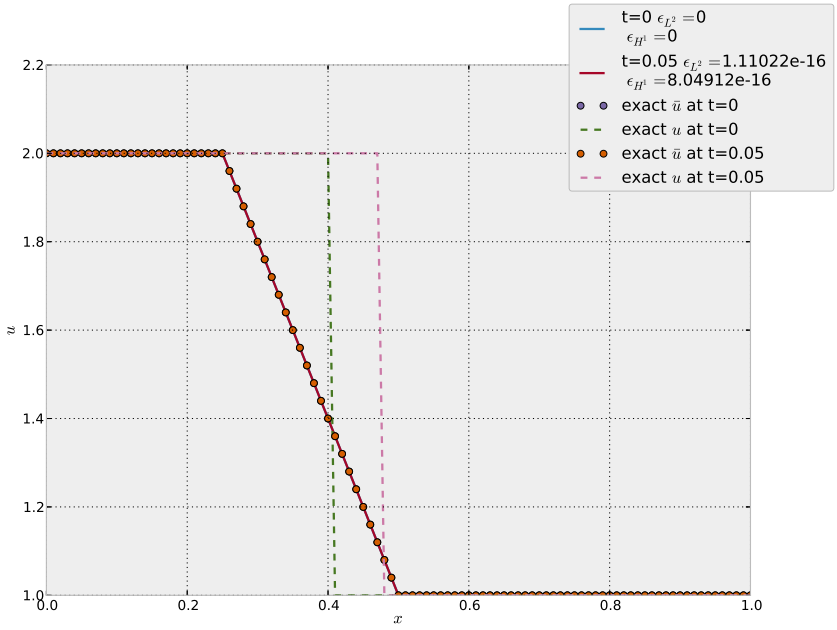

Figure 5.14: $x_s = 0.4$ 4 elements, $\Delta t = 0.05$, one time-step Implicit Euler time march. The shock stays within the element.

5.5 Dynamic Multiscale Shock-Capturing (DMSC)

To make all of the above useful, one needs to know when to apply which term and on what elements to use them. To be able to do that, knowledge about the position of the shock at time t^n, the position at t^{n+1} and the shock strength (i.e. the values for u_L and u_R) is required. The name coined here for a strategy that does that is *Dynamic Multiscale Shock-Capturing* (DMSC). The term *Dynamic* emphasises the fact that, in contrast to some existing shock capturing methods, time-dependent behaviour of the small scales was not neglected in the derivations. In the computations done in this chapter and the next, the initial shock location $x_s(t = 0)$ was given as well as the initial shock strength (u_L and u_R at $t = 0$). For subsequent time steps, the new shock location at time $n+1$ is computed by $x_s(t^{n+1}) = x_s^n + \frac{u_L(t^n)+u_R(t^n)}{2}\Delta t$ (note that $\frac{u_L+u_R}{2}$ is the shock speed). With $u_L(t^n)$ and $u_R(t^n)$ being the value of the solution in the middle of the element before and after the shock at time level t^n respectively.

In the next chapter this method will be used on a problem that is a little more challenging

than just a moving shock.

Chapter 6

A model shock-turbulence interaction problem

In the previous chapters the test case has been a stationary or moving Burgers' shock. In this chapter, upstream fluctuations will be added. This is a step towards shock-turbulence interactions. This case does not mimic the complete interaction, in that it is dominated by the effects of the fluctuations on the shock. It is still useful, however, for demonstrating the potential of improved representations of the unresolved scales.

6.1 Test case

The spatial domain of the computation is $[0, 1]$, a time-dependent Dirichlet boundary condition is imposed on the left-hand side and a non-reflecting boundary condition on the right hand side. The solution at $t = 0$ is given as

$$u(x, t = 0) = \begin{cases} u_L & \forall x \leq x_s \\ u_R & \forall x > x_s \end{cases} \tag{6.1}$$

with $u_L = 1$, $u_R = 0.5$ and $x_s = 0.2$. The Dirichlet boundary condition on the left-hand side (at $x = 0$) is given by

$$u(x = 0, t) = u_L + 0.1 \sin(2\pi t).$$

This is a simple sine wave centered at u_L with an amplitude of 0.1 and a period of 1 time unit. The simulation will be run for a duration of 6 time units.

The interaction of these fluctuations resulting from the time-varying left-hand boundary condition and the shock will cause the shock to increase in strength, and the mean shock speed will increase. For this specific problem, no spectral transfer through the shock will occur.

A good theoretical model explaining this process is given by Zank et al. (2002). This model confirms that we should expect that the *turbulent kinetic energy* of those fluctuations will cause an increased average shock strength and speed. To prevent the shock from running out of our domain, the frame of reference will be moving with the initial shock velocity $\dot{x} = u_s(t=0) = \frac{u_L+u_R}{2} = \frac{1+0.5}{2} = 0.75$. With the moving frame of reference, the boundary condition on the left-hand side becomes:

$$u(x=0,t) = u_L + 0.1\sin\left(2\pi\left(t + \frac{u\Delta t}{\dot{x}}\right)\right)$$

6.2 Results

$YZ\beta$, DCDD and DMSC results for a 32 element mesh are compared to the exact solution in Fig. 6.1 and 6.2. In addition to the shock-capturing methods indicated, Fig. 6.1 used SUPG stabilization whereas in Fig. 6.2 V-SGS stabilization was used. Note that for DMSC the stabilization was only applied to elements where the shock-capturing was not active; for the other shock-capturing the stabilization was active in the entire domain as this generally gave better results in this case.

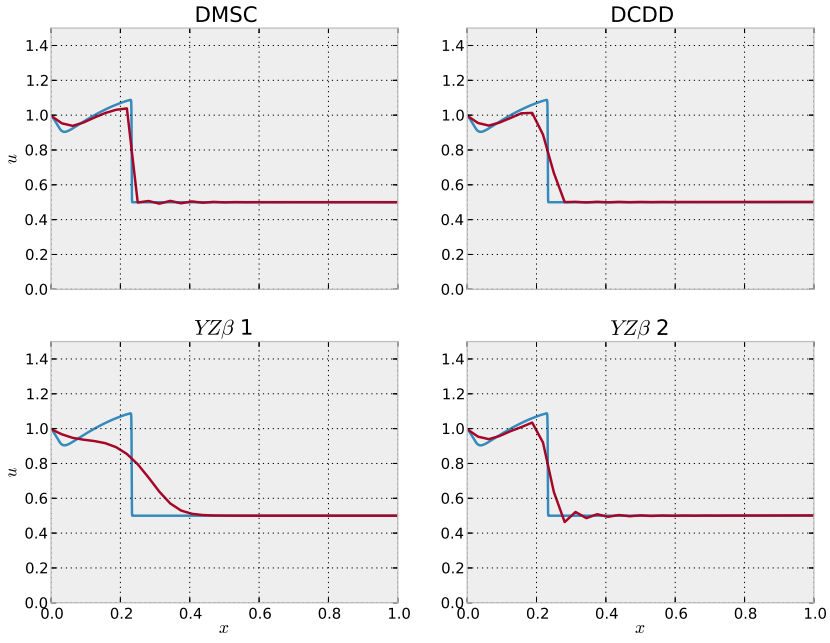

Figure 6.1: Comparison of different shock-capturing methods for the test case at $t = 6$ on a 32 element grid with the DNS solution plotted in blue. In all computations SUPG was used as well as the shock-capturing method mentioned above each plot.

In Chapter 4 it was observed that V-SGS stabilization is more dissipative than SUPG stabilization. One can see this effect here again by comparing Fig. 6.1 to Fig. 6.2. It is also very

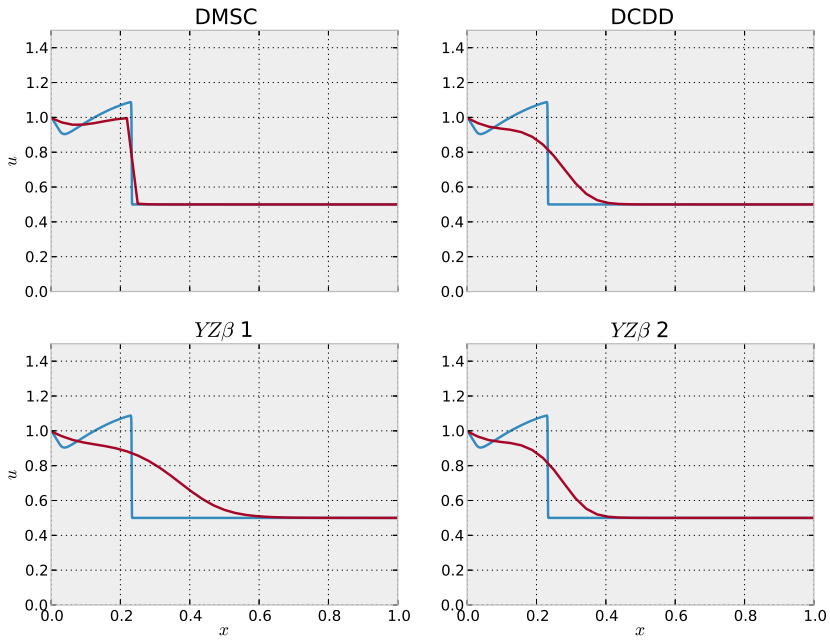

Figure 6.2: Comparison of different shock-capturing methods for the test case at $t = 6$ on a 32 element grid with the DNS solution plotted in blue. In all computations V-SGS was used as well as the shock-capturing method mentioned above each plot.

clear from the figures that DMSC outperforms the other methods. The next best performer seems to be $YZ\beta$ with $\beta = 2$, although in combination with V-SGS stabilization the shock is highly dissipated.

To quantify the performance of the different methods and probe their sensitivity to grid refinement, the errors of computations on a 32 ($h = 0.03125$) and a 64 ($h = 0.015625$) element grid are plotted in Fig. 6.3 for the SUPG stabilized case and Fig. 6.4 for the V-SGS stabilized case.

Just as in Chapter 4, the L^2 error is defined as

$$e_{L^2(\Omega)} = ||u - u^h||_{L^2(\Omega)} = \left(\int_\Omega (u - u^h)^2 d\Omega \right)^{\frac{1}{2}}. \tag{6.2}$$

A second error measurement is defined as the *nodal error*:

$$\epsilon_{nodal} = \sqrt{\sum_{i=1}^{n_e} (u(x_i) - \bar{u}(x_i))^2}, \tag{6.3}$$

where x_i is the x-coordinate of the i^{th} node of the mesh.

Another interesting metric is how the shock position is affected by the different methods. An overview of the shock location as a function of time is given in Fig. 6.5 for the SUPG

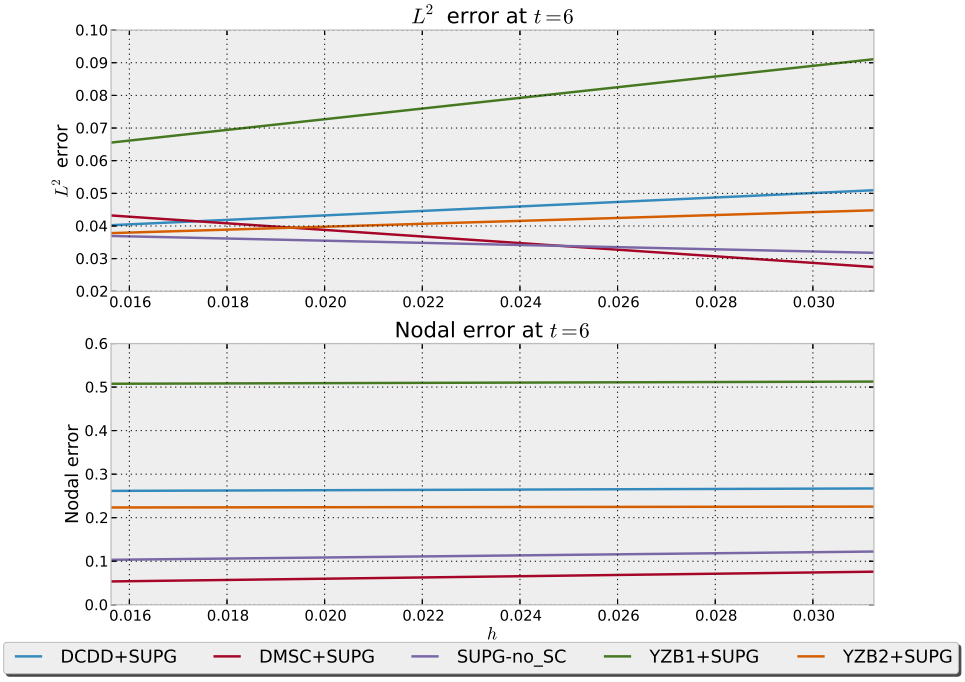

Figure 6.3: Overview of the L^2 and nodal error for SUPG stabilized computations with different shock-capturing methods. The plots show the errors at $t = 6$ with respect to the DNS.

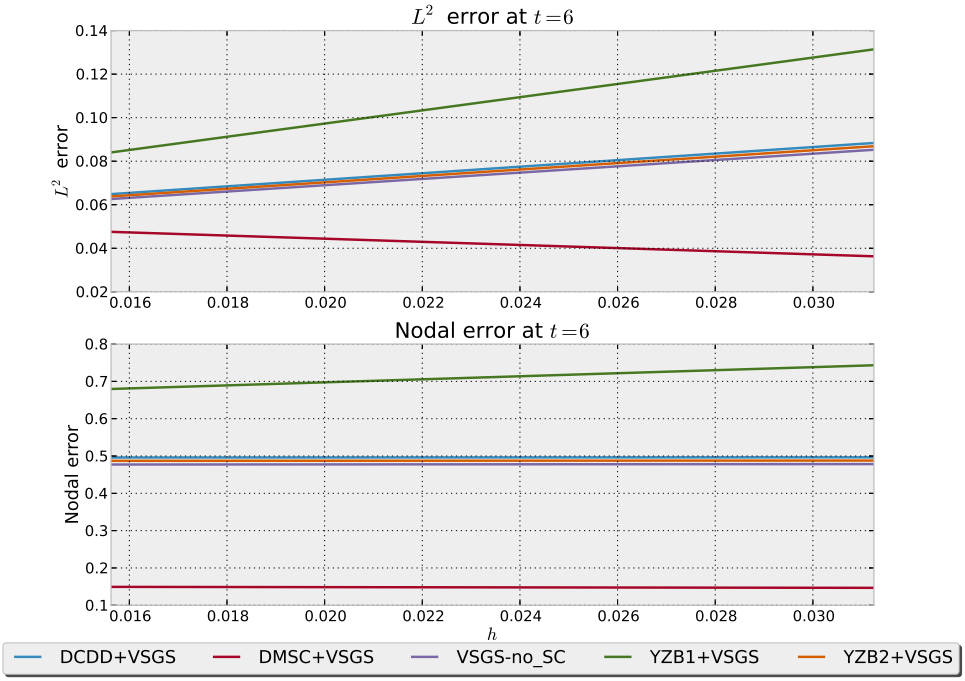

Figure 6.4: Overview of the L^2 and nodal error for V-SGS stabilized computations with different shock-capturing methods. The plots show the errors at $t = 6$ with respect to the DNS.

stabilized case and in Fig. 6.6 for the V-SGS stabilized case. The DMSC-line shows the shock location as a function of time during the computation. As in the previous chapter, for the DMSC, $\bar{x}_s$ indicates the location of the shock in the large-scale solution. The shock location is difficult to define for the shock-capturing methods that smear it out over several elements. Therefore the shock location was defined by the coordinates where the absolute value of the gradient was the greatest.

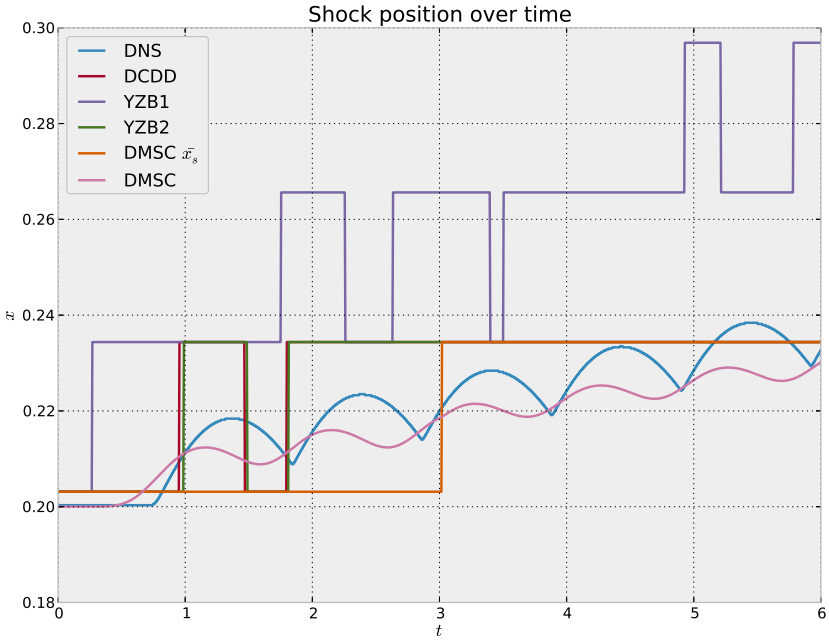

Figure 6.5: The shock position as it moves in time on a 32 element grid with SUPG stabilization and different shock-capturing mechanisms. Note that the shock position is indicated with respect to a moving frame of reference, moving with the speed $\dot{x} = 0.75$. The shock location was defined as the location where the absolute value of the gradient of the solution was largest.

It can be seen from Fig. 6.5 and Fig. 6.6 that the evolution of the shock location over time with DCDD or $YZ\beta$ shock-capturing is quite erratic. DMSC, however follows the mean behaviour of the exact (DNS) solution quite accurately.

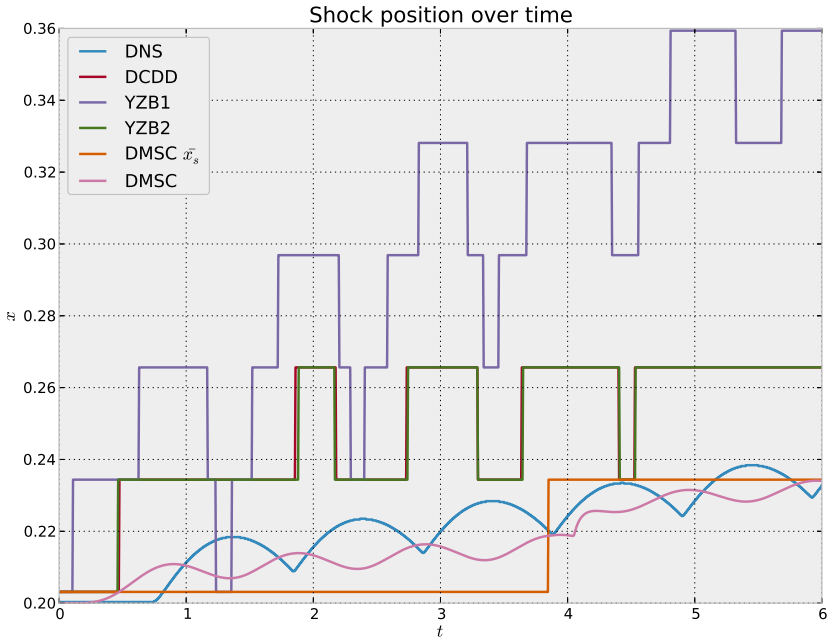

Figure 6.6: The shock position as it moves in time on a 32 element grid with V-SGS stabilization and different shock-capturing methods. Note that the shock position is indicated with respect to a moving frame of reference, moving with the speed $\dot{x} = 0.75$. The shock location was defined as the location where the absolute value of the gradient of the solution was largest.

Chapter 7

Conclusions

In this final chapter an overview is given of the results obtained. Conclusions are drawn and recommendations for improvements are given.

In Chapter 4 the small-scale term that influences the large-scale solution was derived for a stationary 1D Burgers' shock. It was shown that $YZ\beta$, with a certain value for β (depending on the specific problem), approximates this exact term in the integral sense. Specifically the $YZ\beta$ term, when integrated over the element containing a stationary shock, approximates the value of the exact term when integrated over that element. The $YZ\beta$ integrand however does not resemble the exact term. It is only their integrated values that are somewhat similar. In contrast, the *Discontinuity-Capturing Directional Dissipation*(DCDD) was too dissipative and was shown to be far off the mark when compared to the exact term. It can be concluded that the $YZ\beta$ term does, to some extent, behave as a multiscale approximation of the unresolved scales. The same cannot be said of the DCDD term.

For the stationary Burgers' shock, a residual based shock-capturing term was proposed: *Multiscale Shock-Capturing* (MSC). MSC was developed by starting out with a term inspired by $YZ\beta$:

$$\text{MSC term } = \left(\bar{w}_x, \underbrace{u_{ref}^{\alpha} \bar{u}_x^{\beta} h^{\gamma} R^{\delta}}_{S_{MSC}} \right),$$

where the exponents were constrained to make S_{MSC} dimensionally consistent. Then by varying the exponents, within the constraints, a formulation was found that replicates the small-scale term in the large-scale equation. MSC performed very well on the test problem, results were clearly better than those achieved by the existing $DCDD$ and $YZ\beta$ shock-capturing methods.

The MSC term can only be applied to problems for which the shock is stationary with respect to the mesh. We therefore also examined the requirements for representing the shock moving

relative to the mesh. An important finding of this work is that in order to achieve *nodally exact* shock-capturing, the dynamic behaviour of that small-scale term is essential. Simply applying MSC to a moving shock did not give good results as it does not take the time dependency of that small-scale term into account.

Therefore a *Dynamic Multiscale Shock-Capturing* (DMSC) technique was developed in Chapter 5. This was based on the derivation of the exact small-scale terms that appear in the large-scale equation. Which made it possible for DMSC to obtain nodally exact solutions to simple moving shocks. That the time dependency of the small scales is important has previously been stressed by Codina et al. (2007), yet the approach taken here to represent these small-scale terms exactly is quite different. A semi-discrete approach with Euler implicit time integration was used to demonstrate the viability of the approach in practice. Furthermore, when combined with SUPG or V-SGS stabilization over the part of the domain not containing the shock, the DMSC method performed very well for a more general shock-fluctuation interaction problem. Solutions were considerably better than those from existing shock-capturing operators.

This work clearly shows that the way forward is towards more fidelity in the unresolved scale models if one is looking for single element shock-capturing (only using $\bar{u}$ to determine a shock-capturing parameter will not suffice). Even when this unresolved scale model only takes onto account the shock itself, not even the interaction of the fluctuation with the shock, the results shown in Fig. 6.1, 6.2, 6.5 and 6.6 are significantly better than the existing shock-capturing methods used for comparison. By using advanced analytical models of interactions of shocks with turbulence, such as Wouchuk et al. (2009), it seems possible that high-fidelity unresolved scale models can be constructed for real shock-turbulence interactions.

7.1 Recommendations

The next step is to extend MSC and DMSC to multiple dimensions and to systems of multiple equations. MSC and DMSC can be used as an inspiration for methods applicable to the Euler and Navier-Stokes equations. Going from Burgers' equation to the Euler equations or the Navier-Stokes equations will certainly not be trivial and it will be more difficult to obtain exact expressions for small-scale terms which was already complicated for Burgers', but that is where the terms derived here can be used: as approximations to the exact small-scale terms in the Euler or Navier-Stokes equations when they cannot be obtained exactly.

MSC and DMSC are called shock-capturing methods as their formulation resembles a residual based shock-capturing term yet they are also different from regular shock-capturing methods in that they need to be actively switched on and off at the shock. Ideally a shock-capturing method automatically becomes active in the presence of shock and vanishes elsewhere. In that respect MSC and DMSC resemble shock-fitting methods. Making MSC and DMSC more generally applicable will require a shock-detection method to activate the shock-capturing terms. Shock-detection methods already exist, and it is recommended to research to what extent they can be used in combination with MSC and DMSC.

DMSC can be extended to more sophisticated time-march methods. In this thesis the implicit Euler time-march was used for DMSC because it was a very simple one. The performance of DMSC could be improved by using more advanced time-march methods.

Bibliography

K.E. Atkinson. *Theoretical numerical analysis: a functional analysis framework*, volume 39. Springer, 2009.

Y. Bazilevs, V.M. Calo, T.E. Tezduyar, and T.J.R. Hughes. Yzβ discontinuity capturing for advection-dominated processes with application to arterial drug delivery. *International Journal for Numerical Methods in Fluids*, 54(6-8):593–608, 2007.

A.N. Brooks and T.J.R. Hughes. Streamline upwind/petrov-galerkin formulations for convection dominated flows with particular emphasis on the incompressible navier-stokes equations. *Computer methods in applied mechanics and engineering*, 32(1):199–259, 1982.

E.J. Caramana, M.J. Shashkov, and P.P. Whalen. Formulations of artificial viscosity for multi-dimensional shock wave computations. *Journal of Computational Physics*, 144(1): 70–97, 1998.

R.B. Christensen. Godunov methods on a staggered mesh-an improved artificial viscosity. *Lawrence Livermore National Laboratory Report UCRL-JC-105269*, 1990.

R. Codina, J. Principe, O. Guasch, and S. Badia. Time dependent subscales in the stabilized finite element approximation of incompressible flow problems. *Computer Methods in Applied Mechanics and Engineering*, 196(21):2413–2430, 2007.

A. Corsini, F. Rispoli, and A. Santoriello. A variational multiscale higher-order finite element formulation for turbomachinery flow computations. *Computer methods in applied mechanics and engineering*, 194(45):4797–4823, 2005.

J.A. Evans, T.J.R. Hughes, and G. Sangalli. Enforcement of constraints and maximum principles in the variational multiscale method. *Computer Methods in Applied Mechanics and Engineering*, 199(1):61–76, 2009.

J. Guermond and R. Pasquetti. Entropy viscosity method for high-order approximations of conservation laws. In *Spectral and High Order Methods for Partial Differential Equations*, pages 411–418. Springer, 2011.

J. Guermond, R. Pasquetti, and B. Popov. Entropy viscosity method for nonlinear conservation laws. *Journal of Computational Physics*, 230(11):4248–4267, 2011.

T.J.R. Hughes and M. Mallet. A new finite element formulation for computational fluid dynamics: Iv. a discontinuity-capturing operator for multidimensional advective-diffusive systems. *Computer Methods in Applied Mechanics and Engineering*, 58(3):329–336, 1986.

T.J.R. Hughes and G. Sangalli. Variational multiscale analysis: the fine-scale green's function, projection, optimization, localization, and stabilized methods. *SIAM Journal on Numerical Analysis*, 45(2):539–557, 2007.

T.J.R. Hughes, G.R. Feijóo, L. Mazzei, and J.B. Quincy. The variational multiscale methoda paradigm for computational mechanics. *Computer methods in applied mechanics and engineering*, 166(1):3–24, 1998.

J.K. Hunter and B. Nachtergaele. *Applied analysis*. World Scientific Pub Co Inc, 2001.

C. Johnson, A. Szepessy, and P. Hansbo. On the convergence of shock-capturing streamline diffusion finite element methods for hyperbolic conservation laws. *Mathematics of computation*, 54(189):107–129, 1990.

J Larsson. Unphysical damping of turbulence when passing a numerically captured shock. *Annu. Res. Briefs, Center for Turbulence Research*, 2009.

G.J. Le Beau and T.E. Tezduyar. Finite element computation of compressible flows with the supg formulation. *Advances in finite element analysis in fluid dynamics, FED*, 123:21–27, 1991.

M. Nazarov and J. Hoffman. An adaptive finite element method for inviscid compressible flow. *International Journal for Numerical Methods in Fluids*, 64(10-12):1102–1128, 2010.

M. Nazarov and J. Hoffman. Residual-based artificial viscosity for simulation of turbulent compressible flow using adaptive finite element methods. *International Journal for Numerical Methods in Fluids*, 71(3):339–357, 2013.

W.F. Noh. Errors for calculations of strong shocks using an artificial viscosity and an artificial heat flux. *Journal of Computational Physics*, 72(1):78–120, 1987.

J.T. Oden and L. Demkowicz. *Applied functional analysis*. CRC press, 2010.

F. Rispoli and G.Z. Rafael Saavedra. A stabilized finite element method based on sgs models for compressible flows. *Computer methods in applied mechanics and engineering*, 196(1): 652–664, 2006.

F. Rispoli, A. Corsini, and T.E. Tezduyar. Finite element computation of turbulent flows with the discontinuity-capturing directional dissipation (dcdd). *Computers & fluids*, 36(1): 121–126, 2007.

M.D. Salas. A brief history of shock-fitting. In *Computational Fluid Dynamics 2010*, pages 37–53. Springer, 2011.

G. Scovazzi. *Multiscale methods in science and engineering*. PhD thesis, Stanford University, 2004.

F. Shakib, T.J.R. Hughes, and Z. Johan. A new finite element formulation for computational fluid dynamics: X. the compressible euler and navier-stokes equations. *Computer Methods in Applied Mechanics and Engineering*, 89(1):141–219, 1991.

A. Szepessy. Convergence of a shock-capturing streamline diffusion finite element method for a scalar conservation law in two space dimensions. *Mathematics of computation*, 53(188): 527–545, 1989.

A. Szepessy. Convergence of a streamline diffusion finite element method for a conservation law with boundary conditions. *RAIRO Modelling and numerical analysis modelisations*, 25 (5):749–783, 1991.

E. Tadmor. Convergence of spectral methods for nonlinear conservation laws. *SIAM Journal on Numerical Analysis*, 26(1):30–44, 1989.

T.E. Tezduyar. Finite element methods for fluid dynamics with moving boundaries and interfaces. *Encyclopedia of computational mechanics*, 2004.

T.E. Tezduyar and M. Senga. Stabilization and shock-capturing parameters in supg formulation of compressible flows. *Computer methods in applied mechanics and engineering*, 195 (13):1621–1632, 2006.

T.E. Tezduyar and M. Senga. Supg finite element computation of inviscid supersonic flows with yzβ shock-capturing. *Computers & fluids*, 36(1):147–159, 2007.

T.E. Tezduyar, M. Senga, and D. Vicker. Computation of inviscid supersonic flows around cylinders and spheres with the supg formulation and yzβ shock-capturing. *Computational Mechanics*, 38(4-5):469–481, 2006.

ML Wilkins. Use of artificial viscosity in multidimensional shock wave problems. *J. Comput. Phys*, 36:281–303, 1980.

J. G. Wouchuk, C. Huete Ruiz de Lira, and A. L. Velikovich. Analytical linear theory for the interaction of a planar shock wave with an isotropic turbulent vorticity field. *Phys. Rev. E*, 79:066315, Jun 2009. doi: 10.1103/PhysRevE.79.066315. URL http://link.aps.org/doi/10.1103/PhysRevE.79.066315.

H.C. Yee, B. Sjögreen, N.D. Sandham, and A. Hadjadj. Progress in the development of a class of efficient low dissipative high order shock-capturing methods. In *Computational Fluid Dynamics for the 21st Century*, pages 77–102. Springer, 2001.

G.P. Zank, Y. Zhou, W.H. Matthaeus, and W.K.M. Rice. The interaction of turbulence with shock waves: A basic model. *Physics of Fluids (1994-present)*, 14(11):3766–3774, 2002.

Appendix A

Green's Function

"The inverse of a linear differential operator is an integral operator, whose kernel is called the Green's function of the differential operator."(chapter 10 in Hunter and Nachtergaele (2001)) What a Green's function does qualitatively is best explained by this paragraph from *"Green's functions: Introductory theory with applications"* by G.F.Roach:

"The two point function $G(x, y)$ is understood as describing that displacement of the system at a point x which is due to a unit force applied at point y. It follows from the symmetry of the function $G(x, y)$ that $G(x, y)$ also represents that displacement at y which is due to a unit applied force at x. Consequently, if we multiply $G(x, y)$ by an appropriate weighting factor, and integrate over all possible points in the region of interest, we shall get that total displacement of the system at the point y which is due to an applied force distributed according to the behaviour of the function $f(x)$. That is, we obtain the required solution to our problem."

A.1 Expressing the small-scale solution in terms of a Green's function

Consider the abstract problem given in Chapter 2 and define the global Green's operator $\mathcal{G}$ as

$$u = \mathcal{G}f, \tag{A.1}$$

it represents the Green's function $g : \Omega \times \Omega \to \mathbb{R}$:

$$u(\mathbf{y}) = \int_{\Omega} g(\mathbf{x}, \mathbf{y}) f(\mathbf{x}) d\mathbf{x}. \tag{A.2}$$

Similarly one can define a small-scale Green's operator $\mathcal{G}'$ for the small-scale problem (2.22), the small-scale Green's function is a function $g' : \Omega \times \Omega \to \mathbb{R}$ s.t.:

$$u'(\mathbf{y}) = \int_\Omega g'(\mathbf{x}, \mathbf{y})(f - L\bar{u})(\mathbf{x})d\mathbf{x} \tag{A.3}$$

$$u' = \mathcal{G}'R'(\bar{u}) \tag{A.4}$$

with R' being the residual of the large-scale solution projected onto the fine scales:

$$(w', R'(\bar{u})) = F(w') - B(w', \bar{u}) \quad \forall w' \in \mathcal{V}'. \tag{A.5}$$

So the small scales u' are a function of the residual of the large scales $f - L\bar{u}$. Note however that g' is defined in the space $\mathcal{V}'$ and so it is not the Green's function associated with the strong form of (A.3). An exact expression for $\mathcal{G}'$ was found by Hughes and Sangalli (2007):

$$\mathcal{G}' = \mathcal{G} - \mathcal{G}\mathcal{P}^T(\mathcal{P}\mathcal{G}\mathcal{P}^T)^{-1}\mathcal{P}\mathcal{G} \tag{A.6}$$

By substituting (A.4) into (2.24) the following is obtained:

$$B(\bar{w}, \bar{u}) + (L^*\bar{w}, G'(f - L\bar{u})) = (\bar{w}, f) \quad \forall \bar{w} \in \bar{\mathcal{V}}, \tag{A.7}$$

with

$$(L^*\bar{w}, G'(f - L\bar{u})) = \int_\Omega \int_\Omega (L^*\bar{w}(\mathbf{y})g')(\mathbf{x}, \mathbf{y})(f - L\bar{u})(\mathbf{x})d\mathbf{x}d\mathbf{y}. \tag{A.8}$$

Note that (A.7) is an exact equation for the large scales (remember that (2.17) was split up into two problems: one for the large scales and one for the small scales).

In the finite element method the domain Ω is split up into elements with domain Ω^e and boundary Γ^e, the domain Ω' is defined as as the union of the element domains and Γ' is the union of the element boundaries modulo the element interfaces (Γ):

$$\begin{aligned} \Omega' &= \cup_{e=1}^{n_{el}} \Omega^e \\ \Gamma' &= (\cup_{e=1}^{n_{el}} \Gamma^e) \, \Gamma \end{aligned} \tag{A.9}$$

Furthermore $[\![\cdot]\!]$ is the jump operator and b^* is the boundary operator.This means that now, by integration by parts, the following should hold:

$$B(\bar{w}, u') = \sum_{e=1}^{n_{el}} \left(L^*\bar{w}, u')_{\Omega^e} + (b^*\bar{w}, u')_{\Gamma^e} \right), \tag{A.10}$$

$$= (L^*\bar{w}, u')_{\Omega'} + ([\![b^*\bar{w}]\!], u')_{\Gamma'}, \tag{A.11}$$

$$= (L^*\bar{w}, u')_{\Omega}. \tag{A.12}$$

$$B(w', \bar{u}) = \sum_{e=1}^{n_{el}} \left(w', L\bar{u})_{\Omega^e} + (w', b\bar{u})_{\Gamma^e} \right), \tag{A.13}$$

$$= (w', L\bar{u})_{\Omega'} + (w', [\![b\bar{u}]\!])_{\Gamma'}, \tag{A.14}$$

$$= (w', L\bar{u})_{\Omega}. \tag{A.15}$$

$$B(w', u') = \sum_{e=1}^{n_{el}} \left(w', Lu' \right)_{\Omega^e} + \left(w', bu' \right)_{\Gamma^e} \Big), \tag{A.16}$$

$$= (w', Lu')_{\Omega'} + (w', [\![bu']\!])_{\Gamma'}, \tag{A.17}$$

$$= (w', Lu')_{\Omega}. \tag{A.18}$$

With the above equations in mind the exact expression for u' becomes:

$$u'(\mathbf{y}) = \int_{\Omega} g'(\mathbf{x}, \mathbf{y})(f - L\bar{u})(\mathbf{x}) d\mathbf{x} \tag{A.19}$$

$$= \int_{\Omega'} g'(\mathbf{x}, \mathbf{y})(f - L\bar{u})(\mathbf{x}) d\mathbf{x} - \int_{\Gamma'} g'(\mathbf{x}, \mathbf{y}) [\![b\bar{u}]\!](\mathbf{x}) d\mathbf{x} \tag{A.20}$$

$$= \sum_{e=1}^{n_{el}} \left(\int_{\Omega^e} g'(\mathbf{x}, \mathbf{y})(f - L\bar{u})(\mathbf{x}) d\mathbf{x} - \int_{\Gamma^e} g'(\mathbf{x}, \mathbf{y})(b\bar{u})(\mathbf{x}) d\mathbf{x} \right) \tag{A.21}$$

By substituting (A.21) into (A.7), the exact expression for the small-scale effect on the large scales is:

$$\begin{aligned}
(L^*\bar{w}, G'(L\bar{u} - f)) = &- \int_{\Omega} \int_{\Omega} (L^*\bar{w})(y) g'(x, y)(L\bar{u} - f)(x) d\Omega_x d\Omega_y \\
= &- \int_{\Omega'} \int_{\Omega'} (L^*\bar{w})(y) g'(x, y)(L\bar{u} - f)(x) d\Omega_x d\Omega_y \\
&- \int_{\Omega'} \int_{\Gamma'} (L^*\bar{w}(y) g'(x, y) [\![b\bar{u}]\!](x) d\Gamma_x d\Omega_y \\
&- \int_{\Gamma'} \int_{\Omega'} [\![b^*\bar{w}]\!](y) g'(x, y)(L\bar{u} - f)(x) d\Omega_x d\Gamma_y \\
&- \int_{\Gamma'} \int_{\Gamma'} [\![b^*\bar{w}]\!](y) g'(x, y) [\![b\bar{u}]\!](x) d\Gamma_x d\Gamma_y \\
= &- \sum_{e=1}^{n_{el}} \sum_{l=1}^{n_{el}} \left(\int_{\Omega^e} \int_{\Omega^l} (L^*\bar{w})(y) g'(x, y)(L\bar{u} - f)(x) d\Omega_x d\Omega_y \right. \\
&- \int_{\Omega^e} \int_{\Gamma^l} (L^*\bar{w}(y) g'(x, y)(b\bar{u})(x) d\Gamma_x d\Omega_y \\
&- \int_{\Gamma^e} \int_{\Omega^l} (b^*\bar{w})(y) g'(x, y)(L\bar{u} - f)(x) d\Omega_x d\Gamma_y \\
&\left. - \int_{\Gamma^e} \int_{\Gamma^l} (b^*\bar{w})(y) g'(x, y)(b\bar{u})(x) d\Gamma_x d\Gamma_y \right)
\end{aligned} \tag{A.22}$$

All of the above *exact expressions* are very nice, but in practice, u', $\mathcal{G}$ and $\mathcal{G}'$ are not known and so approximations are needed.

A.2 The exact Green's function for the convection-diffusion equation

From the definition of the Green's function, one can see that the element Green's function of the convection-diffusion problem (2.36) must satisfy

$$-a\frac{\partial g_e(x,y)}{\partial x} - k\frac{\partial^2 g_e(x,y)}{\partial x^2} = \delta(x,y) \quad \forall x \in \Omega_e \tag{A.23}$$

and

$$g_e(x,y) = 0 \quad \forall x \in \Gamma_e. \tag{A.24}$$

Using ξ as the reference element coordinate and x as the physical coordinate, then in the case of linear shape functions, the Jacobian of the mapping from the reference element to physical coordinates is:

$$J = \frac{\partial x}{\partial \xi} = x_{,\xi} = h \tag{A.25}$$

with h being the element size. The Jacobian of the inverse mapping, form physical to reference coordinates is then:

$$J^{-1} = \frac{\partial \xi}{\partial x} = \xi_{,x} = \frac{1}{h}. \tag{A.26}$$

This means that the relation of the Dirac delta function on the parent element and physical coordinates is:

$$\delta(x,y) = J^{-1}\delta(\xi,\zeta) = \frac{1}{h}\delta(\xi,\zeta). \tag{A.27}$$

Now transferring (A.23) to the parent element yields:

$$\begin{aligned} -(J^{-1})ag_e(\xi,\zeta)_{,\xi} - (J^{-1})^2 kg_e(\xi,\zeta)_{,\xi\xi} &= (J^{-1})\delta(\xi,\zeta) \\ -ag_e(\xi,\zeta)_{,\xi} - (J^{-1})kg_e(\xi,\zeta)_{,\xi\xi} &= \delta(\xi,\zeta) \\ -ag_e(\xi,\zeta)_{,\xi} - \frac{1}{h}kg_e(\xi,\zeta)_{,\xi\xi} &= \delta(\xi,\zeta) \quad \text{with } \xi,\zeta \in]0,1[\end{aligned} \tag{A.28}$$

and

$$\begin{aligned} g_e(0,\zeta) &= 0, \\ g_e(1,\zeta) &= 0. \end{aligned} \tag{A.29}$$

The solution of the above differential equation will be of the form

$$g_e(\xi,\zeta) = C_1(\zeta)e^{\lambda_1\xi} + C_2(\zeta)e^{\lambda_2\xi} \quad 0 \le \xi \le \zeta, \tag{A.30}$$

$$g_e(\xi,\zeta) = C_3(\zeta)e^{\lambda_1\xi} + C_4(\zeta)e^{\lambda_2\xi} \quad \zeta < \xi \le 1. \tag{A.31}$$

$$\tag{A.32}$$

And λ_1 and λ_2 can be determined by finding the roots of the characteristic equation:

$$\lambda_1 = -\frac{ah}{k}, \tag{A.33}$$

$$\lambda_2 = 0. \tag{A.34}$$

To find C_1, C_2, C_3 and C_4, four conditions are needed. The first two conditions are the boundary conditions A.29, the third condition comes from the requirement for continuity in the element interior:

$$g_e(\zeta^+, \zeta) = g_e(\zeta^-, \zeta). \tag{A.35}$$

The final condition can be found by noting that the first derivative of the element Green's function has a discontinuity at $\xi = \zeta$, this can be found by integrating (A.28) across $\xi = \zeta$.

$$\int_{\zeta^-}^{\zeta^+} \left(-a\frac{\partial g_e(\xi,\zeta)}{\partial \xi} - \frac{k}{h}\frac{\partial^2 g_e(\xi,\zeta)}{\partial \xi^2} \right) d\xi = \int_{\zeta^-}^{\zeta^+} \delta(\xi,\zeta) d\xi \tag{A.36}$$

$$-a\left[g_e(\xi,\zeta)\right]_{\zeta^-}^{\zeta^+} - \frac{k}{h}\left[\frac{\partial g_e(\xi,\zeta)}{\partial \xi}\right]_{\zeta^-}^{\zeta^+} = 1 \tag{A.37}$$

$$g_e(\zeta^+,\zeta)_{,\xi} - g_e(\zeta^-,\zeta)_{,\xi} = -\frac{h}{k}. \tag{A.38}$$

From these conditions the values of the coefficients C_1 through C_4 can be computed, the result is:

$$\begin{aligned} C_1 &= \frac{h}{k}\frac{e^{\lambda_1(1-\zeta)} - 1}{\lambda_1(e^{\lambda_1} - 1)}, \\ C_2 &= \frac{h}{k}\frac{e^{\lambda_1(1-\zeta)} - 1}{\lambda_1(e^{\lambda_1} - 1)}, \\ C_3 &= \frac{h}{k\lambda_1}\frac{1 - e^{-\lambda_1\zeta}}{1 - e^{\lambda_1}}, \\ C_4 &= \frac{h}{k\lambda_1}\frac{e^{\lambda_1} - e^{\lambda_1(1-\zeta)}}{e^{\lambda_1} - 1}. \end{aligned} \tag{A.39}$$

A.2.1 Approximating the fine scale element Green's function with a stabilization parameter τ

Using a Dirac delta function, τ can be written as

$$\tau = \int_{\Omega_e} \tau \cdot \delta(x,y) dx. \tag{A.40}$$

And defining $\tilde{g}'_e(x,y)$ as an approximation to the element Green's function

$$\tilde{g}'_e(x,y) = \tau \cdot \delta(x,y). \tag{A.41}$$

Since $\tilde{g}'_e(x,y)$ is an approximation of the fine scale element Green's function $g'_e(x,y)$, (A.40) can also be written as

$$\tau(y) = \int_{\Omega_e} g'_e(x,y)dx. \tag{A.42}$$

Note that so far $g'_e(x,y)$ and $\tau(y)$ are arbitrary functions, so all of the above will also hold after a change of variables:

$$g'_e(x,y) = g'_e(\xi,\zeta) \quad \tau(y) = \tau(\xi). \tag{A.43}$$

This means that τ can be computed on the parent domain as

$$\begin{aligned}
\tau(\zeta) &= \int_0^1 g'_e(\xi,\zeta)\det(J)d\xi \\
&= h\int_0^1 g'_e(\xi,\zeta)d\xi \\
&= h\left[\int_0^\zeta g'_e(\xi,\zeta)_{0\leq\xi\leq\zeta}d\xi + \int_\zeta^1 g'_e(\xi,\zeta)_{\zeta<\xi\leq 1}d\xi\right] \\
&= h\left[\frac{C_1}{\lambda_1}e^{\lambda_1\zeta} + C_2\zeta - \frac{C_1}{\lambda_1} + \frac{C_3}{\lambda_1}e^{\lambda_1} + C_4 - \frac{C_3}{\lambda_1}e^{\lambda_1\zeta} - C_4\zeta\right] \\
&= -\frac{h}{a}\frac{\zeta - 1 + e^{\frac{ah}{k}\zeta} - e^{\frac{ah}{k}}\zeta}{e^{\frac{ah}{k}} - 1}.
\end{aligned} \tag{A.44}$$

Appendix B

Some definitions from functional analysis

In this appendix a short review of some definitions form functional analysis is given. This is by no means an exhaustive or rigorous overview, for a more extensive and structured reading the following resources are recommended Oden and Demkowicz (2010) and Atkinson (2009).

Norm

Given a linear space V, a norm $||\cdot||$ is a function from V to $\mathbb{R}$ that satisfies three rules:

1. $||\alpha v|| = |\alpha|\ ||v||\ \forall v \in V$ and $\alpha \in \mathbb{K}$
2. $||v|| \geq 0\ \forall v \in V$ and $||v|| = 0 \iff v = 0$
3. $||u + v|| = ||u|| + ||v||\ \forall u, v \in V$

A norm can be induced by an inner product as follows:

$$||u|| = \sqrt{(u, u)}$$

where $(\cdot, \cdot)$ is the inner product.

Operator

Operators have a lot of synonyms, people also call them maps, transformations or functions. $L : U \to V$ is a map or operator from the space U to the space V. It is a function (just a rule if you will) that assigns to every $u \in U$ an unique element $v \in V$.
The operator L is called a *linear operator* if

$$L(\alpha u_1 + \beta u_2) = \alpha L(u_1) + \beta L(u_2) \text{ with } u_1, u_2 \in U \text{ and } \alpha, \beta \in \mathbb{R}$$

The operator $L : U \to V$ is *bounded* if there exists a constant $C > 0$ such that $||Lu||_V \leq C||u||_U$ for all $u \in U$.

$L : U \to V$ is called a *continuous* operator if for every sequence $\{u_n\}$ in U that converges to the limit u in U the following holds:

$$L(u_n) \to L(u)$$

$\mathcal{L}(U, V)$ is the space of all bounded linear operators from U to V. It is itself a normed space using the operator norm:

$$||L|| = \sup_{||u||_U=1} ||L(u)||_V = \sup_{u \neq 0} \frac{||L(u)||_V}{||u||_U}$$

Linear functional

A linear map from space V to $\mathbb{R}$ is called a linear functional.

Dual or adjoint space

For a normed space V, its *dual space* is the space of bounded linear functionals on V: $\mathcal{L}(V, \mathbb{R})$, also written as V^*. V^* is a normed space under the dual norm. Let l be a linear functional such that $l \in \mathcal{L}(V, \mathbb{R})$ or equivalently $l \in V^*$, then the dual norm is:

$$||l||_{V^*} = \sup_{v \in V, ||v||_V=1} |l(v)| = \sup_{v \in V, v \neq 0} \frac{|l(v)|}{||v||_V}$$

Bracket notation

Let V be a normed space over $\mathbb{R}$ and V^* be its dual space, then for every $v \in V$ and $l \in V^*$ one can say:

$$l(v) = \langle v, l \rangle.$$

C^n spaces

The space of continuous functions in the interval $[a, b]$, with $a, b \in \mathbb{R}$, is $C([a, b])$. This can be generalized by taking Ω to be a domain in $\mathbb{R}^n$, then the space of continuous functions on Ω is $C(\Omega)$. The space of functions with a continuous first derivative on $[a, b]$ is called $C^1([a, b])$. And the reader can now guess what the function spaces $C^2([a, b])$, $C^3([a, b])$ and so on are.

L^p spaces

Let Ω be a domain in $\mathbb{R}^n$, and $1 \leq p \leq \infty$. The space $L^p(\Omega)$ is the space of functions that are measurable on Ω and bounded in the p-norm:

$$L^p(\Omega) = \{f : f \text{ is measurable on } \Omega \text{ and } ||f||_p \leq \infty\}$$

and the p-norm is defined as:

$$||f||_p = \left(\int_\Omega |f|^p d\Omega \right)^{1/p}$$

except for the case $p = \infty$:

$$||f||_\infty = \text{ess.} \sup_\Omega |f|.$$

Banach space

A space with a norm such that every Cauchy sequence converges to a limit within the space is a Banach space. It is also a complete space. Some examples of Banach spaces are the L^P spaces and $C([a, b])$.

Hilbert and Sobolev spaces

A Hilbert space is a complete inner product space.
Riesz representation theorem: For each bounded linear functional F on a Hilbert space V, there is a unique element $u \in V$ such that for all $v \in V$:

$$F(v) = (v, u) \text{ and } ||u||_{V^*} = \sup_{v \in V, v \neq 0} \frac{|F(v)|}{||v||}$$

$W^{m,p}(\Omega)$, with $1 \leq p \leq \infty$ and $m \in \mathbb{Z}$, is a Sobolev space containing the functions in $L^p(\Omega)$ whose derivatives (in the distributional sense) of order m or less are also in $L^p(\Omega)$. Is is a Banach space with the $|| \cdot ||_{W^{m,p}(\Omega)}$-norm.

$$||v||_{W^{m,p}(\Omega)} = \left(\sum_{|j| \leq m} ||D^j v||^p_{L^p(\Omega)} \right)^{1/p}$$

where j is a multi-index $j = (j_1, \ldots, j_n)$, and the length $|j|$ of a multi-index is defined as $|j| = \sum_{i=1}^n j_i$. So the differential operator D^j is defined as

$$D^j = D_1^{j_1} \ldots D_n^{j_n} = \frac{\partial^{|j|}}{\partial x_1^{j_1} \ldots \partial x_n^{j_n}}.$$

If $p = 2$, $W^{m,2}(\Omega)$ is a Hilbert space: $W^{m,2}(\Omega) = H^m(\Omega)$ and this Hilbert space has the inner product

$$(u, v)_{H^m(\Omega)} = \sum_{|j| \leq m} (D^j u, D^j v)$$

A subspace of $H^m(\Omega)$ containing functions that vanish on the boundary is known as H_0^m:

$$H_0^m(\Omega) = \{u \in H^m(\Omega) : u = \frac{\partial u}{\partial n} \dots \frac{\partial^{m-1} u}{\partial n^{m-1}} = 0 \text{ on } \partial\Omega\}$$

The dual space of $H_0^m(\Omega)$ is $H^{-m}(\Omega)$.

Dual or adjoint operator

Let U and V be normed spaces, and U^* and V^* their dual spaces. Furthermore use $u \in U$, $v \in V$, $u^* \in U^*$, $v^* \in V*$ and define a bounded linear transformation $L \in \mathcal{L}(U, V)$ as $L : U \to V$. Then the adjoint operator L^* is defined by:

$$v^*(L(u)) = L^* v^*(u)$$

or in bracket notation

$$\langle L(u), v^* \rangle = \langle u, L^*(v^*) \rangle,$$

the above indentity is called the *bilinear identity*.
If $U = \mathbb{R}^m$ and $V = \mathbb{R}^n$, then using the standard inner product, one can use the Riesz representation theorem to formulate that bilinear identity for $L \in \mathcal{L}(\mathbb{R}^m, \mathbb{R}^n)$ as

$$(Lu, v) = (u, L^* v) \text{ with } u \in \mathbb{R}^m, v \in \mathbb{R}^n.$$

Appendix C

Detailed discretization of Burgers' equation

$$\frac{\partial u}{\partial t} + u\frac{\partial u}{\partial x} - \nu\frac{\partial^2 u}{\partial x^2} = f \quad \text{with } \nu > 0. \tag{C.1}$$

C.0.2 Discretization

For the time discretization a generalized trapezoidal rule will be used:

$$u^{n+\theta} = \theta u^{n+1} + (1-\theta)u^n, \tag{C.2}$$

where the superscript indicates the time step. By setting θ to 0, 0.5 or 1 the time discretization becomes forward Euler, Crank-Nicolson or backward Euler respectively. For Burgers' equation this yields

$$\frac{u^{n+1} - u^n}{\Delta t} + u^n\frac{\partial\left(\theta u^{n+1} + (1-\theta)u^n\right)}{\partial x} - \nu\frac{\partial^2\left(\theta u^{n+1} + (1-\theta)u^n\right)}{\partial x^2} = f. \tag{C.3}$$

Now the variational form of this equation is

$$\begin{aligned}\frac{(w, u^{n+1}) - (w, u^n)}{\Delta t} + \theta\left(w, u^n\frac{\partial u^{n+1}}{\partial x}\right) + (1-\theta)\left(w, u^n\frac{\partial u^n}{\partial x}\right) \\ - \nu\left[\theta\left(w, \frac{\partial^2 u^{n+1}}{\partial x^2}\right) + (1-\theta)\left(w, \frac{\partial^2 u^n}{\partial x^2}\right)\right] = (w, f),\end{aligned} \tag{C.4}$$

where the operator $(\cdot,\cdot)$ signifies integration over the spatial domain Ω: $(a,b) = \int_\Omega a \cdot b d\Omega$. Using integration by parts on the diffusion terms, and assuming homogeneous boundary conditions, this becomes:

$$\begin{aligned}\frac{(w,u^{n+1})-(w,u^n)}{\Delta t}+\theta\left(w,u^n\frac{\partial u^{n+1}}{\partial x}\right)+(1-\theta)\left(w,u^n\frac{\partial u^n}{\partial x}\right)\\ +\nu\left[\theta\left(\frac{\partial w}{\partial x},\frac{\partial u^{n+1}}{\partial x}\right)+(1-\theta)\left(\frac{\partial w}{\partial x},\frac{\partial u^n}{\partial x}\right)\right]=(w,f).\end{aligned} \tag{C.5}$$

Eq. C.5 can be rearranged into:

$$\begin{aligned}&\frac{1}{\Delta t}(w,u^{n+1})+\theta\left(w,u^n\frac{\partial u^{n+1}}{\partial x}\right)+\nu\theta\left(\frac{\partial w}{\partial x},\frac{\partial u^{n+1}}{\partial x}\right)\\ &\quad=(w,f)+\frac{1}{\Delta t}(w,u^n)-(1-\theta)\left(w,u^n\frac{\partial u^n}{\partial x}\right)-\nu(1-\theta)\left(\frac{\partial w}{\partial x},\frac{\partial u^n}{\partial x}\right).\end{aligned} \tag{C.6}$$

C.0.3 Variational Multiscale Formulation

The basic concept of a two-scale multiscale method is to split up the solution into a large-scale and a small scale solution by taking $u=\bar{u}+u'$. This also means splitting up the trial function and test function spaces such that:

$$\mathcal{S}=\bar{\mathcal{S}}\oplus\mathcal{S}' \tag{C.7}$$
$$\mathcal{V}=\bar{\mathcal{V}}\oplus\mathcal{V}' \tag{C.8}$$

with the boundary conditions now becoming:

$$\bar{u}=g \text{ on } \Gamma \quad \forall\bar{u}\in\bar{\mathcal{S}}, \tag{C.9}$$
$$u'=0 \text{ on } \Gamma \quad \forall u'\in\mathcal{S}', \tag{C.10}$$
$$\bar{w}=0 \text{ on } \Gamma \quad \forall\bar{w}\in\bar{\mathcal{V}}, \tag{C.11}$$
$$w'=0 \text{ on } \Gamma \quad \forall w'\in\mathcal{V}'. \tag{C.12}$$

It is now possible to work out a small-scale and a large-scale equation. By writing out Eq. 2.21 one comes to the small-scale equation is:

$$\begin{aligned}&\frac{1}{\Delta t}(w',u'^{n+1})+\theta\left(w',u^n\frac{\partial u'^{n+1}}{\partial x}\right)+\nu\theta\left(\frac{\partial w'}{\partial x},\frac{\partial u'^{n+1}}{\partial x}\right)\\ &\quad=(w',f)+\frac{1}{\Delta t}(w',u'^n)-(1-\theta)\left(w',u^n\frac{\partial u'^n}{\partial x}\right)-\nu(1-\theta)\left(\frac{\partial w'}{\partial x},\frac{\partial u'^n}{\partial x}\right)\\ &\quad-\frac{1}{\Delta t}(w',\bar{u}^{n+1})-\left(w',u^n\left(\theta\frac{\partial\bar{u}^{n+1}}{\partial x}+(1-\theta)\frac{\partial\bar{u}^n}{\partial x}\right)\right)-\nu\left(\frac{\partial w'}{\partial x},\theta\frac{\partial\bar{u}^{n+1}}{\partial x}+(1-\theta)\frac{\partial\bar{u}^n}{\partial x}\right),\end{aligned} \tag{C.13}$$

and using Eq. 2.23, the large-scale equation becomes:

$$\begin{aligned}
&\frac{1}{\Delta t}(\bar{w},\bar{u}^{n+1})+\theta\left(\bar{w},u^n\frac{\partial\bar{u}^{n+1}}{\partial x}\right)+\nu\theta\left(\frac{\partial\bar{w}}{\partial x},\frac{\partial\bar{u}^{n+1}}{\partial x}\right)\\
&\quad=(\bar{w},f)+\frac{1}{\Delta t}(\bar{w},\bar{u}^n)-(1-\theta)\left(\bar{w},u^n\frac{\partial\bar{u}^n}{\partial x}\right)-\nu(1-\theta)\left(\frac{\partial\bar{w}}{\partial x},\frac{\partial\bar{u}^n}{\partial x}\right)\\
&\quad-\frac{1}{\Delta t}(\bar{w},u'^{n+1})-\left(\bar{w},u^n\left(\theta\frac{\partial u'^{n+1}}{\partial x}+(1-\theta)\frac{\partial u'^n}{\partial x}\right)\right)-\nu\left(\frac{\partial\bar{w}}{\partial x},\theta\frac{\partial u'^{n+1}}{\partial x}+(1-\theta)\frac{\partial u'^n}{\partial x}\right).
\end{aligned}\tag{C.14}$$

C.0.4 Stabilization

A stabilized method is usually of the form

$$a(w,\mathbf{u})+(\mathbf{L}w,\tau(\mathcal{L}\mathbf{u}-\mathbf{f}))=(w,\mathbf{f}),\tag{C.15}$$

where $\mathbf{L}$ is some operator (for GLS $\mathbf{L}=\mathcal{L}$ and for SUPG $\mathbf{L}=\mathcal{L}_{adv}$) and τ is an algebraic operator, also called the intrinsic length scale. Stabilization of this form has a strong link with the variational multiscale method.

For Burgers' equation this τ, computed following the method of Shakib et al. (1991), is:

$$\tau=\left[\left(\frac{2}{\Delta t}\right)^2+\left(\frac{2a(u)}{h}\right)^2+\left(\frac{4\nu}{h^2}\right)^2\right]^{-\frac{1}{2}}\tag{C.16}$$

where $a(u)$ is some convection speed which is a function of u. In this case it was taken to be the local velocity. And h in Eq. C.16 is the size of the mesh in the flow direction (easy in here since it is a 1D case). The general variational form of 1D Burgers' equation with SUPG stabilization reads:

$$(w,u_t+uu_x-\nu u_{xx})+\left(uw_x,\left[\left(\frac{2}{\Delta t}\right)^2+\left(\frac{2u}{h}\right)^2+\left(\frac{4\nu}{h^2}\right)^2\right]^{-\frac{1}{2}}(u_t+uu_x-\nu u_{xx}-f)\right)=(w,f)\tag{C.17}$$

where $u_t=\partial u/\partial t$ and $u_x=\partial u/\partial x$. Eq. C.5 with the SUPG stabilization term becomes:

$$\begin{aligned}
&\frac{(w,u^{n+1})-(w,u^n)}{\Delta t}+\theta\left(w,u^n\frac{\partial u^{n+1}}{\partial x}\right)+(1-\theta)\left(w,u^n\frac{\partial u^n}{\partial x}\right)\\
&\quad+\nu\left[\theta\left(\frac{\partial w}{\partial x},\frac{\partial u^{n+1}}{\partial x}\right)+(1-\theta)\left(\frac{\partial w}{\partial x},\frac{\partial u^n}{\partial x}\right)\right]\\
&\quad+\left(u\frac{\partial w}{\partial x},\tau\left[\frac{u^{n+1}}{\Delta t}+u^n\frac{\partial x^{n+1}}{\partial x}-\nu\theta\left(\frac{\partial u^{n+1}}{\partial^2 x^2}\right)\right]\right)\\
&\quad=(w,f)-\left(u\frac{\partial w}{\partial x},\tau\left[\frac{u^n}{\Delta t}-(1-\theta)u^n\frac{\partial u^n}{\partial x}+\nu(1-\theta)\frac{\partial^2 u^n}{\partial x^2}\right]\right).
\end{aligned}\tag{C.18}$$

Appendix D

Stationary shock error data

D.1 Stabilization and shock-capturing methods

h	$1/65$	$1/35$	$1/15$	$1/5$
DCDD H^1 error	5.48817	3.94425	2.14904	0.563537
DCDD L^2 error	0.0507345	0.0685667	0.0968429	0.124882
MSC H^1 error	0.100771	0.0958584	0.0870473	0.107109
MSC L^2 error	0.0264213	0.0362112	0.0555655	0.0920219
SUPG H^1 error	4.48305	2.68486	1.07392	0.276045
SUPG L^2 error	0.0462064	0.0581953	0.0747669	0.107876
V-SGS H^1 error	6.9027	4.86579	2.82154	1.04125
V-SGS L^2 error	0.083031	0.102537	0.13086	0.163865
YZB1 H^1 error	6.91698	4.87686	2.82854	0.982175
YZB1 L^2 error	0.0834986	0.102969	0.130837	0.158869
YZB2 H^1 error	4.60271	2.97074	1.25074	0.24967
YZB2 L^2 error	0.0424544	0.0570628	0.0768168	0.10592
clean H^1 error	13.4685	5.18057	1.32495	0.252284
clean L^2 error	0.0553096	0.0396203	0.0435608	0.0848977

Table D.1: Errors for different mesh size at $t = 0.1$(with time step $\Delta t = {}^{h}/_{6}$, resulting in a Courant number of $Cr = 0.25$)

h	$1/65$	$1/35$	$1/15$	$1/5$
DCDD H^1 error	5.59876	4.07716	2.60652	1.29522
DCDD L^2 error	0.0511548	0.0691801	0.103191	0.166225
MSC H^1 error	0.23692	0.237901	0.240543	0.0953943
MSC L^2 error	0.0264199	0.0362644	0.0566373	0.0940624
SUPG H^1 error	4.8204	3.53174	2.22937	0.880752
SUPG L^2 error	0.049678	0.0659883	0.0980748	0.14672
V-SGS H^1 error	7.16679	5.22466	3.34015	1.79238
V-SGS L^2 error	0.0949698	0.125929	0.178508	0.272425
YZB1 H^1 error	7.17349	5.22276	3.32694	1.74474
YZB1 L^2 error	0.0946836	0.125336	0.175623	0.258413
YZB2 H^1 error	5.15391	3.65945	2.15866	0.756625
YZB2 L^2 error	0.0435881	0.058613	0.0861	0.131719
clean H^1 error	39.3738	20.335	7.3757	1.35411
clean L^2 error	0.174865	0.166407	0.133537	0.0826977

Table D.2: Errors for different mesh size at $t = 0.5$ (with time step $\Delta t = {}^{h}/_{6}$, resulting in a Courant number of $Cr = 0.25$)

D.2 SUPG stabilisation with shock-capturing

h	$1/65$	$1/35$	$1/15$	$1/5$
SUPG+DCDD H^1 error	6.09577	4.343	2.53028	0.835475
SUPG+DCDD L^2 error	0.0623706	0.0814642	0.11162	0.144298
SUPG+MSC H^1 error	4.55374	2.85406	1.33571	0.473282
SUPG+MSC L^2 error	0.0464913	0.0597117	0.0804142	0.120032
SUPG+YZB1 H^1 error	7.11651	5.04977	3.01629	1.17788
SUPG+YZB1 L^2 error	0.0908555	0.111459	0.141854	0.175704
SUPG+YZB2 H^1 error	5.68019	4.0055	2.11493	0.60058
SUPG+YZB2 L^2 error	0.0566006	0.0742637	0.0995047	0.12831
clean H^1 error	13.4685	5.18057	1.32495	0.252284
clean L^2 error	0.0553096	0.0396203	0.0435608	0.0848977

Table D.3: Errors of SUPG stabilized computations for different mesh size at $t = 0.1$ (with time step $\Delta t = {}^{h}/_{6}$, resulting in a Courant number of $Cr = 0.25$)

h	$1/65$	$1/35$	$1/15$	$1/5$
SUPG+DCDD H^1 error	6.17402	4.51821	2.91489	1.5477
SUPG+DCDD L^2 error	0.0650477	0.0870401	0.129239	0.202515
SUPG+MSC H^1 error	4.82042	3.53225	2.25218	0.994375
SUPG+MSC L^2 error	0.0496781	0.0659968	0.0984486	0.154213
SUPG+YZB1 H^1 error	7.36725	5.36495	3.43003	1.84697
SUPG+YZB1 L^2 error	0.105764	0.138929	0.193432	0.292547
SUPG+YZB2 H^1 error	5.76333	4.22021	2.7239	1.3792
SUPG+YZB2 L^2 error	0.0594067	0.0793706	0.117996	0.18538
clean H^1 error	39.3738	20.335	7.3757	1.35411
clean L^2 error	0.174865	0.166407	0.133537	0.0826977

Table D.4: Errors of SUPG stabilized computations for different mesh size at $t = 0.5$ (with time step $\Delta t = h/6$, resulting in a Courant number of $Cr = 0.25$)

D.3 SUPG stabilisation with shock-capturing and shock-detection

h	$1/65$	$1/35$	$1/15$	$1/5$
SUPG+DCDD H^1 error	6.09223	4.33349	2.47476	0.523564
SUPG+DCDD L^2 error	0.0623222	0.08122	0.109911	0.123317
SUPG+MSC H^1 error	0.0644934	0.064629	0.0702626	0.098766
SUPG+MSC L^2 error	0.0263568	0.0360091	0.0551752	0.0956767
SUPG+YZB1 H^1 error	7.11492	5.04631	3.00308	1.11898
SUPG+YZB1 L^2 error	0.0907899	0.111255	0.141023	0.170442
SUPG+YZB2 H^1 error	5.66497	3.90189	1.47056	0.227931
SUPG+YZB2 L^2 error	0.0564107	0.0727967	0.0838846	0.104987
clean H^1 error	13.4685	5.18057	1.32495	0.252284
clean L^2 error	0.0553096	0.0396203	0.0435608	0.0848977

Table D.5: Errors of SUPG stabilized computations with shock detection for different mesh size at $t = 0.1$ (with time step $\Delta t = h/6$, resulting in a Courant number of $Cr = 0.25$)

h	$1/65$	$1/35$	$1/15$	$1/5$
SUPG+DCDD H^1 error	6.17402	4.51815	2.9136	1.52512
SUPG+DCDD L^2 error	0.0650476	0.0870385	0.129167	0.200036
SUPG+MSC H^1 error	0.156868	0.148768	0.151683	0.172457
SUPG+MSC L^2 error	0.0301253	0.0384151	0.0569773	0.10178
SUPG+YZB1 H^1 error	7.36719	5.3647	3.42983	1.8433
SUPG+YZB1 L^2 error	0.105768	0.138902	0.193279	0.291157
SUPG+YZB2 H^1 error	5.76333	4.21999	2.71594	0.706539
SUPG+YZB2 L^2 error	0.0594067	0.0793657	0.117561	0.135812
clean H^1 error	39.3738	20.335	7.3757	1.35411
clean L^2 error	0.174865	0.166407	0.133537	0.0826977

Table D.6: Errors of SUPG stabilized computations with shock detection for different mesh size at $t = 0.5$ (with time step $\Delta t = h/6$, resulting in a Courant number of $Cr = 0.25$)

D.4 V-SGS stabilisation with shock-capturing

h	$1/65$	$1/35$	$1/15$	$1/5$
V-SGS+DCDD H^1 error	7.03307	5.00825	3.03895	1.29942
V-SGS+DCDD L^2 error	0.0873804	0.108893	0.14225	0.185562
V-SGS+MSC H^1 error	6.90373	4.8682	2.83081	1.06852
V-SGS+MSC L^2 error	0.083066	0.102643	0.131312	0.166157
V-SGS+YZB1 H^1 error	7.38072	5.28175	3.25516	1.49582
V-SGS+YZB1 L^2 error	0.106701	0.129543	0.164361	0.211522
V-SGS+YZB2 H^1 error	6.97622	4.94874	2.95819	1.19019
V-SGS+YZB2 L^2 error	0.0854064	0.106084	0.13751	0.176143
clean H^1 error	13.4685	5.18057	1.32495	0.252284
clean L^2 error	0.0553096	0.0396203	0.0435608	0.0848977

Table D.7: Errors of V-SGS stabilized computations for different mesh size at $t = 0.1$ (with time step $\Delta t = h/6$, resulting in a Courant number of $Cr = 0.25$)

h	$1/65$	$1/35$	$1/15$	$1/5$
V-SGS+DCDD H^1 error	7.24453	5.28685	3.39377	1.85088
V-SGS+DCDD L^2 error	0.0988282	0.131218	0.186816	0.289949
V-SGS+MSC H^1 error	7.16681	5.22476	3.34053	1.79426
V-SGS+MSC L^2 error	0.0949711	0.125938	0.17857	0.273016
V-SGS+YZB1 H^1 error	7.60307	5.5397	3.55947	2.00859
V-SGS+YZB1 L^2 error	0.130382	0.168393	0.233351	0.370287
V-SGS+YZB2 H^1 error	7.20915	5.25898	3.37059	1.82762
V-SGS+YZB2 L^2 error	0.0970316	0.128797	0.183148	0.282635
clean H^1 error	39.3738	20.335	7.3757	1.35411
clean L^2 error	0.174865	0.166407	0.133537	0.0826977

Table D.8: Errors of V-SGS stabilized computations for different mesh size at $t = 0.5$ (with time step $\Delta t = h/6$, resulting in a Courant number of $Cr = 0.25$)

D.5 V-SGS stabilisation with shock-capturing and shock-detection

h	$1/65$	$1/35$	$1/15$	$1/5$
V-SGS+DCDD H^1 error	7.02459	4.99032	2.92169	0.448218
V-SGS+DCDD L^2 error	0.0870294	0.107886	0.134867	0.120355
V-SGS+MSC H^1 error	0.0430831	0.0496882	0.0640486	0.0976829
V-SGS+MSC L^2 error	0.0262583	0.0357767	0.0546654	0.0949216
V-SGS+YZB1 H^1 error	7.37786	5.27573	3.2365	1.44518
V-SGS+YZB1 L^2 error	0.106482	0.128969	0.162233	0.202325
V-SGS+YZB2 H^1 error	6.93649	4.76639	0.797822	0.191843
V-SGS+YZB2 L^2 error	0.0839398	0.0982274	0.071502	0.103345
clean H^1 error	13.4685	5.18057	1.32495	0.252284
clean L^2 error	0.0553096	0.0396203	0.0435608	0.0848977

Table D.9: Errors of V-SGS stabilized computations with shock detection for different mesh size at $t = 0.1$ (with time step $\Delta t = h/6$, resulting in a Courant number of $Cr = 0.25$)

h	$1/65$	$1/35$	$1/15$	$1/5$
V-SGS+DCDD H^1 error	7.24432	5.28602	3.3887	1.81013
V-SGS+DCDD L^2 error	0.0988154	0.131132	0.185832	0.274619
V-SGS+MSC H^1 error	0.0793311	0.0827888	0.0955135	0.140592
V-SGS+MSC L^2 error	0.0289861	0.0381649	0.0572524	0.101346
V-SGS+YZB1 H^1 error	7.60285	5.53923	3.55847	2.00008
V-SGS+YZB1 L^2 error	0.130365	0.168317	0.232816	0.36614
V-SGS+YZB2 H^1 error	7.20824	5.25322	3.33629	0.409989
V-SGS+YZB2 L^2 error	0.0969803	0.128238	0.177326	0.126197
clean H^1 error	39.3738	20.335	7.3757	1.35411
clean L^2 error	0.174865	0.166407	0.133537	0.0826977

Table D.10: Errors of V-SGS stabilized computations with shock detection for different mesh size at $t = 0.5$ (with time step $\Delta t = h/6$, resulting in a Courant number of $Cr = 0.25$)

Appendix E

Moving shock error data

E.1 SUPG stabilized results

h	$1/64$	$1/48$	$1/32$
ADMSC+SUPG Nodal Error error	0.0535888	0.0899839	0.0759868
ADMSC+SUPG L^2 error	0.0432265	0.0439535	0.027438
DCDD+SUPG Nodal Error error	0.261581	0.315624	0.267178
DCDD+SUPG L^2 error	0.0402422	0.0421122	0.050953
SUPG Nodal Error error	0.103289	0.31374	0.122254
SUPG L^2 error	0.0369477	0.0356176	0.0317859
YZB1+SUPG Nodal Error error	0.507659	0.513621	0.512617
YZB1+SUPG L^2 error	0.0655426	0.0735526	0.0910829
YZB2+SUPG Nodal Error error	0.22346	0.286907	0.225463
YZB2+SUPG L^2 error	0.0378186	0.0380662	0.0448099

Table E.1: Errors for different mesh size at $t = 6$, all using SUPG stabilization and different shock-capturing methods.

E.2 V-SGS stabilized results

h	$1/64$	$1/48$	$1/32$
ADMSC+V-SGS Nodal Error error	0.149306	0.601561	0.146706
ADMSC+V-SGS L^2 error	0.0475438	0.0553798	0.0363033
DCDD+V-SGS Nodal Error error	0.495959	0.510712	0.496485
DCDD+V-SGS L^2 error	0.0648709	0.0720262	0.0883684
V-SGS Nodal Error error	0.477166	0.493369	0.478345
V-SGS L^2 error	0.0626208	0.069574	0.0852509
YZB1+V-SGS Nodal Error error	0.679572	0.683919	0.743157
YZB1+V-SGS L^2 error	0.0840196	0.101254	0.131382
YZB2+V-SGS Nodal Error error	0.487074	0.502591	0.487788
YZB2+V-SGS L^2 error	0.0638107	0.0708651	0.0868729

Table E.2: Errors for different mesh size at $t = 6$, all using V-SGS stabilization and different shock-capturing methods.